CALORIMETRY IN HIGH-ENERGY PHYSICS

Christian W. Fabjan

CERN

CH-1211 Geneva 23

1. INTRODUCTION

Much of our present knowledge about elementary particles has been established through a continuing refinement of techniques for measuring the trajectories of individual charged particles. Only in recent years has a different class of detectors—calorimeters—been widely employed, but these have already greatly influenced the scope of experiments.

Conceptually, a calorimeter is a block of matter which intercepts the primary particle, and is of sufficient thickness to cause it to interact and deposit all its energy inside the detector volume in the subsequent cascade or 'shower' of increasingly lower-energy particles. Eventually, most of the incident energy is dissipated and appears in the form of heat. Some (usually a very small) fraction of the deposited energy is detectable in the form of a more practical signal (e.g. scintillation light, Cherenkov light, or ionization charge), which is proportional to the initial energy.

The first large-scale detectors of this type were used in cosmic-ray studies [1]. Interest in calorimeters grew during the late 1960's and early 1970's in view of the new accelerators at CERN [the Intersecting Storage Rings (ISR) and the Super Proton Synchrotron (SPS)] and at the Fermi National Accelerator Laboratory (FNAL), with their greatly changed experimental directions and requirements [2]. One consequence of the new fixed-target accelerators was the advent of intense, high-energy neutrino beams with the need for very massive detectors to study their interactions. This detector development was paralleled by the rapid growth of analog signal-processing techniques: during the last decade the typical number of analog signal-channels of nuclear spectroscopy quality has increased from about 10 to 10^4 in high-energy physics experiments.

Calorimeters offer many attractive capabilities, supplementing or replacing information obtained with magnetic spectrometers:

1) They are sensitive to charged and neutral particles.
2) The 'energy degradation' through the development of the particle cascade is a statistical process, and the average number ⟨N⟩ of secondary particles is proportional to the energy of the incident particle. In principle, the uncertainty in the energy measurement is governed by statistical fluctuations of N, and hence the relative energy resolution σ/E improves as $1/\sqrt{\langle N\rangle} \sim E^{-1/2}$.
3) The length of the detector scales logarithmically with particle energy E, whereas for magnetic spectrometers the size scales with momentum p as $p^{1/2}$, for a given relative momentum resolution $\Delta p/p$.
4) With segmented detectors, information on the shower development allows precise measurements of the position and angle of the incident particle.
5) Their different response to electrons, muons, and hadrons can be exploited for particle identification.
6) Their fast time response allows operation at high particle rates, and the pattern of energy deposition can be used for rapid on-line event selection.

In these notes we comment first on the principal features of detectors designed to measure the energy of photons and electrons, the 'electromagnetic shower detectors' (ESD). The underlying physics has been understood for many years, and such detectors were the main components in many experiments—some of which were credited with important discoveries. Recent developments have been emphasizing precision measurements of energy and position in large arrays.

In the subsequent section the physics of 'hadronic calorimeters' is reviewed. Progress during the last decade contributed to an understanding of the physics of this technique and to a steadily growing range of applications.

The final section concentrates on the technical issues of information processing from calorimeters. We can only select representative examples from the numerous and ingenious methods devised to extract the energy information. We end with a discussion on the state-of-the-art Monte Carlo simulation of electromagnetic and hadronic showers.

These notes follow an earlier review [3], emphasize recent developments, update the bibliography, but do not supersede other excellent introductions to this field [4, 5].

2. ELECTROMAGNETIC SHOWER DETECTORS

2.1 Energy Loss Mechanism

The contributions of the various energy loss mechanisms as a function of particle energy are given in Fig. 1 for electrons and positrons and in Fig. 2 for photons [6]. Above approximately 1 GeV, the principal processes—bremsstrahlung for electrons and positrons, pair production for photons—become energy independent. It is through a succession of these energy loss mechanisms that the electromagnetic cascade (EMC) is propagated, until the energy of the charged secondaries has been degraded to the regime dominated by ionization loss. Within this description, the combined energy loss of the cascade particles in the detector equals the energy of the incident electron or photon. The measurable signal—excitation or ionization of the medium—can be considered as the sum of the signals from the track segments of the positrons and electrons. Naively one might therefore expect that this signal should be equivalent to that produced by muons traversing the detector and whose combined track length equals that of the track

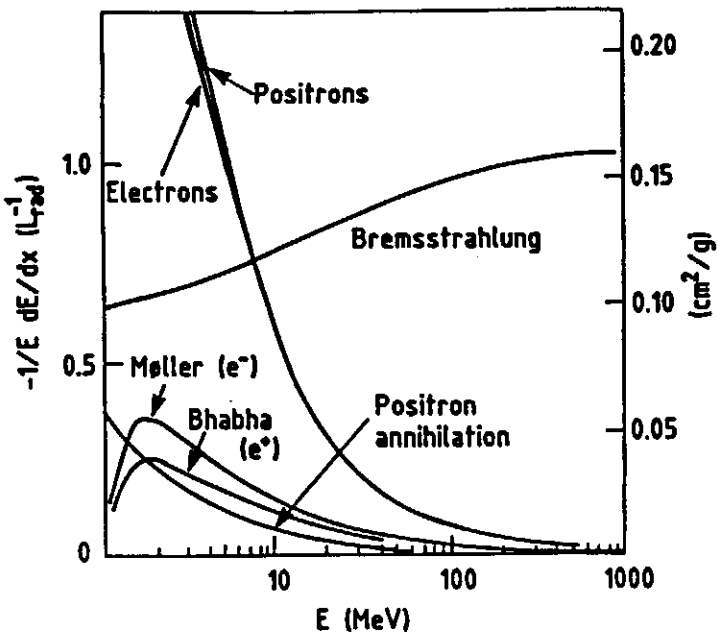

Fig. 1: Fractional energy loss per radiation length (left ordinate) and per g/cm^2 (right ordinate) in lead as a function of electron or positron energy. (Review of Particle Properties, April 1982 edition).

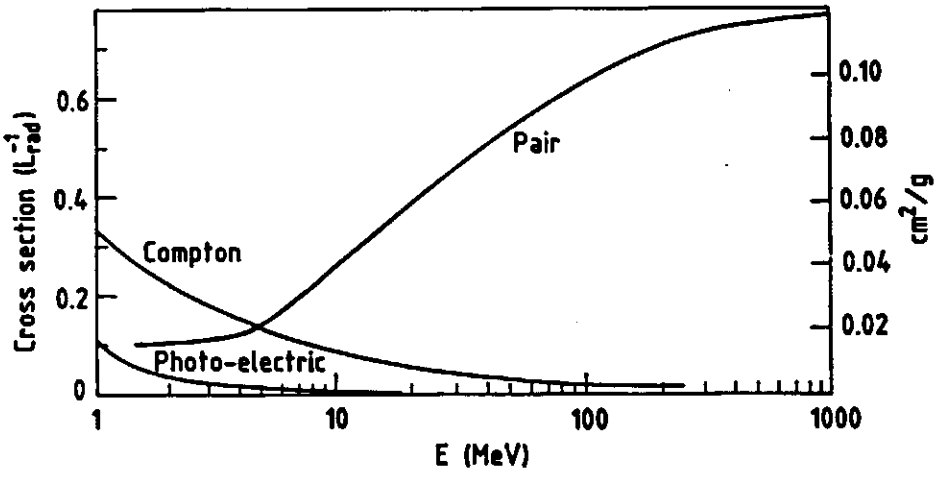

Fig. 2: Photon cross-section σ in lead as a function of photon energy. The intensity of photons can be expressed as $I = I_0 \exp(-\sigma x)$, where x is the path length in radiation lengths. (Review of Particle Properties, April 1980 edition).

segments of the EMC. This picture ignores finer points concerning low-probability photo-nuclear interactions, non-linear response of the ionizing medium as a function of ionization density or the detailed response to the very low energy e^+'s or e^-'s of the last generation of the shower. It emphasizes, however, the concept of 'track length T': a calorimeter is a useful device, because in the process of cascade formation the total track length T required for absorption is broken up into a 'tree' of many individual segments.

The electromagnetic cascading is fully described by quantum electrodynamics (QED) [7], and depends essentially on the density of electrons in the absorber medium. For this reason it is possible to describe the characteristic longitudinal dimensions of the high-energy EMC ($E > 1$ GeV) in a material-independent way, expressed by the 'radiation length, X_0'. It is defined through the equation for the energy loss $\Delta E/\Delta x$ *by radiation*

$$(\Delta E/\Delta x)_{\text{radiation}}\,[X_0^{-1}] = -E$$

and the numerical value is well approximated by the following expression:

$$X_0\,[\text{g/cm}^2] \simeq 180\,A/Z^2 \text{ (to better than 20\% for } \simeq Z > 13).$$

Whilst the high-energy part of the EMC is governed by the value of X_0, the low-energy tail of the shower is characterized by the 'critical energy ϵ' of the medium. It is defined as the energy loss *by collisions* of electrons or positrons of energy ϵ in the medium per unit X_0, i.e.

$$(dE/dx)_{\text{collision}}\,[X_0^{-1}] = -\epsilon, \qquad \text{where } \epsilon\,(\text{MeV}) \simeq 550 \times Z^{-1}$$

(accurate to better than 10% for $Z > 13$). This value of ϵ coincides approximately with that value of the electron energy below which the ionization energy loss starts to dominate the energy loss by bremsstrahlung. The critical energy ϵ is seen to define the dividing line between shower multiplication and the subsequent dissipation of the shower energy through excitation and ionization.

A rigorous, analytical description of the longitudinal shower profile has been given by Rossi [8] based on the following assumptions ('Rossi's approximation B'), and the most useful results are given in Table 1:

i) the cross-section for ionization is energy independent, $dE/dx\,[X_0^{-1}] = -\epsilon$;
ii) multiple scattering is neglected and the EMC is treated one-dimensionally;
iii) Compton scattering is neglected.

Table 1: EMC Quantities Evaluated with Rossi's Approximation B
($y = E/\epsilon$; T measured in units of X_0)

	Incident electron	Incident photons
Peak of shower, t_{max}	$1.0 \times (\ln y - 1)$	$1.0 \times (\ln y - 0.5)$
Centre of gravity, t_{med}	$t_{max} + 1.4$	$t_{max} + 1.7$
Number e^+ and e^- at peak	$0.3\,y \times (\ln y - 0.37)^{-1/2}$	$0.3\,y \times (\ln y - 0.31)^{-1/2}$
Total track length T	y	y

The characteristic longitudinal EMC profile is shown in Fig. 3 for four very different materials and demonstrates the 'longitudinal scaling in radiation length'. A convenient analytical description of the profile has been given in the form [9]

$$dE/dt = E_0\,b^{\alpha+1}/\Gamma(\alpha+1)t^{\alpha}e^{-bt};\ t = x/X_0,\ \alpha = bt_{max}, \text{ and } b \simeq 0.5.$$

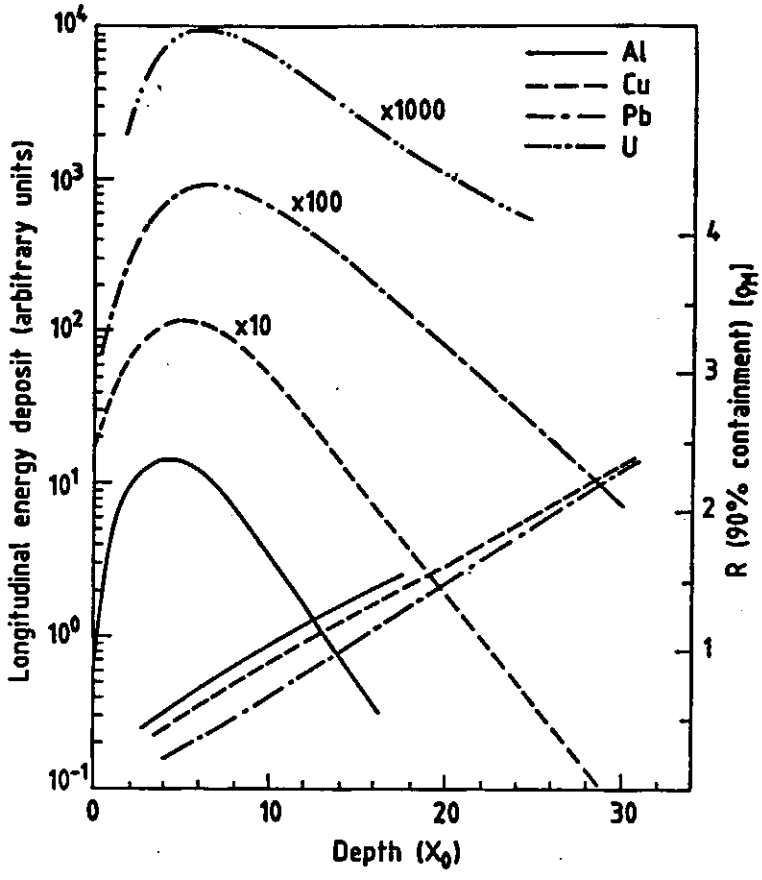

Fig. 3: Longitudinal shower development (left ordinate) of 6 GeV/c electrons in four very different materials, showing the scaling in units of radiation lengths X_0. On the right ordinate the shower radius for 90% containment of the shower is given as a function of the shower depth. In the later development of the cascade, the radial shower dimensions scale with the Molière radius $\varrho_M \sim 7A/Z$. [Al, Cu, and Pb, adapted from G. Bathow et al., Nucl. Phys. B20:592 (1970). Uranium data from G. Barbiellini et al., Ref. [127].

The transverse shower properties, which are not described within the framework of Rossi's 'approximation B' can also be easily understood qualitatively. In the early, most energetic part of the cascade the lateral spread is characterized by both the typical angle for bremsstrahlung emission, $\theta_{brems} \sim p_e/m_e$, and multiple scattering in the absorber. This latter process increasingly influences the lateral spread with decreasing energy of the shower particles and causes a gradual widening of the shower. For the purpose of total energy measurement, the EMC occupies a cylinder of radius R

$$R \approx 2\varrho_M; \quad \varrho_M = 21X_0/\epsilon \simeq 7A/Z\ [g\,cm^{-2}],$$

ϱ_M being the 'Molière Radius', which describes the average lateral deflection of electrons of energy ϵ after traversing one radiation length. In Fig. 4, the transverse shower profile as a function of depth clearly exhibits the rather pronounced central and energetic core surrounded by a low-energy 'halo'.

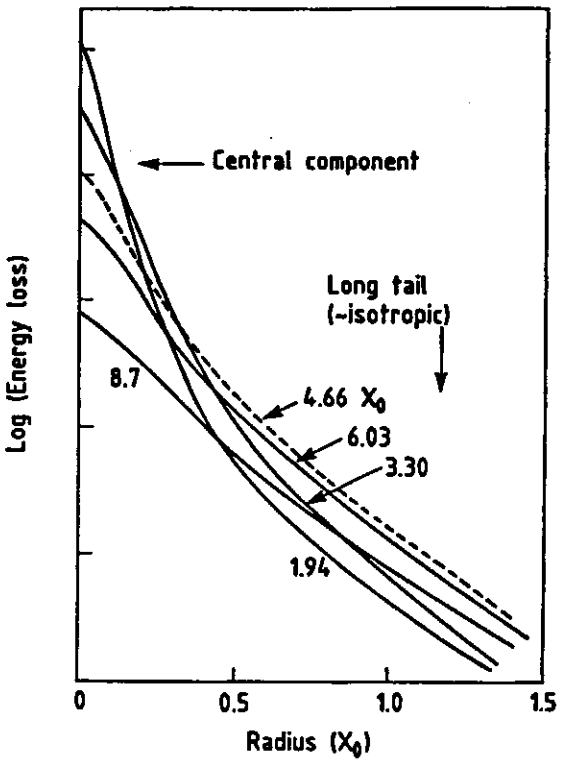

Fig. 4: Radial shower profile of 1 GeV electrons in aluminium; a pronounced central core, surrounded by 'halo', gradually widens with increasing depths of the shower [17].

2.2 Limits on Energy Resolution of EMCs

In the discussion in the previous section we have represented the shower by a total track length T, which could be expressed as $T(X_0) = E_{particle}(MeV)/\epsilon(MeV)$. The 'detectable' track length T_d, i.e. the equivalent track length which corresponds to the measured signal in a particular detector, will in general be shorter, $T_d \leq T$, as practical devices are only sensitive to the cascade particles above a certain threshold energy η. The fractional reduction in visible track length as a function of η/ϵ [4] is indicated in Fig. 5. The dotted lines are the result of an analytic calculation [8] for $E \gg \eta$, and $F(\xi)$ is given by $F(\xi) = [1+\xi \ln (\xi/1.53)] \exp \xi$ ($\xi = 2.29\ \eta/\epsilon$). The points are obtained by Monte Carlo calculations [9–11].

The average detectable track length $\langle T_d \rangle$ is given by $\langle T_d \rangle (X_0) = F(\xi) \cdot E/\epsilon$ and calorimetric energy measurements are possible because $\langle T_d \rangle \propto E$ for any reasonable value of ϵ. The *resolution* of the energy measurement is determined by the *fluctuations* in the shower propagation. The intrinsic component of the resolution is caused by the fluctuations in T_d. This represents the lower bound on the energy resolution and may be qualitatively estimated in the following way: the maximum number of track segments $N_{max} = E/\eta$ hence $\sigma(E)/E \geq \sigma(N_{max})/N_{max}$. In a lead-glass shower counter for which $\eta \sim 0.7$ MeV, one estimates for a 1 GeV shower, $N_{max} = 1000/0.7 = 1.5 \times 10^3$, implying an energy resolution at the level of one to two percent, somewhat higher than the level computed by detailed Monte Carlo calculations [9].

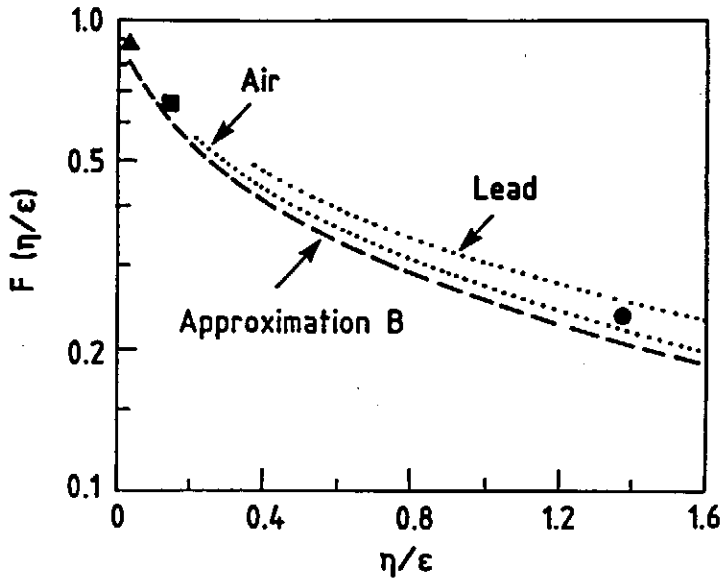

Fig. 5: Fraction F of the total track length which is seen on the average in a fully contained electromagnetic shower. The dotted lines represent analytical calculations and the points represent Monte Carlo results. ▲: lead glass; ■ and ●: lead sampling devices (see Ref. [4]).

In practical detectors, however, usually a number of additional components must be considered, which may conspire to affect the resolution. One important instrumental contribution to the energy resolution comes from incomplete containment of the showers ('energy leakage'), as can be seen from Fig. 6. Available information on average longitudinal containment (both experimental and calculational) may be parametrized as

$$L(98\%)_{av} = t_{max} + 4\lambda_{att},$$

where L(98%) gives the length for 98% longitudinal containment. The quantity λ_{att} characterizes the slow, exponential decay of the shower after the shower maximum (see Fig. 3) expressed as exp $(-t/\lambda_{att})$. The values of λ_{att} are found to be rather energy independent, but material dependent and close in value to the mean free path of photons that have minimum attenuation in a given material. Experimental values cluster around λ_{att} $[X_0] \simeq 3.4 \pm 0.5X_0$. This estimate is in reasonable agreement with other parametrizations [12], e.g. $L(98\%) \simeq 2.5\ t_{max}$ for E in the 10 to 1000 GeV range. The effect of longitudinal leakage on the energy resolution is consistent with the parametrization

$$\sigma(E)/E \simeq [\sigma(E)/E]_{f=0} \times [1 + 2\sqrt{E(GeV)} \times f]$$

for values f of the fractional energy loss through leakage, $f < 0.2$ and $E < 100$ GeV. One notes that longitudinal leakage is more critical than transverse leakage due to the fact that fluctuations about the average longitudinal loss are much larger than for transverse leakage.

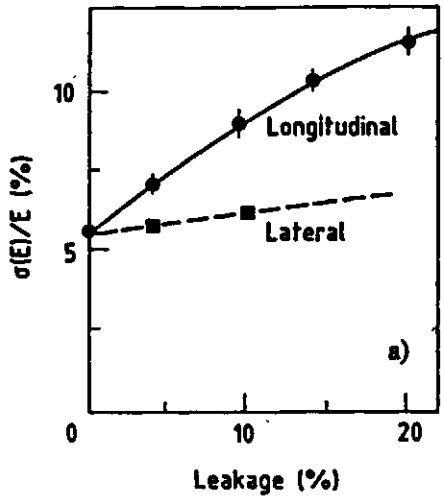

Fig. 6a: Effects of longitudinal and lateral losses on the energy resolution as measured for electrons in the CHARM neutrino calorimeter [23].

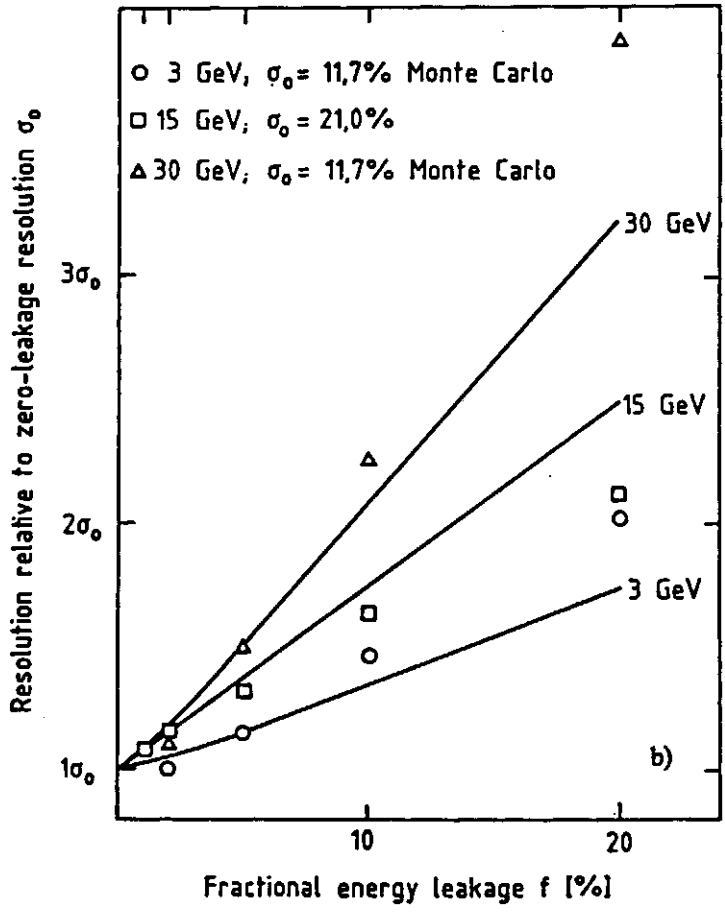

Fig. 6b: Deterioration of the zero-leakage resolution σ_0 as a function of fractional energy leakage f for three different electron energies [21, 23].

Homogeneous detectors have always played a very important role as e.m. calorimeters. Historically, it was NaI that was used as one of the first calorimetric detectors, still unsurpassed in energy resolution. For energies E = 1 GeV, one obtains a value close to the intrinsic limit; at higher energies, the full statistical gain ~ $1/\sqrt{E}$ is not obtained, even for very carefully tuned instruments [13] for which the resolution is quoted as $\sigma(E)/E \simeq 0.009 \times E^{-1/4}$ (GeV). Such a behaviour is characteristic of contributions other than those governed by statistical processes, such as non-uniformity in the signal collection, energy leakage, etc. A second, very frequently used homogeneous detector is lead glass, i.e. glass loaded with 50–60% PbO. The EMC is sampled by the production of Cherenkov light emitted from the relativistic electron-positron pairs. These detectors are therefore characterized by a relatively low light yield—typically 1000 photoelectrons per GeV are measured—and a relatively large cut-off energy η. These two effects combined give a resolution of

$$\sigma_{tot} = (\sigma_\eta^2 + \sigma_{ph}^2)^{1/2} = (0.020^2 + 0.032^2)^{1/2} = 3.8\% \text{ at 1 GeV},$$

in agreement with the best values reported, of $\gtrsim$ 4%. Recent developments of new scintillating crystals have stimulated interest in such homogeneous detectors, which promise exceedingly good performance in the 1 to 100 GeV regime (see the discussion in Section 5).

2.3 Energy Resolution in 'Sampling' Calorimeters

'Sampling' calorimeters are devices in which the functions of energy degradation and energy measurement are separated in alternating layers of different substances. This allows a considerably greater freedom in the optimization of detectors for certain specific applications. The choice of a 'passive' absorber—typically plates made of Fe, Cu, or Pb, each ranging in thickness from a fraction of X_0 to a few X_0—makes it possible to build rather compact devices, and it permits optimization for a specific experimental requirement such as electron/pion discrimination or position measurement. Independently of the choice of the absorber, the readout method may be selected for best uniformity of signal collection, high spatial subdivision, rate capability or other criteria. The disadvantage is that only a fraction of the total energy of the EMC is 'sampled' in the active planes, resulting in additional *'sampling' fluctuations* of the energy determination.

These general comments apply to both electromagnetic and hadron calorimeters. The following discussion of sampling fluctuations is specifically valid for the measurement with e.m. calorimeters, for which sampling fluctuations have been rather carefully studied. Today we know that they depend on the characteristics of both the passive and the active medium (in particular, thickness and density) and that several effects contribute to the 'total' sampling fluctuation.

The *'intrinsic sampling' fluctuations* express the statistical fluctuations in the number of e^+e^- pairs traversing the active signal planes and can be estimated in the spirit of approximation B. The number N_x of crossings is ($\eta = 0$)

$$N_x = T \text{ (total track length)/d (distance between active plates)},$$

where $T = E/\epsilon$ and hence $N_x = E/\epsilon d = E/\Delta E$, ΔE being the energy loss per unit cell.

The contribution to the energy resolution is

$$\sigma(E)/E_{sampling} = \sigma(N_x)/N_x = 1/\sqrt{N_x} = 3.2\% \; [\Delta E\,(MeV)/E\,(GeV)]^{1/2}.$$

This expression has to be regarded as a lower bound on the sampling fluctuations for the following reasons:

- tracks originate from pair-produced particles and therefore the number of independent gap crossings would be only $N_x/2$ for totally correlated production;

- approximation B ignores multiple scattering, which increases the effective distance d to $d = d/\langle\cos\theta\rangle$, where the characteristic multiple scattering angle θ is given by $\langle\cos\theta\rangle \sim \cos(21\,MeV/\epsilon\pi)$ [4];

- for $\eta \neq 0$, $T_d = F(\xi)T$.

Considering these effects, the contribution of sampling fluctuations to the energy resolution is evaluated as

$$[\sigma(E)/E]_{sampling} \gtrsim 3.2\% \; \{\Delta E\,(MeV)/[F(\xi) \times \cos(21/\epsilon\pi)\,E\,(GeV)]\}^{1/2}.$$

This expression does not include possible additional effects due to *'Landau' fluctuations* of the energy deposit in the active signal planes, which can be estimated to contribute

$$[\sigma(E)/E]_{Landau} \simeq 3/[\sqrt{N_x} \times \ln(1.3 \times 10^4\,\delta)],$$

where δ (MeV) gives the energy loss per active detector plane. Such additional fluctuations are small for energy losses δ of a few MeV (e.g. a few millimetres of scintillator), but may become comparable to the 'intrinsic' sampling fluctuations for very thin detectors, e.g. gaseous detectors with δ in the keV range. In addition to these 'Landau' fluctuations there is a further source of errors which also depends on the density of the active medium, *'path-length' fluctuation:* low-energy electrons may be multiply scattered into the plane of the active detector and then travel distances much larger than, for example, the gap thickness in gaseous detector planes, depositing considerably more energy compared to that deposited under perpendicular traversal. This effect is quantitatively less significant in dense active layers, because the range of the low energy electrons is comparable to the thickness of these layers. Moreover, increased multiple scattering in dense detector planes will also tend to reduce this effect relative to light absorbers. From Fig. 7 it can be seen that path-length fluctuations may contribute as much as Landau fluctuations to the resolution [14] in detectors with gaseous readouts.

Concluding this section, we compare in Table 2 the measured performance of some characteristic sampling devices, and compare it with the estimated contributions using the formulae given here. The energy resolution is seen to be rather well described by these estimates, provided that instrumental effects (such as calibration errors, photon statistics, leakage, etc.) do not dominate.

It is interesting to note that the path length and the Landau fluctuations are not negligible even in the case of dense active readout gaps, if these are very thin (e.g. measurements with the W/Si calorimeter).

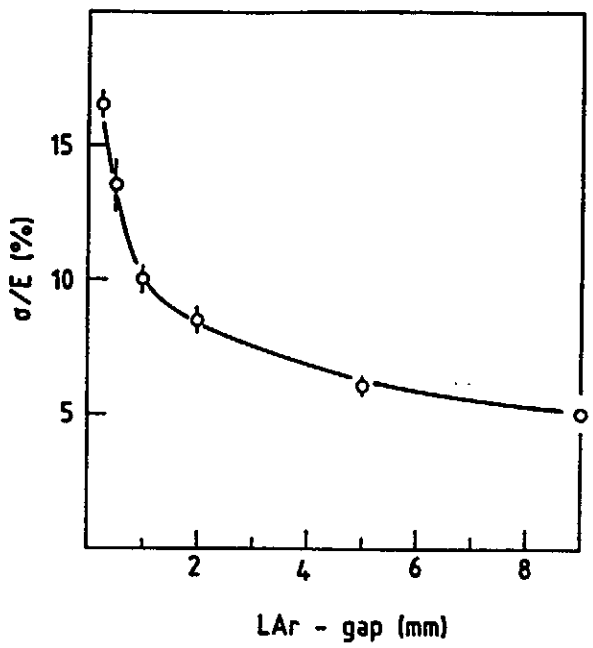

Fig.7a: Energy resolution versus thickness of the active liquid-argon layer for 1 GeV electrons in an iron/argon sampling calorimeter.

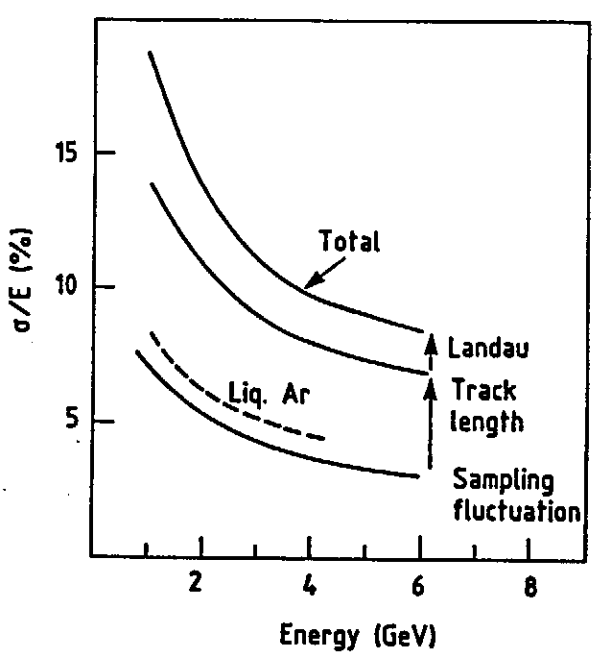

Fig. 7b: Contributions of sampling, path length, and Landau fluctuations to the energy resolution of a lead/MWPC sampling calorimeter. The latter contribute approximately equally (~ 12% at E = 1 GeV), and combined quadratically with the sampling fluctuations (~ 7%) they account for the overall resolution of ~ $18\%/\sqrt{E}$ [14].

Table 2: Measured and Estimated Performance of Electromagnetic Sampling Calorimeters

Device passive/active (mm)	Al/scint. 89/30	Fe/LAr 1.5/2.0	Cu/scint. 5/2.5	W/Si detector 7.0/0.2	Pb/Ar/CO_2 at NTP 2.0/10.0	U/scint. 1.6/2.5
Energy resolution measured at 1 GeV(%)	20	7.5	13.0	25.0	$\leq$ 20.0	11.0
η (MeV)	3.0	0.7 (?)	0.7 (?)	0.7 (?)	$\leq$ 0.6 (?)	0.7 (?)
$F(\xi)^{-1/2}$	1.16	1.10	1.10	1.18	1.18	1.20
$\langle\cos\theta\rangle^{-1/2}$	1.00	1.03	1.03	1.27	1.36	1.51
σ^{sample}	23	4.8	9.2	19.1	8.2	10.6
σ_{Landau}	3.8	1.0	1.0	4.5	8.70	1
$\sigma_{\text{path length}}$		5.7	6	17.5	13.0	6 (?)
$\sigma_{\text{estimated}}$	23	7.5	10.0	25.9	17.7	12.2
Note	a	b, c	c, d, e	c, f	c, g	c, e, h

a) A.N. Diddens et al., Nucl. Instrum. Methods 178:27 (1980).
b) C.W. Fabjan et al., Nucl. Instrum. Methods 141: 61 (1977).
c) Path-length fluctuations estimated from H.G. Fischer, Nucl. Instrum. Methods 156:81 (1978).
d) O. Botner, Phys. Scripta 23:555 (1981).
e) Difference consistent with photon statistics.
f) G. Barbiellini et al., Nucl. Instrum. Methods 235:55 (1983).
g) J.A. Appel, Fermilab FN-380 (1982).
h) R. Carosi et al., Nucl. Instrum. Methods 219:311 (1984).

2.4 'Transition' Effects

The concept of total track length T has been repeatedly used to estimate properties of the EMC. In particular, it suggests equating the measurable signal in a specific calorimeter with the energy deposit of penetrating particles such as muons of equivalent path length, or in terms of the number of equivalent particles n_{ep}. One equivalent particle (1 ep) is defined as the most probable detected energy, $(dE/dx)^{mp}$ of a penetrating muon

$$1\ \text{ep} = (dE/dx)^{mp}_{\text{visible},\,\mu}.$$

The expected number n_{ep} for electrons with kinetic energy E^e_{kin} would be

$$n^{el}_{ep}(\text{expected}) = E^{el}_{kin}/1\ \text{ep}.$$

Experimentally, yet, one always observes:

$$n_{ep}^{el}(\text{visible}) < n_{ep}^{el}(\text{expected}) \quad \text{or} \quad \text{'e}/\mu < 1\text{'}.$$

A summary of some representative measurements is given in Table 3.

The calibration of an EMC with muons is one way of establishing an absolute energy scale. If carried out in a reproducible and consistent way, it would allow us to compare, on an absolute energy scale, the electron response of different calorimeters—a crucial ingredient also in the understanding of hadronic calorimeters (see Section 3). As an example, the energy scale for muons quoted in Table 3 is based on the most probable

Table 3: Average Calorimeter Response for Pions and Muons*)
Relative to Electrons [38]

Type of particle (energy)	Sampling calorimeter structure: scintillator / liquid argon		
	with Fe (Cu)	with Pb	with ^{238}U
Electrons (10 GeV/c)	1	1	1
	1	1	1
Pions (10 GeV/c)	0.63 ± 0.03[a,b]	0.68 ± 0.04[b]	0.93 ± 0.03[b,d]
	0.7[c]	not yet measured	1.0 ± 0.05[c]
Muons (~ 10 GeV/c)	1.15[b]	1.26[b]	1.29[b,d]
	1.1	1.4[e,f]	1.65[g]

*) See text for definition of muon response.
NB: Errors of typically 10% have to be assumed for figures quoted without error.

a) A. Beer et al., Nucl. Instrum. Methods 224:360 (1984).
b) O. Botner, Phys. Scripta 23:555 (1981).
c) C.W. Fabjan et al., Nucl. Instrum. Methods 141:61 (1977).
d) T. Akesson et al., Properties of a fine-sampling uranium-copper scintillator hadron calorimeter, submitted to Nucl. Instrum. Methods (1985).
e) J. Cobb et al., Nucl. Instrum. Methods 158:93 (1979).
A. Lankford, CERN-EP Internal Report 78-3 (1978).
C. Kourkoumelis, CERN Report 77-06 (1977).
f) P. Steffen (NA31 Collaboration, CERN), private communication.
g) C.W. Fabjan and W. Willis, unpublished note on measurements reported in c).

energy loss evaluated for the total thickness of the device, applying the energy loss formula [15] for the appropriate muon momentum, including the non-negligible relativistic rise. The energy loss in the active medium was estimated to follow the ratio of the respective mass of the passive and active materials. Table 3 shows that the discrepancies from the 'naïve' expectations are substantial, with some indication that the response depends on the sampling thickness and the atomic number of the active and passive materials.

These discrepancies have been repeatedly attributed to 'transition effects' at the boundary between the different layers [16–18], often characterized by very different critical energies and hence different collision losses per radiation length. One expects that at a boundary from high Z to low Z (e.g. Fe to scintillator), the increased collision losses in the low-Z substance will reduce the electron flux, in agreement with measurements [17, 18] and some recent Monte Carlo calculations [19]. Apart from local disturbances of the EMC, multiple scattering tends to increase the effective path length in the high-Z absorber relative to the low-Z readout and this mechanism may also suppress the electron response relative to muons, for increasing Z. Furthermore, a considerable fraction of the energy is deposited by the last generation of the cascade, consisting of low-energy particles, and saturation in the response of readout substances (which occur in scintillator or liquid argon) will further suppress the measured response relative to muons.

It may be concluded that for a more refined understanding of sampling detectors it will be important to calibrate carefully the electron response on an absolute energy scale with a reproducible standard, as provided e.g. by muons.

2.5 Spatial Resolution

In subsection 2.1 we described in general the physical processes contributing to the shower propagation and its characteristic dimension. Typical angles for bremsstrahlung emission and multiple scattering depend on the energy of the shower particles and hence alter the transverse shower profile as a function of longitudinal depth inside the shower. Before the shower maximum, typically more than 90% of the energy is contained in a cylinder of radius $r \simeq 0.5X_0$, whereas the radius for 90% containment of the total energy is $r \simeq 2\varrho_M$. For the localization of the impact point of a photon it is therefore advantageous to probe the shower in the early part before the shower maximum. In principle, given sufficiently fine-grained instrumental resolution, the localization σ_x of the centre of gravity of the transverse distribution is determined by signal/noise considerations and, therefore, should improve with increasing particle energy E as $\sigma_x \sim E^{-1/2}$, which is confirmed experimentally [20], reaching sub-millimetre accuracy for 100 GeV showers [21]. If position resolution is the principal criterion, one may achieve very high spatial subdivision using multiwire proportional chamber (MWPC) techniques [22] allowing localization at the millimetre level.

Somewhat different criteria apply if both good position and energy resolution are required, e.g. for the determination of the invariant mass of particles such as π^0's, $J/\psi \to e^+e^-$, etc. In this case the centres of gravity of the complete showers have to be determined—frequently with the constraint of minimizing the sharing of energy between the neighbouring showers—; even then, excellent spatial resolutions of the order of 1 mm have been reported [20], e.g. in an array of lead-glass blocks of 35 × 35 mm cross-section.

Given simultaneous information on the transverse and longitudinal shower development, the *direction* of a shower and hence the angle of incidence of the particle may be reconstructed. As an example, for the CHARM neutrino calorimeter [23] an angular resolution of $\sigma(\theta_e)$ (mrad) = $20/E^{1/2}$ + 560/E (E in GeV) was measured; for a FNAL neutrino calorimeter [24] the following result is quoted:

$$\sigma(\theta_e)\ (\text{mrad}) = 3.5 + 53/E\ (\text{GeV}).$$

3. HADRONIC SHOWER DETECTORS

3.1 General properties

Conceptually, the energy measurement of hadronic showers is analogous to that of EMCs, but the much greater variety and complexity of the hadronic processes propagating the hadronic cascade (HC) complicate the detailed understanding. No simple analytical description of hadronic showers exists, but the elementary processes are well studied.

Typical of hadronic interactions is multiple particle production with transverse momentum $\langle p_T \rangle \simeq 0.35$ GeV/c, for which about half of the available energy is consumed (the inelasticity $K \simeq 0.5$). The remainder of the energy is carried by fast, forward-going (leading) particles. The secondaries are mostly pions and nucleons, and their multiplicity is only weakly energy-dependent. The characteristic stages in the HC development are summarized in Table 4. Two specific features have been identified as the principal physics limitations to the energy resolution of hadronic calorimeters:

i) A considerable part of the secondaries are π^0's, which will propagate electromagnetically without any further nuclear interactions; the average fraction converted into $f_{\pi^0} = 0.1 \ln E$ (GeV), for energies E in the range of a few to several hundred GeV. The size of the π^0 component is largely determined by the production in the first interaction, and event-by-event fluctuations about the average value are, therefore, important.
ii) A sizeable amount of the available energy is converted into excitation or break-up of the nuclei, of which only a fraction will result in detectable ('visible') energy.

The two processes, intimately correlated, may lead, for a given entering hadron, to a very different shower composition, which has a very different detectable response. Together they impose the intrinsic limitation on the performance of hadronic calorimeters.

Table 4 gives some indications of the relative importance of these competing processes. Considerable insight has been gained from very detailed Monte Carlo calculations, which in their most ambitious form aim to simulate the full nuclear and particle physics aspects of the hadronic cascade based on the measured cross-sections of the elementary processes (see also Section 6) [25]. Examples showing the energy dependence of the principal effects are given in Fig. 8. It should be noted that these various processes contribute in varying degrees to the visible energy of the HC, and that a considerable fraction—such as nuclear binding energy, muons, and neutrinos—will be lost in the form of 'invisible' or undetectable energy.

Table 4: Characteristic Properties of the Hadronic Cascade

Reaction	Properties	Influence on energy resolution	Characteristic time (s)	Characteristic length (g/cm^2)
Hadron production	Multiplicity $\simeq A^{0.1} \ln s$ Inelasticity $\simeq 1/2$	π^0/π^+ ratio Binding energy loss.	10^{-22}	Abs. length $\lambda \simeq 35A^{1/3}$
Nuclear de-excitation	Evaporation energy $\simeq 10\%$ Binding energy $\simeq 10\%$ Fast neutrons $\simeq 40\%$ Fast protons $\simeq 40\%$	Binding energy loss. Poor or different response to n, charged particles, and γ's.	10^{-18}–10^{-13}	Fast neutrons $\lambda_n \simeq 100$ Fast protons $\lambda_p \simeq 20$
Pion and muon decays	Fractional energy of μ's and ν's $\simeq 5\%$	Loss of ν's	10^{-8}–10^{-6}	$\gg \lambda$
Decay of c, b particles produced in multi-TeV cascades	Fractional energy of μ's and ν's at percent level	Loss of ν's. Tails in resolution function.	10^{-12}–10^{-10}	$\ll \lambda$

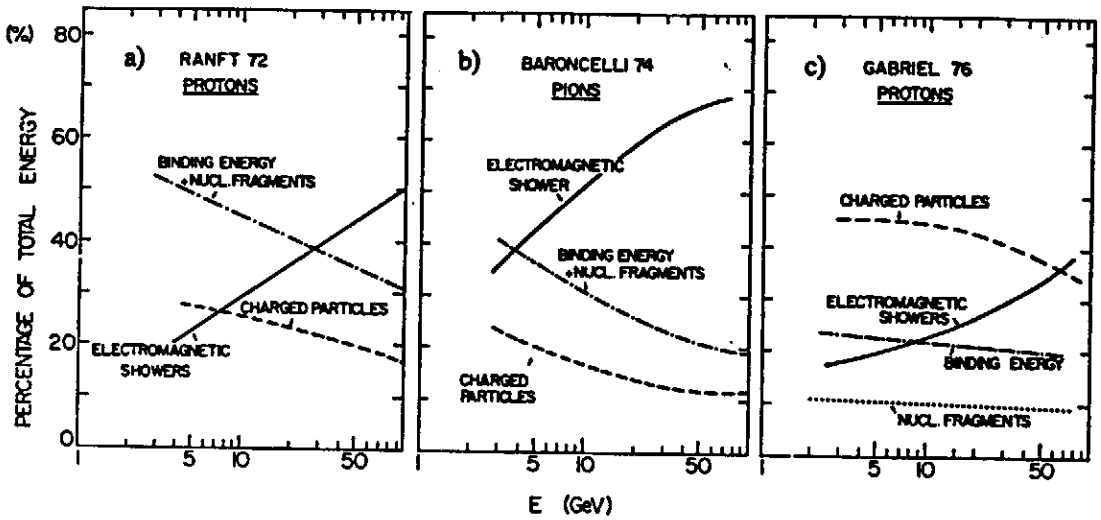

Fig. 8: Relative contributions of the most important processes to the energy dissipated by hadronic showers, as evaluated from three representative Monte Carlo calculations [25].

Average longitudinal and transverse distributions (Fig. 9) are useful estimates of the characteristic dimensions for near-complete shower containment. The average longitudinal distribution exhibits 'scaling in units of absorption length λ'. The transverse distributions depend—as in the case of EMCs—on the longitudinal depth: the core of the shower is rather narrow (FWHM from 0.1 to 0.5λ), increasing with shower depth. The highly energetic, very collimated core is surrounded by lower-energy particles, which extend a considerable distance away from the shower axis, such that for 95% containment a cylinder of radius $R \sim 1\lambda$ is required.

Experimental data are consistent with the following parametrization:

a) the shower maximum, measured from the face of the calorimeter, is given by

$$t_{max}(\lambda) \sim 0.2 \ln E\,(\mathrm{GeV}) + 0.7;$$

it occurs at a smaller depth in high-Z materials due to the smaller ratio of X_0/λ.

b) The longitudinal dimension required for almost full containment is approximated by

$$L_{0.95}(\lambda) \simeq t_{max} + 2.5\,\lambda_{att},$$

again measured from the face of the calorimeter. The quantity λ_{att} describes the exponential decay of the shower beyond t_{max} and increases with energy approximately as $\lambda_{att} \simeq \lambda[E\,(\mathrm{GeV})]^{0.13}$, with an indication of a weaker energy dependence for high-Z absorbers. The expression for $L_{0.95}$ describes available data in the energy range of a few GeV to a few hundred GeV to within 10%.

c) The transverse radius R of the 95%-containment cylinder is very approximately $R_{0.95} \lesssim 1\lambda$; it does not scale with λ and is smaller in high-Z substances.

d) A useful parametrization of the longitudinal shower development is

$$dE/ds = K[wt^a e^{-bt} + (1-w)\,t^c e^{-dt}],$$

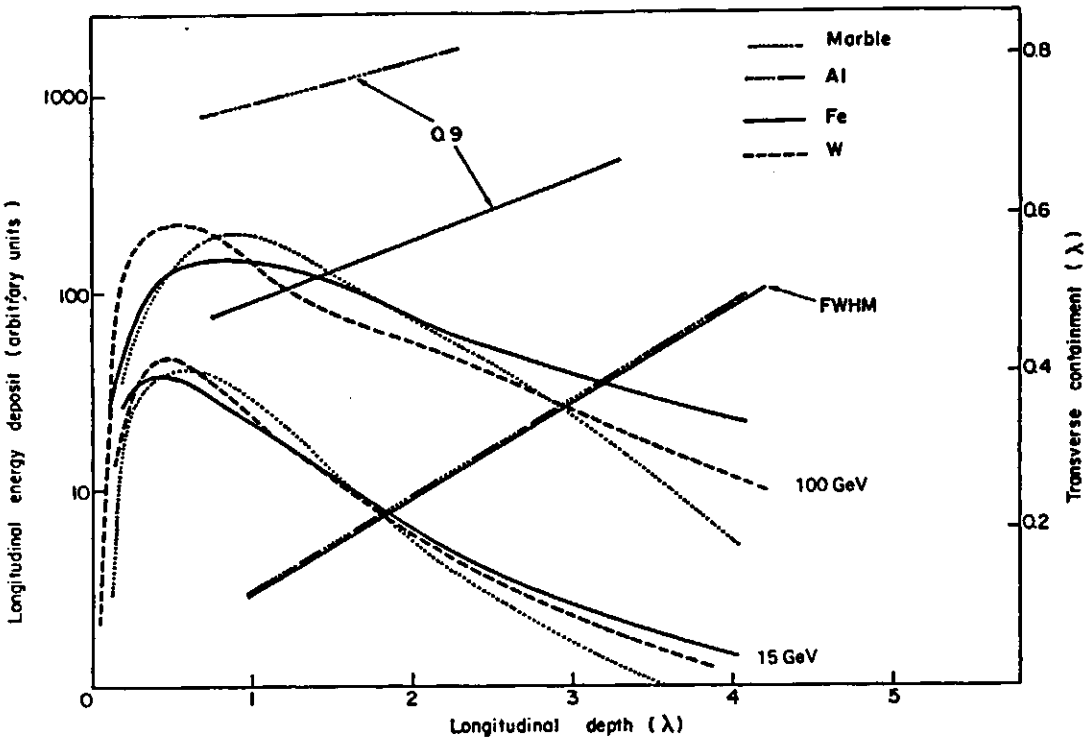

Fig. 9: Longitudinal shower development (left ordinate) induced by hadrons in different materials, showing approximate scaling in absorption length λ. The shower distributions are measured from the vertex of the shower and are therefore more peaked than those measured with respect to the face of the calorimeter. For the transverse distributions as a function of shower depth, scaling in λ is found for the narrow core (FWHM) of the showers. The radius of the cylinder for 90% lateral containment is much larger and does not scale in λ. [10 GeV/c π's: B. Friend et al., Nucl. Instrum. Methods 136:505 (1976)]. Note that marble and aluminium have almost identical absorption and radiation lengths [Marble: M. Jonker et al., Nucl. Instrum. Methods 200:183 (1982); Fe: M. Holder et al., Nucl. Instrum. Methods 151:69 (1978); W: D.L. Cheshire et al., Nucl. Instrum. Methods 141:219 (1977)].

where t is the depth, starting from the shower origin, in radiation lengths, and ℓ is the same depth in units of absorption lengths. The parameters a,b,c,d are fits to the data and are given a logarithmic energy dependence. Crude shower fluctuations may be simulated by i) randomly varying the depth of the shower origin; ii) smearing the incident particle energy to simulate the calorimeter energy resolution; iii) randomly varying the length of the shower by scaling the values of t and l [26].

Although the total depth needed for near-complete absorption increases only logarithmically with energy, it does require, for example, about 8λ to contain, on the average, more than 95% of a 350 GeV pion.

3.2 Intrinsic Energy Resolution

In the previous subsection we indicated that the fluctuations in the HC development, producing a range of different particles—from π^0's to slow neutrons, muons, and

neutrinos—with vastly different detection characteristics, are the principal limitations to the energy resolution. These fluctuations have been found to be large—of the order of 50% at 1 GeV—in strong contrast with the measurement of e.m. calorimeters, where the *intrinsic* fluctuations of the visible track length are less than 1% at 1 GeV. This understanding of hadronic cascades emerged from studies in which the various possible contributions could be individually identified and measured [27]. The dominant influence of the nuclear processes manifests itself also in the shape of the response function (Fig. 10) and is corroborated by detailed Monte Carlo estimates. Available experimental evidence indicates that the intrinsic hadronic energy resolution is

$$\sigma(E)/E|_{\text{intrinsic}} \simeq 0.45/\sqrt{E\,(\text{GeV})}\,.$$

This relation describes devices made from materials covering almost the complete periodic table from aluminium [23] to lead [28]. Only in hydrogen are these nuclear effects absent, but they are already sizeable in hydrogen-rich absorbers (e.g. scintillators): one measurement in an homogeneous liquid-scintillator calorimeter is reported [29] for which the quoted energy resolution is also consistent with the above-quoted value. The sole known exception from this rule is given by uranium-238, for reasons that are explained in the next subsection.

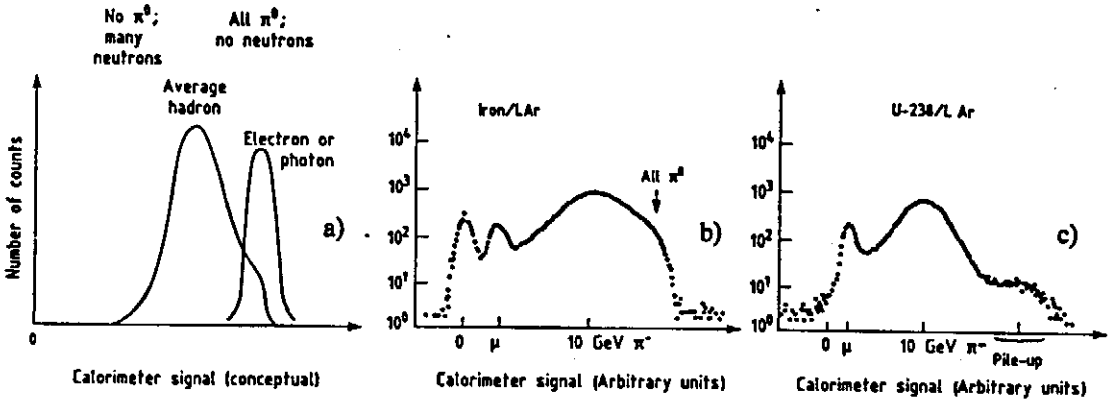

Fig. 10: Calorimeter response for 10 GeV/c pions.
a) Conceptually, the fluctuations are dominated by the nature of the first inelastic interaction. On the average, a certain number of π^0's, charged pions, nuclear fragments, and slow protons and neutrons will be produced. In one extreme case, no π^0's will be produced—only charged pions, neutrons, etc. (low-energy side of response function). At the other extreme the reaction products are mostly π^0's, and the energy deposit will be very similar to that of electrons or photons of equivalent energy.
b) The measured response function is shown for a calorimeter using iron as absorber. The logarithmic ordinate exposes a break in the resolution function corresponding to the case of mostly electromagnetic propagation.
c) The response for a U-238 sampling calorimeter is shown. The nuclear losses are effectively compensated, leading to a response that is nearly equal for charged and neutral pions. The essentially Gaussian response function is also an indication of this uniform response. (The muon peak sets the energy scale corresponding to 'one equivalent particle').

The level of these nuclear effects and, more generally, the level of 'invisible' energy is sensitively measured by comparing the response of a calorimeter for electrons and hadrons at the same 'available' energy, which is the kinetic energy of electrons and nucleons, the total energy for mesons, and the total energy plus the rest mass for antinucleons. A summary of some representative data is shown in Fig. 11. Two features deserve a comment: all calorimeters except those made from uranium show a visible energy of approximately 70% relative to electrons, which slowly increases owing to the rise in the electromagnetic component at higher energies. On the other hand, with energies decreasing below E ~ 1.5 GeV, the nature of the hadronic cascade changes: to a larger measure, the energy is degraded by ionization alone, with the hadron response approaching that of muons and being above that of electrons (see subsection 2.4). In this low-energy limit all calorimeters, including those using uranium as a degrader, are expected to give similar responses. This interpretation is confirmed by the fact that in this low-energy regime the relative resolution improves, $\sigma/E < 0.45/\sqrt{E}$ [30–32], as well as by quantitative Monte Carlo estimates [32].

In summary, the response of hadrons relative to electrons is a sensitive probe of the level of nuclear effects. Typical values are $e/h \simeq 1.4$ for most materials. Strongly correlated with this average suppression are fluctuations in the response; these are due to large fluctuations of the electromagnetic component. The intrinsic resolution of hadron calorimeters is, for these reasons, limited to $\sigma(E)/E_{\text{intrinsic}} \simeq 0.45/\sqrt{E}$ (GeV), unless event-to-event fluctuations in the electromagnetic component of hadron cascades are somehow corrected for. This applies likewise to *homogeneous* and *sampling* devices.

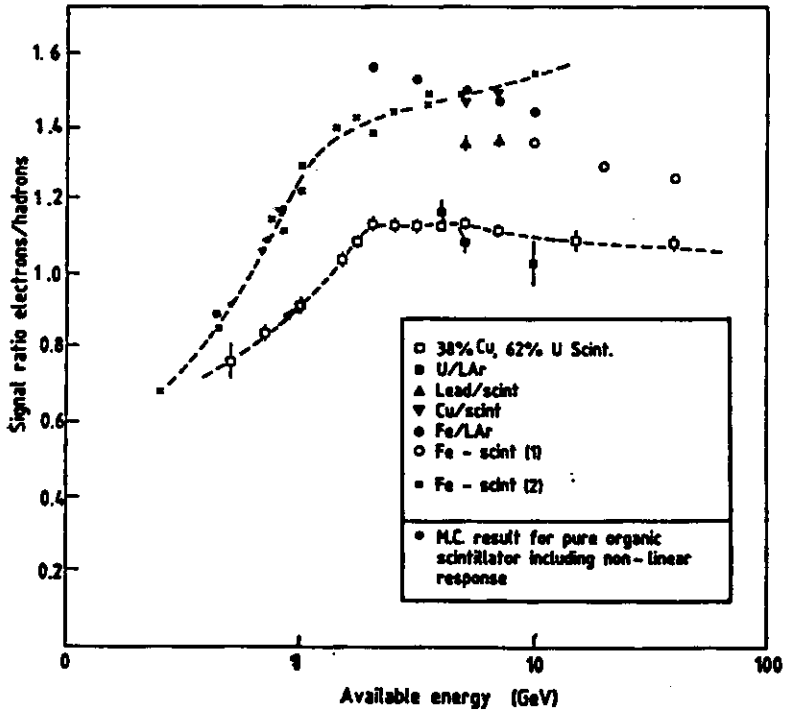

Fig. 11: The ratio of electromagnetic to hadronic energy response as a function of energy for different calorimeter systems: 38% Cu, 62% U/scint. [32]; U/LAr [37]; Cu/scint. [88]; Fe/LAr [37]; Fe/scint. (1) [35]; Fe/scint. (2) [31].

3.3 Compensating Fluctuations

We have emphasized that the relative response between electrons and pions is a sensitive measure of the level of nuclear interactions. An improvement in the energy resolution would be expected if the response of the electromagnetic cascade were identical compared with the purely hadronic one, i.e. if devices with an e/h ratio equal to one were available. Alternatively, given sufficiently detailed information on the individual hadronically induced shower, one would be able to assess the relative components and apply suitable corrections to improve the energy resolution. Both approaches have been explored and are described here.

Several suggestions have been made for monitoring the level of the electromagnetic component event-by-event. One suggestion was to use, as an indicator, the Cherenkov light from relativistic particles dominantly produced by e^+e^- pairs [33], but Monte Carlo estimates [33] for practical devices suggest that it is difficult to obtain a very useful correlation and to improve the resolution significantly. Another suggestion was to monitor the level of the nuclear component by associating heavily ionizing particles with the 'late' component of the hadronic shower [34]. If a calorimeter is instrumented so as to provide detailed longitudinal information, then some useful compensation on a shower-by-shower basis is possible for the electromagnetic/hadronic fluctuations. The most successful attempt was made by the CERN–Dortmund–Heidelberg–Saclay (CDHS) collaboration using the longitudinal information from their relatively fine-grained neutrino calorimeter [35, 36]. This was done by a weighting algorithm applied to the individual longitudinal measurements relative to the total energy measured. In Fig. 12 the unweighted and weighted results for the energy resolution are presented. Firstly, it can be seen that the raw results show a marked deviation from the expected $E^{-1/2}$ dependence.

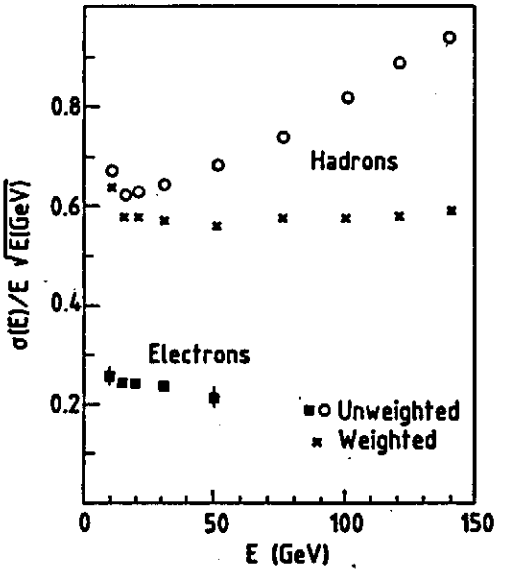

Fig. 12: Energy resolution measured in the CDHS neutrino calorimeter (2.5 cm Fe/scint.) versus the energy of the incident particle. Note that the uncorrected energy resolution for hadrons does not improve as $1/\sqrt{E}$. With a weighting procedure to reduce the large fluctuation due to the e.m. component the resolution is improved, and is consistent with the $1/\sqrt{E}$ scaling up to the highest energies measured [35].

This cannot be ascribed to instrumental effects given the reported result for the electron resolution, which is well described by an $E^{-1/2}$ law. Secondly, the weighting algorithm improves the resolution, particularly at the highest energies, to a level that would be expected from extrapolating the low-energy resolution according to an $E^{-1/2}$ law. In subsection 3.5 we comment further about this deviation from the naïve $1/\sqrt{E}$ behaviour of hadronic calorimeters at high energies.

The more direct cure for these fluctuations would be to equalize the response for electrons and hadrons. In principle, equalizations of these differences, which are at the 30% to 40% level, may be accomplished in two ways: either by decreasing the electron response—typically 20% to 40% lower relative to a minimum-ionizing particle calibration (subsection 2.2); or by boosting the hadronic signal. This latter aspect is being exploited by using uranium-238 as the energy degrader [37]. In that material (and probably also to a lesser extent in thorium) some of the normally invisible energy expended in the nuclear break-up leads to neutron-induced fission, which in turn produces detectable energy in the calorimeter. It can be estimated that on the average 40 fissions are induced per GeV of energy deposited, which altogether liberate about 10 GeV of fission energy. Only a very small fraction (300 to 400 MeV) needs to be detected in order to compensate the nuclear deficit; this could be done either by the few-MeV γ-component or through the fission neutrons liberated in the fission process. Which component and what fraction of the fission contributions are measured depends on the nature of the active sampler. One may achieve essentially complete compensation not only on average but also event-by-event, because the intrinsic resolution is measured to be [32, 37]

$$\sigma(E)^{\text{uranium}}_{\text{intrinsic}} \simeq 0.22/\sqrt{E}\,(\text{GeV}).$$

The fundamental importance of equalizing the hadronic and electromagnetic response should again be emphasized. The latter sensitively depends on the details of the low-energy part of the EMC and hence critically on the material and the sampling frequency. It would appear that this is one further contribution to the tuning of the e/h ratio. Hence for hadron showers, the level of visible compensation is expected to be affected not only by the choice of the passive absorber but also by the response of the active readout to densely ionizing particles (from the HC) and to the electromagnetic component. We do not yet have a complete set of measurements, but Table 3 attempts to organize the available information [38].

3.4 Instrumental Effects to the Energy Resolution

Most hadronic calorimeters are 'sampling' detectors, using preferentially rather dense passive absorbers to reduce the linear dimensions of the instrument. As a consequence, sampling fluctuations of statistical origin analogous to the case of electromagnetic sampling fluctuations (section 2.3) may contribute to the energy resolution, although, for the sampling of the HC we do not have a similar detailed description. Available measurements (see Fig. 13 with the quoted references) are consistent with a parametrization of the form

$$\sigma(E)/E/\text{hadron-sampling} \simeq 0.09\,[\Delta E\,(\text{MeV})/E\,(\text{GeV})]^{1/2}.$$

The quantity ΔE expresses the energy loss per unit sampling cell for minimum ionizing particles. Hadronic sampling fluctuations are approximately twice as large as the

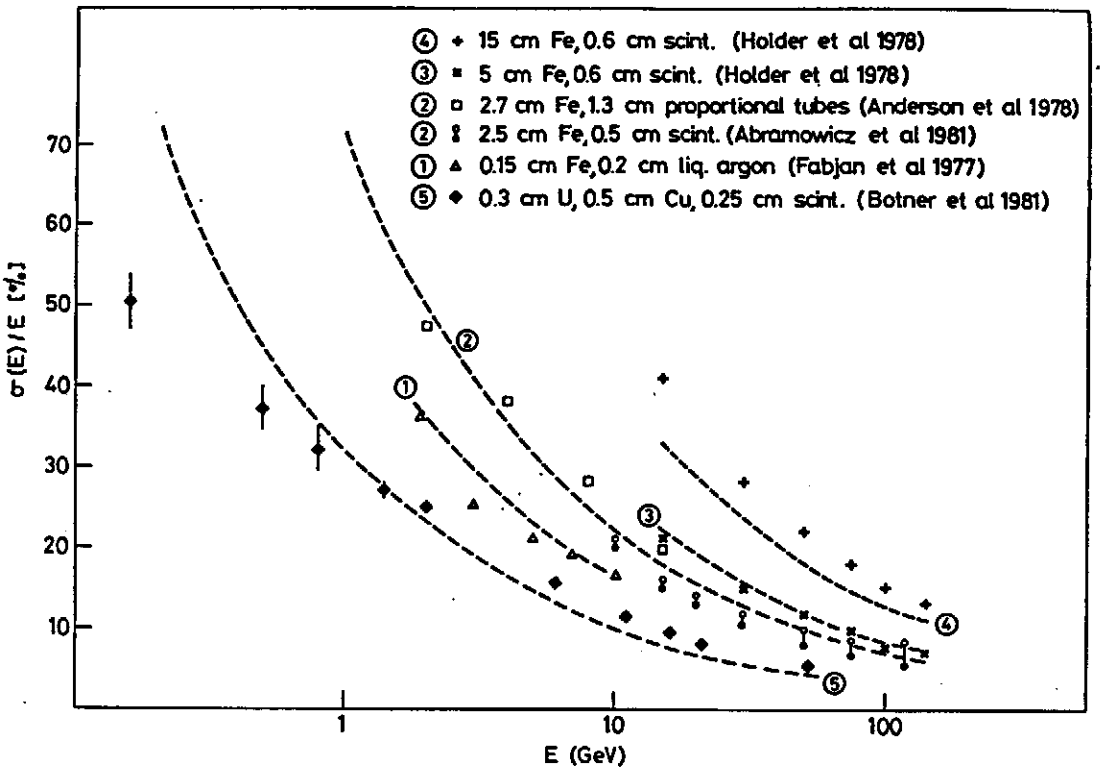

Fig. 13: Energy resolution for hadrons measured with iron and uranium sampling calorimeters. Curves 1–4 are calculated with the values for intrinsic and sampling fluctuations as given in Table 5. For the data on curve 2 [35], the open circles are the raw data; the solid circles are the results of the off-line analysis, using the longitudinal shower information to correct for fluctuations in the electromagnetic/hadronic energy ratio. For curve 5 the intrinsic fluctuation is assumed to be $0.2/\sqrt{E}$, and does not take account of the 35% (in units of λ) admixture of Cu. Below 1 GeV the resolution improves over the expected value and indicates the influence of mechanisms such as ranging and reduced nuclear effects [32, 88]. The data labelled 3 and 4 are by M. Holder et al., Nucl. Instrum. Methods 151:69 (1978), the open squares refer to R.L. Anderson et al., IEEE Trans. Nucl. Sci. NS-25:1-340 (1978).

electromagnetic sampling fluctuations for the same detector; unlike the e.m. case however, where sampling is the predominant contribution to the resolution, sampling in hadronic detectors can be made small relative to the large intrinsic component, and energy resolution need not be sacrificed in hadronic sampling calorimeters.

Energy leakage due to partial shower containment will not only degrade the energy resolution, but will also give rise to very asymmetric resolution functions with low-energy tails. Calorimetric experiments, which emphasize measurements such as neutrino detection based on missing energy or hadronic high-p_T jet production have therefore particularly stringent requirements to achieve very close to 100% containment. Again, as already noted for the measurement of e.m. calorimeters, longitudinal fluctuations are larger than transverse fluctuations and hence longitudinal leakage is more critical to the

performance. For values of fractional leakage $f \leq 0.3$ the degradation of the energy resolution follows approximately the expression

$$\sigma(E)/E \simeq [\sigma(E)/E]_{f=0} \times (1+4f),$$

with the effect being somewhat more pronounced at higher energies for a given fractional energy leakage.

3.5 Calorimetric Energy Resolution of Jets

Increasingly, the physics emphasis is shifting from the measurement of single particles to the analysis of jets of hadrons considered as the principal manifestation of quarks and gluons. This trend is expected to be pursued at the future multi-TeV hadron colliders, where the spectroscopy of particles in the 100 to 1000 GeV range will largely be done through the invariant mass determination of multijet systems [39]. There are two distinct contributions to the resolution of this invariant mass determination. The first effect is associated with the physics of jet production. Jets, unlike single particles, are not unambiguously defined objects, but have to be defined operationally by a 'jet algorithm' (Fig. 14). For example, hadron-initiated jets are produced together with particles originating from peripheral interactions; multijets may partially coalesce. The second contribution to the mass resolution depends on the calorimeter performance itself, and in particular on the momentum response to different particles (Fig. 11). This is seen conceptually in Fig. 15 for two different calorimeters, which have rather comparable nominal resolutions but a very different response to electrons and pions. For very low

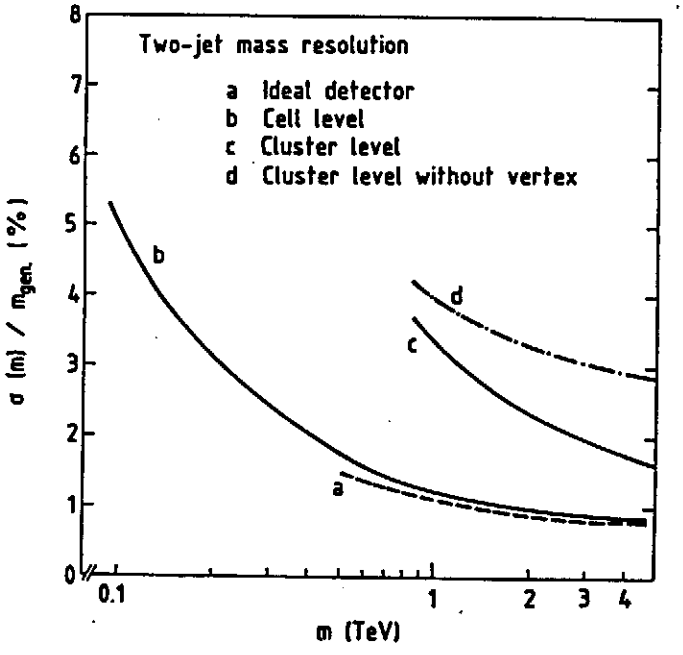

Fig. 14: Two-jet mass resolution as a function of the two-jet mass and for various assumptions on the detector performance. The ideal detector measures the jet mass at the individual particle level; at the cell level the energy information from each cell ($\Delta\phi \times \Delta\eta = 5^\circ \times 0.05$) is considered. At the 'cluster level' certain pattern recognition criteria are introduced. Precise knowledge of the event vertex is important [39].

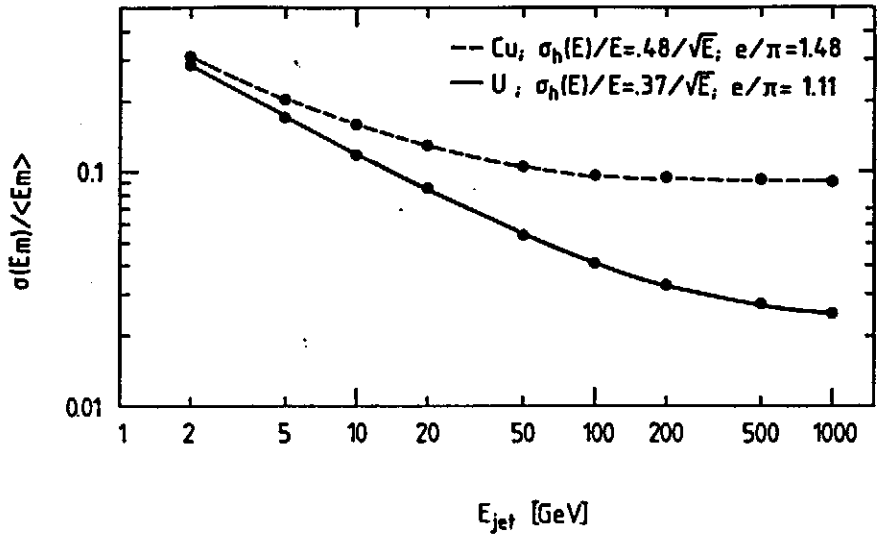

Fig. 15: Jet resolution for an 'infinitely' thick, 4π calorimeter, assuming a Feyman-Field-like fragmentation function. The advantage of a (nearly) compensated calorimeter is particularly evident at very large jet energies. For calorimeters with e/h very different from one, the resolution ceases to improve as $E^{-1/2}$ in the high-energy limit [39].

energies of the jets ($E_{jet} \leq 5$ GeV), the jet resolution is dominated by the very non-linear response to low-momentum particles, and is similar for both calorimeters. At very high energies, the performance is dominated by the relative electron/hadron response. In particular, for the e/h = 1.48 calorimeter it is estimated that the energy resolution levels at approximately 10%. Qualitatively, such a strong influence is expected, because a large fraction of the jet energy is carried by only a few high-momentum particles; fluctuations in the charged hadron/π^0 ratio of these leading particles at sufficiently high energies will dominate over the simple statistical $E^{-1/2}$ improvement.

A similar argument should also be valid for single, very energetic hadrons, which after the first inelastic interaction in a calorimeter will be similar to a jet of particles of comparable energy. Therefore, hadron calorimeters with e/h $\neq$ 1 are expected to show an intrinsic energy resolution $\sigma(E)/E \sim c \times E^{-\alpha}$, with $\alpha < 1/2$ for large energies ($E > 50$ GeV). This behaviour is consistent with the careful analysis (Refs. [35, 36], and Fig. 12) discussed in the previous subsection. Table 5 summarizes the contributions to the energy resolution for both electromagnetic and hadronic calorimeters.

3.6 Spatial Resolution for Hadronic Showers

This discussion follows closely the related comments on e.m. calorimeters (subsection 2.5). Hadron showers are found to consist of a narrow core surrounded by a 'halo' of particles extending to several times the dimensions of the core. Consequently, somewhat different criteria apply to the measurement of the position and to considerations of shower separation. Measurements on the spatial resolution of the impact point [23, 32] may be parametrized approximately in the form

$$\sigma(\text{vertex})\,(\text{cm}) \simeq (\lambda)/[4\sqrt{E\,(\text{GeV})}]\,.$$

Table 5: Principal Contributions to Energy Resolution in Electromagnetic and Hadronic Calorimeters

Mechanisms (add in quadrature)	Electromagnetic showers	Hadronic showers
Intrinsic shower fluctuations	Track-length fluctuations: $\sigma/E \gtrsim 0.005/\sqrt{E}$ (GeV).	Fluctuations in the energy loss: $\sigma/E = 0.45/\sqrt{E}$ (GeV). Scaling weaker than $1/\sqrt{E}$ for high energies. With compensation for nuclear effects: $\sigma/E \simeq 0.22/\sqrt{E}$ (GeV).
Sampling fluctuations	$\sigma/E = 0.04\sqrt{\Delta E/E}$. Nature of readout may augment sampling fluctuations.	$\sigma/E \simeq 0.09\sqrt{\Delta E/E}$
Instrumental effects	Noise and pedestal width: $\sigma/E \sim 1/E$ – determine minimum detectable signal; – limit low-energy performance.	
	Calibration errors and non-uniformities: $\sigma/E \sim$ constant and therefore limits high-energy performance.	
Incomplete containment of shower	$\sigma/E \sim E^{-\alpha}$, $\alpha < 1/2$ (see subsec. 2.2, resp. 3.4). For leakage fraction $\gtrsim$ few %: non-linear response and non-Gaussian 'tail'.	

a) $\Delta E \simeq$ energy loss of a minimum ionizing particle in one sampling layer, measured in MeV; E = total energy, measured in GeV.

In compact calorimeters, where the average interaction length may be as low as $\langle\lambda\rangle \leq 20$ cm, spatial resolutions in the range of a few centimetres at 1 GeV are achievable. The influence of the transverse segmentation has also been studied [40] and the following dependence can be derived:

$$\sigma(\text{vertex}) \simeq \sigma_0\,(\text{vertex})\exp(2d),$$

where the segmentation d is expressed in units of absorption length and σ_0 refers to the intrinsic vertex resolution in the absence of instrumental effects due to finite segmentation. This expression suggests that the improvement becomes rather modest if the lateral segmentation is increased beyond $d\langle\lambda\rangle \leq 0{:}1$, even disregarding other aspects such as photon statistics or noise.

Finally, the angular resolution of hadron showers has been carefully studied for several calorimeters used to investigate neutrino scattering. The limitations again stem from fluctuations in the $\pi^{\pm}/\pi^0$ composition of the HC, because of their (usually) very different spatial shower developments. These effects were purposely minimized in the

case of the CERN-Hamburg-Amsterdam-Rome-Moscow (CHARM) neutrino calorimeter with the choice of marble as the passive absorber material in which EMCs and HCs have approximately the same dimensions [$3X_0$ (cm) ~ λ (cm)]. An angular resolution of

$$\sigma(\theta)_{\text{hadron}}\,(\text{mrad}) \simeq 160/\sqrt{E\,(\text{GeV})} + 560/E\,(\text{GeV})$$

is reported [23], and a similar result was obtained with a detector constructed for the same purpose at FNAL [24].

4. PARTICLE IDENTIFICATION

With hadronic calorimeters it is possible to identify a class of particles which are not always easily identified by other methods, and which may be particularly interesting for very topical physics studies, as summarized in Table 6.

In the following, we discuss in some detail the identification of electrons, muons, and neutrinos.

Table 6: Particle Identification with Calorimeters

Particle produced	Calorimeter technique	Comment
Electron, e	Charged particle initiating the electromagnetic shower	Background from charge exchange $\pi^* N \to \pi^0 + X$ in calorimeter; π discrimination of ~ 10–1000 possible
Photon, γ	Neutral particle initiating the electromagnetic shower	Background from photons from meson decays
$\pi^0, \eta, \ldots \to \gamma\gamma$ $\varrho, \phi, J/\psi, T, \ldots \to e^+e^-$	Invariant mass obtained from measurement of energy and angle	Classical application for electromagnetic calorimeters;
Protons, deuterons, tritons, ... and their antiparticles	Comparison of visible energy E_{vis} in calorimeter with momentum of particle	$E_{vis}^{b(\bar{b})} = (\vec{p}_b^{\,2} + m_b^2)^{1/2} - (+)\,m_b$ Protons (antiprotons) identified up to 4 (5) GeV/c; deuterons (antideuterons) correspondingly higher
(Anti)neutrino	Visible energy E_{vis} in calorimeter compared with missing momentum	Important tool for $e^+e^- \to \nu(\bar{\nu}) + X$ and at CERN Collider (FNAL $p\bar{p}$ collider, $pp(p\bar{p}) \to \nu(\bar{\nu}) + X$
Muon	Particle interacting only electromagnetically (range). E_{vis} compared to $\vec{p}$.	Background from non-interacting pions
Neutron or $K_L^0(n,\bar{K}_L^0)$	Neutral particle initiating hadronic shower	Some discrimination perhaps possible based on detailed (longitudinal) shower information

4.1 Discrimination between Electrons (Photons) and Hadrons

The discrimination is based on the difference in the shower profiles, accentuated in materials with very different radiation and absorption lengths. One finds approximately

$$\lambda\,(\text{g/cm}^2)/X_0\,(\text{g/cm}^2) \sim 35A^{1/3}\,Z^2/180A \sim 0.12Z^{4/3},$$

which explains that heavy materials (lead, tungsten, or uranium) are best suited for electron-hadron discrimination.

The principal physics limitation is imposed by the charge exchange reaction $\pi^- p \rightarrow \pi^0 n$ (or $\pi^+ n \rightarrow \pi^0 p$), which may, under unfavourable circumstances, simulate an electromagnetic shower, closely matching the energy of the incident pion. For pion energies in the few-GeV range, the cross-section for this process is at the one percent level of the total inelastic cross-section, and decreases logarithmically with energy [41]. Typical values for pion discrimination are of the order of 1 in 10^2 in the 1 to 10 GeV region and of 1 in 10^3 or more for particles energies beyond 100 GeV [42]. Considerably better performance (close to 10^3 pion rejection for few-GeV particles) is reported for instruments with very fine longitudinal subdivision [43], which helps to recognize the hadronic origin of a charge-exchange-dominated cascade. Only relatively small further improvements (a factor of 3 to 5) are obtained if transverse shower profile information is available; this is because of the very high degree of correlation between transverse and longitudinal profile [44, 45]. The quoted values apply to electron-hadron discrimination based on shower shape analysis only. If, in addition, energy information can be used, for example knowledge of the electron and pion momenta from magnetic spectroscopy, a further improvement in the rejection of typically one order of magnitude is obtained.

4.2 Muon Identification

Several calorimetric methods exist for discriminating between muons and hadrons or electrons, all based on the very large differences of energy deposit.

i) Calorimeters with fine longitudinal subdivision: such calorimeters, typically many tens of absorption lengths long, have been used predominantly in experiments on incident neutrinos. Energetic muons are very clearly recognized as isolated, minimum-ionizing tracks, frequently ranging far beyond the tracks from hadronic showers.
ii) Muon penetration through active or passive absorbers: the absorbers or calorimeters are deep enough to contain the hadrons adequately and to reduce the 'punch through' probability P of pions ($P \sim e^{-d/\langle\lambda\rangle}$). The observed path length d is measured in units of 'detectable' absorption lengths $\langle\lambda\rangle$, which is found to agree closely with tabulated values [46]. The detailed rejection power against hadrons depends critically on the experimental precautions taken and may be improved by

a) reducing the background from pion and K decay before the calorimeter; the active 'beam dump' experiments have refined this method [47];
b) measuring the muon momentum after the calorimeter in, for example, magnetized iron [48] or a precision magnetic spectrometer [49]; momentum matching of muon candidates before and after the absorber may further improve the rejection [50];
c) correlating the direction of the particle before and behind the absorber. The applicability of the method is limited by multiple scattering of the muons in the absorber (Fig. 16), and accidental overlap with nearby tracks before the absorber.

Very good muon identification will be of increasing importance for experimentation at the storage rings under construction [the FNAL 2 TeV $p\bar{p}$ collider, the CERN Large Electron-Positron Storage Ring (LEP)], or *a fortiori* at those being discussed [the Superconducting Super Collider (SSC) in the USA, the Large Hadron Collider (LHC) in the LEP tunnel]. The very high particle density will make the identification of electrons inside jets extremely difficult, leaving possibly only the muon as a charged lepton signature. In addition, accurate momentum measurement of the muon will be inevitable

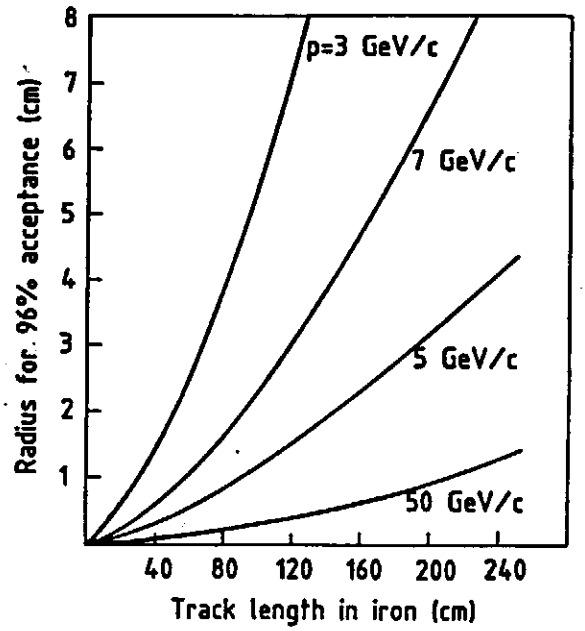

Fig. 16: Radius of 96% acceptance circle for multiply scattered muons as a function of muon track length in iron and of muon momentum. [H. Burmeister et al., CERN/TCL/Int. 74-7 (1974)].

for those experiments which will increasingly exploit very good total energy measurement, for which, of course, the muon momentum has to be included [50, 51].

4.3 Neutrino Identification

The recent discovery of W production based on 'missing momentum' analysis [52] has reminded us of the power of such information. Two related methods can be used:

i) total energy measurement can be accomplished provided 4π calorimetric coverage in the c.m. system is available for all particles (charged, neutrals, muons). This can be practically achieved at e^+e^- storage rings (although 4π hadron calorimetry is not the forte of the forthcoming LEP experiments) or in a fixed-target environment [50]. Neutrino production is implied whenever the measured energy is lower than the total available energy and incompatible with the resolution function of the detector. Total energy measurement does not work well at a hadron collider, such as the CERN $p\bar{p}$ Collider, because a significant fraction of the total energy is always produced at very small angles relative to the incident beams, making a calorimetric measurement impractical. Fortunately, help is provided by

ii) a missing transverse momentum measurement. In this method, clearly related to method (i), the production of a neutrino is signalled by $\Sigma p_{T,i} \neq 0$ to a degree which is incompatible with the detector resolution. Very good missing-momentum resolution at the level of $\sigma(p_{T,miss})/p_{total} \gtrsim 0.3/\sqrt{E}$ has been estimated [53]. This is to be contrasted with the actual performance of a much cruder device for which a $\sigma(p_{T,miss}) \sim 0.7\sqrt{p_T}$ (GeV) is quoted, which is still adequate for a range of striking experimental results [52].

5. SIGNAL READOUT TECHNIQUES FOR CALORIMETERS

During the last 10 years, considerable effort has been devoted to calorimeter instrumentation with a view to developing readout techniques which optimally match an experimental application. The principal goal is to develop methods which will minimize the instrumental effects, relative to the intrinsic performance, caused by the physics of the detectors. Modern beam facilities with their steadily increasing particle energies impose ever more taxing criteria:

- the response must be linear as a function of the particle energy, frequently over a very large dynamic range; only for the exceptional case of energy measurement on isolated particles is a non-linear response acceptable, because it could be remedied (in principle) by calibration;
- the 'noise' or the non-uniformity of the readout system (photoelectron statistics, equivalent noise charge of preamplifiers) must not dominate the energy resolution;
- the readout system must have a rate capability adapted to the observed interaction rate;
- provision must be made for adequate longitudinal and transverse segmentation;
- the absolute and relative energy response must be monitored and maintained with sufficient accuracy;
- other operational characteristics, such as sensitivity to magnetic fields, radiation and temperature, have to be considered.

We have already emphasized the fundamental distinction between homogeneously active or sampling devices. The former have been used in many practical applications for the measurement of electromagnetic showers, whilst the latter represent the only really practical form of hadronic calorimeters. The instrumentation used can be categorized as 'light-collecting' devices measuring scintillator or Cherenkov light or as 'charge-collecting' methods, operating in the ion chamber, proportional, streamer, or saturated Geiger modes. In the following discussion, only recent developments or novel applications are emphasized, as witnessed by the choice of a very restricted number of references from the vast amount of literature.

5.1 Homogeneous Calorimeters

Some of the active readout materials have a density that is high enough for them to be used as homogeneously sensitive calorimeters. The properties of most frequently used materials are summarized in Table 7 [54–79].

Among recent noteworthy developments we find:
- a programme to use BGO crystals (amongst the presently known, optically transparent materials, the one with the shortest radiation length) for large 4π photon calorimeters with excellent space and energy resolution [49, 61];
- materials with considerably improved radiation resistance [64, 65, 74, 75];
- the use of BaF_2 crystals, coupled to very fast UV-sensitive light detectors for very high rate applications [73, 74].

5.2 Readout systems for sampling calorimeters

A great and very diversified number of readout systems have been developed, reflecting the desire to tailor the systems performance to a physics application.

Table 7: Properties and Performances of Homogeneous e.m. Shower Detectors

Detector type	NaI(Tl)	CsI(Tl)	BaF_2	$Bi_4Ge_3O_{12}$	Scintillating glass	Lead glass 55% PbO + 45% SiO_2	$Tl(HCO_2)$-liquid 'Helicon'	Liquid argon
Radiation length (cm)	2.59	1.86	2.1	1.12	~ 4	2.36	~ 1.9	14
Density (g/cm^3)	3.7	4.51	4.9	7.13	~ 3.5	4.08	~ 4.3	1.4
Detection mechanism	Scintillation	Scintillation	Scintillation (20% around 210 nm, 80% around 310 nm)	Scintillation	Scintillation	Cherenkov light	Cherenkov light	Ionization charge
Energy resolution (E in GeV)	$\sim 0.015\,E^{-1/2} < 1$ $< 0.015\,E^{-1/4} > 1$	Comparable to NaI(Tl)	Comparable to NaI(Tl)	Comparable to NaI(Tl)	$\sim 0.002\,E^{-1/2}$	$\sim 0.04\,E^{-1/2}$	Comparable to lead glass	$\gtrsim 0.02\,E^{-1/2}$
Principal limitation to $\sigma(E)$	Shower fluctuations optically non-uniform	Similar to NaI(Tl)	Light collection non-uniformities	Similar to NaI(Tl)	Photon statistics	Photon statistics	Photon statistics	Effect of shower fluctuation on electron collection
Signal[a] (photo-el/GeV)	$\sim 10^7$	$\sim 5 \times 10^6$	$\sim 10^6$	$\sim 10^6$	Few $\times 10^3$	10^3	$\lesssim 10^3$ (?)	$\lesssim 2 \times 10^6$
Characteristic time (ns)	250	900	0.6 ; 300	350	~ 70	~ 20	~ 20	$\gtrsim 100$
Rad. damage at appr. dose[b] (Gy)	$\lesssim 10$	$\lesssim 10$	$\sim 10^3$	~ 10	$\sim 10^4$	$\sim 10^2$	$\gtrsim 10^4$	Not measured; expected to be very large
Mechanical stability	Hygroscopic, fragile	Very good	Good	Good	Very good	Very good	Toxic liquid	Cryogenic liquid
References	[54, 55, 57]	[72]	[73, 74]	[61–63]	[64, 65]	[66–69]	[75]	[76–79]

a) Values are approximate, and depend on spectral matching between light source and photon detector.
b) Values are guidelines only and very substantially depending on experiment and measuring conditions.

5.2.1 Light-collecting sampling calorimeters. The renaissance of such calorimeters started with the introduction of cheap 'plastic scintillators' and elegant light-readout techniques using 'wavelength shifters' (WLSs) to replace the technique of scintillator plates individually coupled to a lightguide [80] (Fig. 17a). The principle is indicated in Fig.17b [81–89]. Scintillation light crosses an air gap and enters the WLS, where it is absorbed and subsequently re-emitted at longer wavelengths; a fraction of this 'wavelength shifted' light is then internally reflected to the light detector. This scheme avoids complicated and costly optical contacts between the scintillators and the light collectors, and minimizes dead spaces. A variety of scintillators have been developed for the large calorimeter facilities. They are based on polymethyl methacrylate (PMMA) [90] or polystyrene [30] as the matrix for the primary scintillating agent. The light yield is close to that of more conventional organic scintillators (usually based on a polyvinyl toluene solvent) if certain aromatic compounds, e.g. up to about 20% naphthalene, are added. These new scintillators are more easily mass-produced, hence cheaper, and have superior mechanical properties. Some of the limitations of the WLS method may be removed after further development: better spectral matching between the scintillator emission and the WLS absorption, and also between the WLS emission and the photocathode sensitivity, will increase the number of detected photons, which is marginal in present systems. Related developments might result in the use of thinner yet more uniform WLSs; increased granularity might be achieved with WLSs having spatially

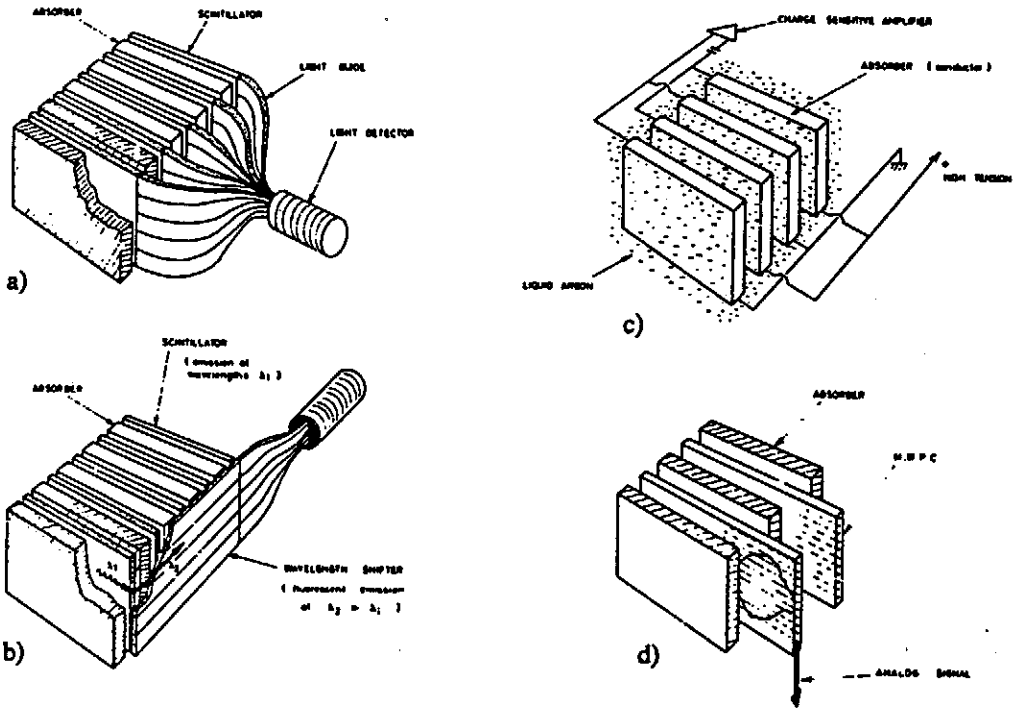

Fig. 17: Schematic representation for frequently used calorimeter readout techniques: a) Plates of scintillator optically coupled individually to a photomultiplier. b) Plates of scintillator read out by photon absorption and conversion in a wavelength shifter plate. c) Charge produced in an electron-transporting medium (e.g. liquefied or high-pressure argon) collected at electrodes, which may also function as the passive absorber plates. d) Charge produced in a proportional gas and amplified internally on suitable readout wires (proportional or saturated gas amplification).

different spectral sensitivities [87], or with very thin foils of WLS [91]. Potentially the most promising developments concern scintillators. They are still rather inefficient (only a few percent of the energy loss is converted into visible photons), and reduced saturation of the response to densely ionizing nuclear fragments should improve the energy resolution of hadron calorimeters (see subsection 3.3). The scintillator properties are important for the energy resolution of calorimeters, and need to be carefully investigated and specified when comparing various seemingly equivalent calorimeters.

Interest in high granularity and very compact readouts has recently led to 'double wavelength-shifter' applications [92–95] (Fig. 18). Although the second shifting reduces the number of photons by a further factor of ~ 5, the compression of the light into a very small cross-section light-pipe is attractive for several reasons, such as small insensitive zones and the possibility to use light detectors with small active areas. Such schemes favour the light registration with vacuum photodiodes [56, 70, 96] or silicon photodiodes [59, 93]. These devices—lacking an internal charge amplification mechanism—are operated with low-noise charge-sensitive preamplifiers, and are therefore more stable compared with photomultipliers; furthermore, they are insensitive to the commonly used levels of magnetic fields (vacuum diodes with some restrictions). These light detectors are therefore particularly attractive for the photon calorimeters of storage ring detectors, which most frequently are operated inside magnetic spectrometer fields [49, 56, 59, 60, 70].

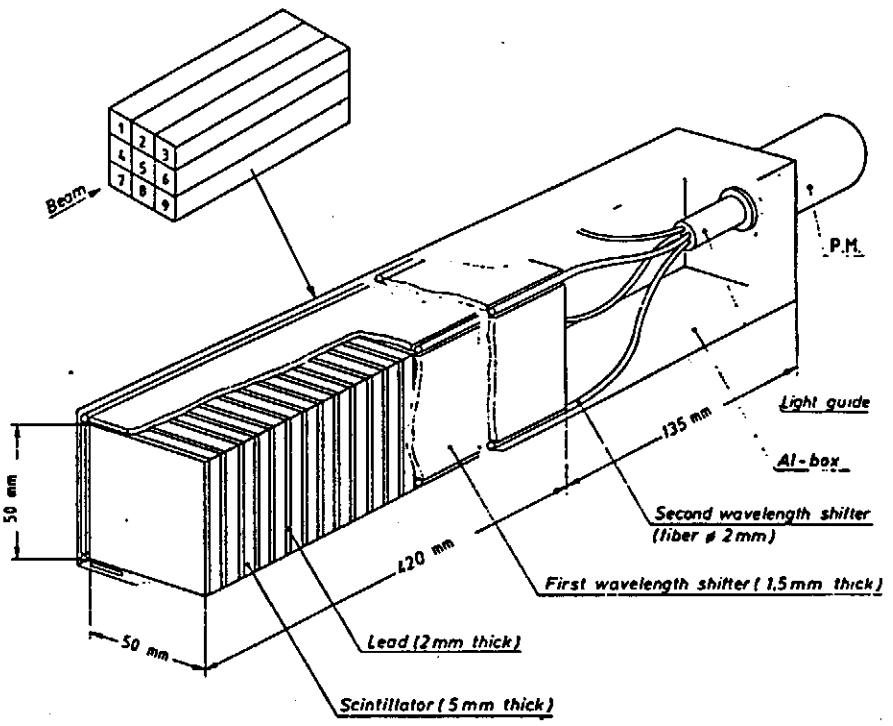

Fig. 18: Schematic view of a 'tower' of a sampling calorimeter array, using double-wavelength shifting techniques for the light measurement. The thin plates of the first WLS cover all four sides of the tower, whereas the second WLS, in the form of a fibre, registers the light emerging from the first shifter and guides it to the photomultiplier [92].

Another line of study concerns the innovative use of scintillators. Very long, narrow, Teflon tubes filled with liquid scintillator have been used for a large photon calorimeter [97]. The Teflon tubes define the spatial granularity of the active element and guide the light through total internal reflection to photomultipliers. A logical refinement consists in using small scintillating fibres [98] embedded in a metal matrix. With this technique a photon detector was constructed with the very short average radiation length of $X_0 = 14.5$ mm and an energy resolution of $\sigma_E/E = 0.11/\sqrt{E}$—the modest man's BGO [99].

In recent years considerable effort was devoted to minimizing two disadvantages of the scintillator readouts; namely, the inherent non-uniformity in the light collection, and the difficulty of energy calibration.

The principal source of non-uniform light collection is not primarily the attenuation of light propagating in thin scintillator sheets, but is usually due to the light collection geometry. The non-uniform response, measured for example by scanning the active surface with a monochromatic electron beam, is at a level of ±5% in finely tuned instruments [32], and one representative example is shown in Fig. 19. Such a level of non-uniform response will of course influence the energy resolution for electrons with $p \geq 10$ GeV/c, if no correction for the impact point is applied. Hadron showers are much less affected, if the geometric extension of the non-uniformities is comparable to or smaller than the shower size. Such problems may be considerably aggravated if the usually sufficiently high transmission of the scintillator is affected, e.g. by radiation damage [32], surface cracking, or for other reasons. Plastic scintillators will show radiation damage after exposure to less than 100 Gy, if in contact with air [100], whilst toluene-based scintillator may sustain approximately 10 times more radiation [101, 102] before its usefulness is severely limited. Closely connected with these problems of light collection is the strategy of relative and absolute energy calibration. For precision applications, it is necessary to expose each calorimeter cell at least once to some kind of particle beam in order to establish an absolute calibration, which subsequently has to be transferred and maintained with some kind of absolutely stable light source. This light source is usually an external reference lamp, whose output is distributed to the calorimeter cells [103]. In some cases, the light produced by internal radioactive sources [32] has served this purpose.

The limitations outlined here become a major concern for applications where very high energy deposits could, in principle, be measured at the one percent accuracy level [50, 95, 104] and correspondingly benefit the quality of the physics data.

Increasingly, therefore, the experimental teams are evaluating alternative solutions, as discussed in the next subsection.

5.2.2. Charge collection readout. The ionization charge produced by the passage of the charged particles of the shower may be collected from solids, liquids, or gases. Solids [105] and liquids can only be used in an ionization chamber mode with no internal amplification. The best known and, to date, the only practical example is based on the use of liquid argon [106]. In specific cases, liquid xenon may be used [107–110]. The use of room-temperature liquids has also been repeatedly advocated [95, 111], but with increasing operating temperature the tolerable level of impurities decreases strongly. If gas is used as the active sampling medium, internal amplification to various degrees is usually exploited: proportional chambers or tubes provide a signal proportional to the

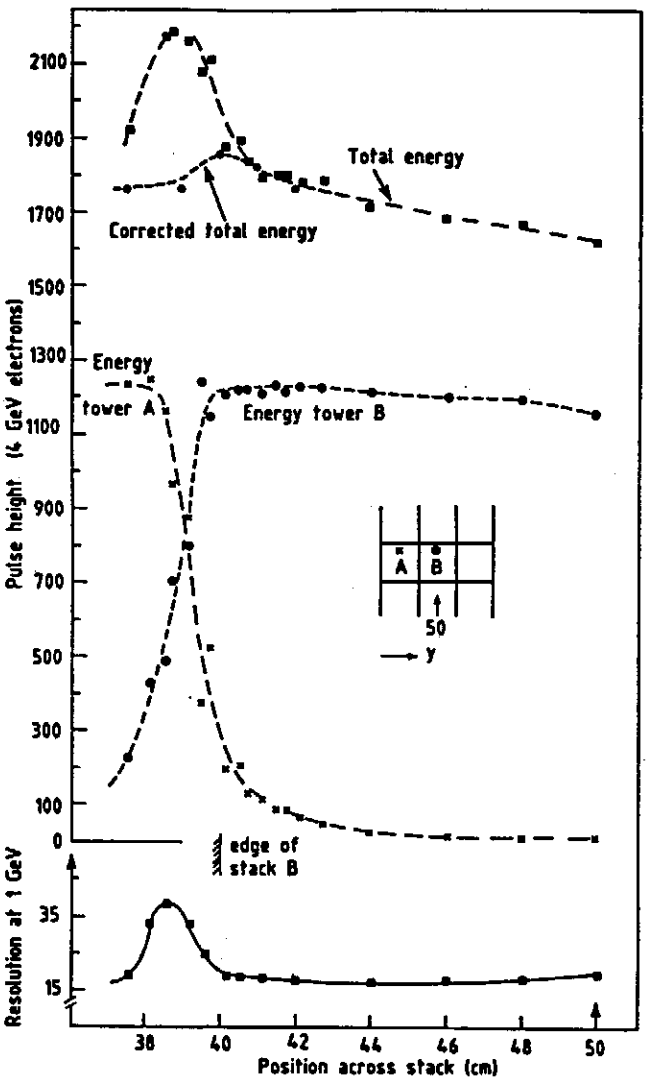

Fig. 19. The worst-case optical non-uniformity obtained by scanning with a 4 GeV/c electron beam under normal incidence across the gap between neighbouring stacks. The approximately 15% non-uniformity can be further reduced with a correction algorithm using the two signals in each tower, A and B (short-dashed curve) [32].

energy loss. At higher gas gain, with devices operating in a controlled streamer or Geiger mode, the measured signal is related to the number of shower particles which traverse the active medium ('digital readout') [112]. The conceptual arrangements are shown in Fig. 20.

The principal advantages common to all these charge collection methods are seen in the ease of segmentation of the readout and the capability to operate in magnetic fields. Some features specific to the various types are:

a) operation in the ionization mode, i.e. liquid-argon calorimeters, provides the best control of systematic effects [44, 113–116];

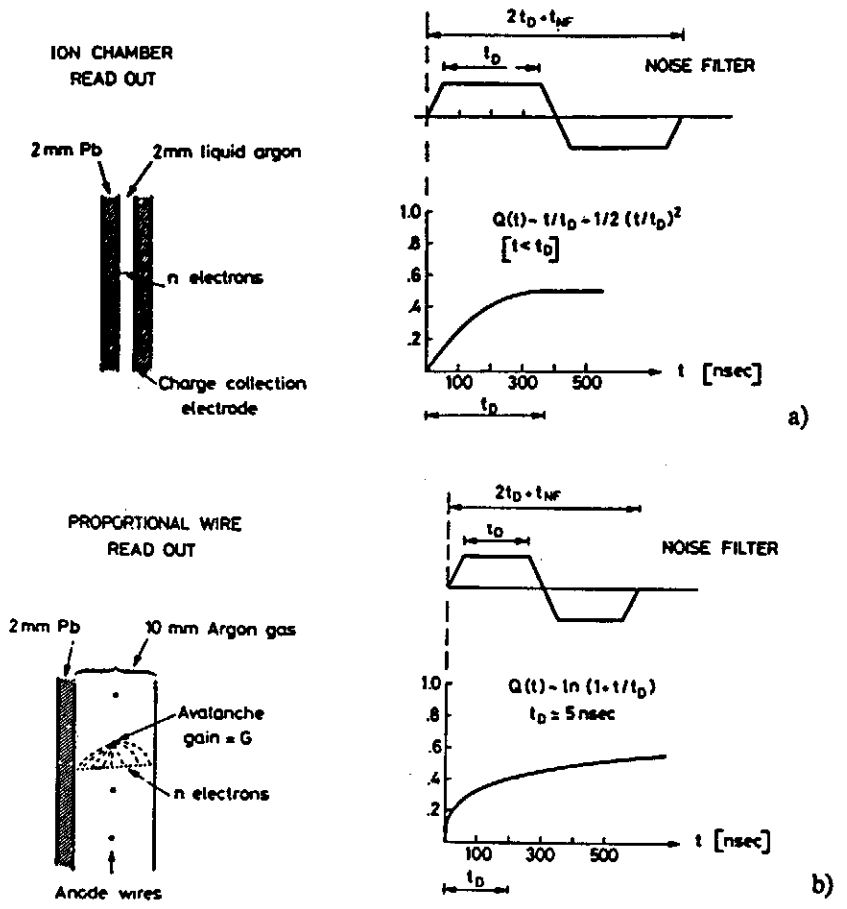

Fig. 20: Charge collection in a single sampling layer for a) a liquid-argon calorimeter with ion chamber readout; b) gas proportional wire readout. The signal charge Q(t) is shown as a function of time, and t_D is the time required for all ionization electrons to be collected. For each case a bipolar noise-filter weighting function is indicated (see text).

b) gas proportional devices offer a wide variety of relatively inexpensive construction methods [117];
c) digital operation, in the Geiger or streamer mode, allows for very simple and cheap signal-processing electronics [112, 118, 119].

The ion chamber technique is the preferred solution whenever optimum performance is at a premium because it excels in the following points, all of which have been realized in practice in devices using liquid argon as the active medium:

- uniformity of response at the fractional percent level;
- ease in fine-grained segmentation with a minimum of insensitive area;
- excellent long-term operating stability (radiation damage absent in liquid argon; response of active medium controllable).

Experimentation at today's fixed-target or storage ring facilities often justifies the use of such high-performance calorimeters, and as a consequence the liquid-argon ion chamber technique has been adopted for several large facilities, both in existence [44, 113–116] or planned [51, 120, 121]. One noteworthy exception is made by the teams preparing the four LEP detectors—they have opted for scintillator or proportional chamber readout solutions.

For many years, several liquid substances have been known, in which electrons may be drifted over large (several centimetres) distances, given adequate electric fields and levels of purity [122]. Generally, it may be said that operation at cryogenic temperatures, $T < 100$ K, eases the purification problem. Liquid-argon calorimeters, for example, may be operated with levels of $\sim$ 1 ppm O_2, but the requirements are already considerably more severe for liquid xenon ($\sim$ 10 ppb O_2 tolerable) and develop into a major engineering difficulty for room-temperature liquids [95, 123]. In practical applications one has to weigh the complexity of a cryogenic detector (difficult access to components inside, extra space for the cryostat, increased mechanical engineering problems) against the difficulties arising from impurity control (large multistage purification plant, use of ultra-high vacuum techniques and components in the construction) [123]. It was thought that some of the lighter room-temperature liquids [such as tetramethylsilane (TMS)] might be intrinsically more advantageous for hadron calorimeter readouts, because one expected relatively small saturation for densely ionizing particles (e.g. recoil protons) [124]. Recent measurements [95, 125] however, have indicated that in practical electric drift fields such an advantage may not exist.

The very low cost of sufficiently pure liquid argon and the relative ease of maintaining it in operating conditions suggest its use in large-mass detectors for neutrino-scattering or proton-decay experiments [77–79, 126]. As with all rare-event detectors, the possibility of very large drifts of the ionization [time projection chamber (TPC)] have been studied with the aim of reducing the number of electronic channels to an 'acceptable' level [76, 77].

A recent extension of the ion chamber techniques to the use of solid dielectrics has met with considerable success [127], the signal being measured with Si surface barrier detectors in sampling calorimeter detectors. This scheme combines the advantages of a room-temperature ion chamber readout, with the attractive feature that these Si detectors are usually extremely thin, less than 500 μm, permitting the realization of detectors with $X_0 \leq 4$ mm, and hence offering the ultimate localization of showers.

For ion chambers and proportional wire readout, the measured signal typically amounts to a few picocoulombs of charge per GeV of shower energy. Since sampling calorimeters are inherently devices having a large capacitance, the optimum charge measurement requires careful consideration of the relationship between signal, noise, resolving time, and detector size. A detailed noise analysis gives [128]

$$\mathrm{ENC_{opt}} = k \times 10^6 (C_D/t_{NF})^{1/2},$$

the 'equivalent noise charge' ENC being the input signal level which gives the same output as the electronic noise. The parameter k is proportional to the r.m.s. thermal noise of the input field-effect transistor; for practical detector arrangements a value of $k \simeq 5$ is realized. [C_D is the detector capacitance (in μF), and t_{NF} is the noise filter-time (in ns)]. This relation determines the fundamental lower limit to the noise, which is achieved

with optimal capacitance matching between the detector and amplifier. The noise figure grows with increasing detector capacitance, but can be reduced at the expense of augmenting the resolving time.

Charge collection in gases, usually followed by some degree of internal amplification, forms the basis of another important category of calorimeter readouts [117]. The method lends itself naturally to highly segmented construction, of particular value for the topological analysis of the energy deposit (e.g. γ/hadron discrimination, muon identification). The technique has profited from the diversified developments in gaseous position detectors [129] over the last fifteen years: the versatility of arranging readout anode wires combined with the ease of gain control have produced a great variety of different solutions tailored to the specific requirements of an experiment.

With these types of detectors, spatial segmentation and localization can be easily implemented. This may be achieved in a projective geometry using strips, or in a 'tower' arrangement, e.g. by measuring the signal charge induced on a pattern of cathode pads [130, 131]. The tower arrangement is mandatory for reducing ambiguities and confusion in multiparticle events.

Another technique, currently being pursued, aims at achieving a very high degree of spatial segmentation, and uses a TPC method, the so-called 'drift-collection' calorimeter [132]. The ionization produced by the charged particles of a cascade is drifted over very long distances and collected on a relatively small number of proportional wire planes, equipped with a two-dimensional readout, while the third shower coordinate is determined by a drift-time measurement. The conceptual configuration is shown in Fig. 21. An example of the pictorial quality of shower reconstruction expected with this technique is given in Fig. 22.

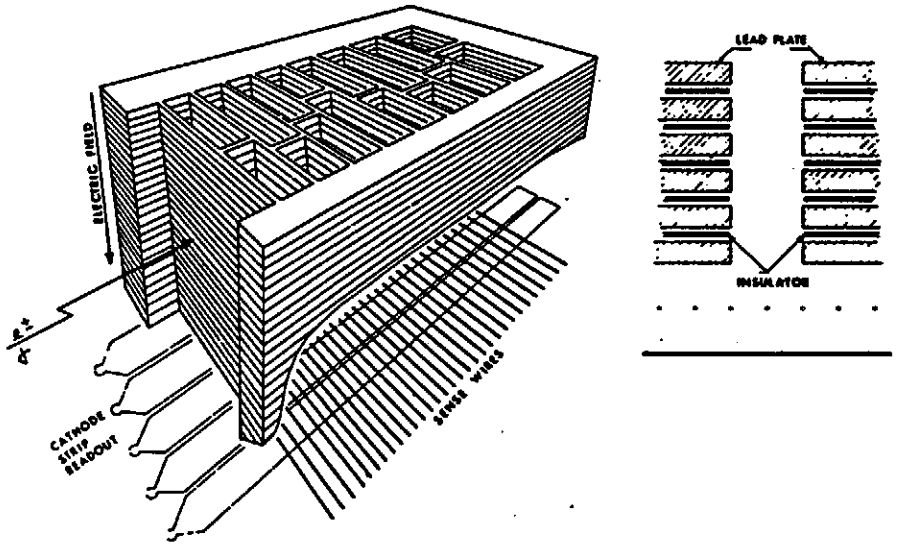

Fig. 21: Geometrical arrangement for the high-density drift calorimeter. Cavities between absorber plates allow the drifting of ionization electrons over long distances on to MWPC-type detectors. Very high spatial granularity can be achieved at the cost of mechanical complexity and rate capability. A very uniform magnetic guidance field parallel to the drift direction is usually required [132].

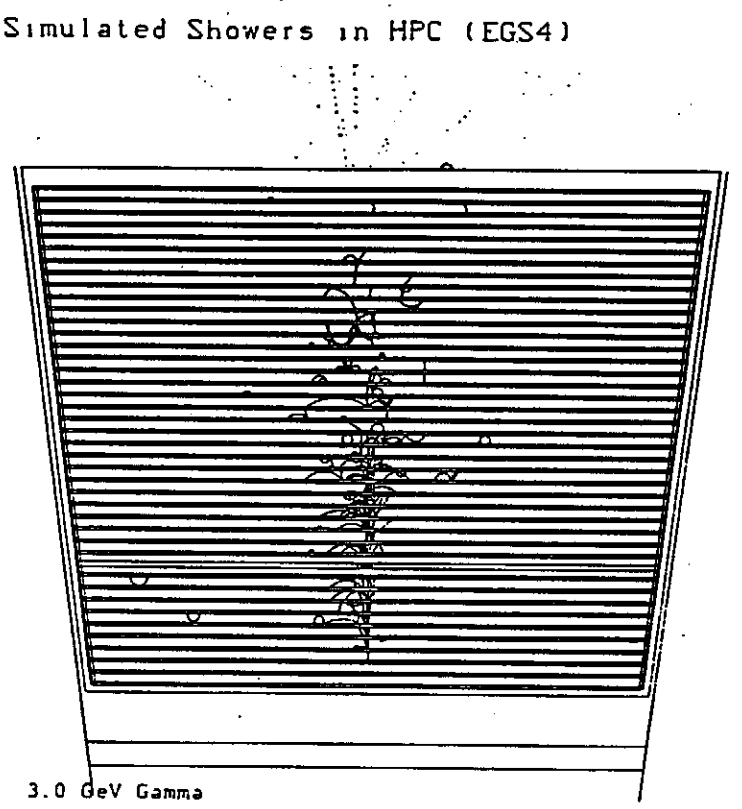

Fig. 22: Simulation of an electromagnetic shower in the calorimeter of the LEP DELPHI collaboration using EGS IV. The bubble-chamber-like pictorial quality of the information allows the individual shower particles to be distinguished. (Courtesy of H. Burmeister, CERN.)

Gas sampling calorimetry in a digital mode (using Geiger, streamer, or flash-tube techniques) is a means of simplifying the signal processing circuitry, and offers an expedient method for achieving a high degree of segmentation. Flash chambers consist of an array of tubular cells filled with a mixture of about 96% neon + 4% helium; a pulsed high-voltage is applied across each cell after an external event trigger. In the presence of ionization charge, a signal-producing plasma discharge propagates over the full length of the cell. In one such array for a large neutrino experiment at Fermilab, 608 flash-chamber planes with a total of some 400,000 cells are sandwiched between absorber layers of sand and steel shot [24]. The pattern of struck cells in each plane is read out by sensing induced signals on a pair of magnetostrictive delay lines. Wire readout planes may also be operated in the 'streamer mode', where the charge gain is controlled to cover only a segment around the particle impact point [133, 134]. Common to these saturated gas-gain readout schemes are the following properties:

- the energy resolution is in principle better than in a proportional gain system, because Landau fluctuations are reduced or suppressed;
- the mechanical tolerances of the readout system are less stringent than for proportional systems;

- these readouts are inherently non-linear. One charged particle causes an insensitive region along the struck wire, which prevents other nearby tracks from being registered. Typically, non-linearities become measurable above ~ 10 GeV.

Usually, care is taken to limit the geometrical extension of the discharge region, e.g. with various mechanical discontinuities (beads, nylon wires, etc.). A calorimeter operated in this mode gave an energy resolution of $\sigma \simeq 14\%/\sqrt{E}$ for electron energies up to 5 GeV [135]. This is better than is normally achieved for gas sampling calorimeters, reflecting the absence of Landau and path-length fluctuations. At higher energies the calorimeter showed saturation effects due to the increasing probability of multiple hits over the geometrical extension of the discharge region.

The *rate capability* of calorimeters is an important parameter for high-rate fixed-target experiments or the planned hadron colliders (Table 8) [136]. Several different time constants characterize the readout:

1) 'occupation' time specifies the length of time during which the physical signal produced by the particle is present in the detector (pulse length);
2) 'integration' time corresponds to the externally (e.g. electronically) chosen time defining the bandwidth of the signal processing system;
3) 'time resolution' specifies the precision with which the impact time of a particle may be determined.

For scintillator-based methods the signal duration is typically about 20–50 ns but, with special care, signals of about 10 ns length have been achieved [94].

For liquid-argon devices, the charge-collection time is ~ 200 ns/mm gap; it may be reduced by a factor of 2 by adding ~ 1% of methane. Sometimes it is acceptable not to integrate over the full signal length, entailing a reduction in the signal-to-noise ratio. For liquid-argon devices, the noise is proportional to $(\tau_{\text{integ}})^{-1/2}$ and the signal is almost proportional to $(\tau_{\text{integ}})^{1/2}$, if $\tau_{\text{integ}} < \tau_{\text{tot. coll.}}$. A very short integration time is sometimes chosen ('clipping' of a signal) to enable very fast trigger decisions; only if the event information is of interest is the signal processed with a longer integration time, in order to obtain an optimum signal-to-noise ratio.

The time resolution achievable with calorimeters may help to associate the calorimeter information with different events, separated by a time interval much shorter than the integration time. For scintillator and liquid-argon calorimeters, time resolutions of 2–3 ns have been measured for few-GeV energy deposits [44, 137].

The ultimate rate limitation is, however, determined by the physics to be studied with a calorimeter. In collisions involving hadrons in the initial state, reactions which occur with very different cross-sections may be characterized by very different event topologies. A typical example is the production of several high-p_T jets in a pp collision, the cross-section of which is very small in comparison with the total inelastic cross-section. In such a case, several events may be recorded within the occupation time of the detector without serious effects (Fig. 23). This figure suggests that calorimeters may still be very useful even if, during the occupation time of an interesting event, several other events produce energy deposits and are recorded in the detector [32, 39, 138].

Table 8: Temporal Response of Readout Systems

Calorimeter system	Occupation time (ns)	Pulse width (integration) (ns)	Timing resolution σ (ns)	Radiation resistance
Metal/scintillator with WLS readout	50	50	2.5 for few-GeV deposit; better at higher energy, if not limited by PM	Depends on scintillator, dose rate, environment; $> 10^3$ Gy appear achievable [102].
^{238}U/scintillator with fast WLS readout	~ 100	100	2.5	As above
Metal/fast scintillator with fast WLS readout	≤ 20	≤ 20	< 2 (?)	
Metal/proportional or saturated gas-gain readout	50–100	100–200 bipolar shaping	≤ 10	Adequate for chamber; lifetime of on-detector electronics may be a limitation; readout elements need to be shielded from U radioactivity.
^{238}U/proportional or saturated gas-gain readout	≥ 100	≥ 200 bipolar shaping	≤ 10	
Metal/LAr ion chamber	~ 200 per 1 mm gap	$2\lambda = 400$ bipolar shaping	~ 2 for few-GeV deposit	Lifetime of on-detector electronics may be a limitation
Metal/LAr–CH_4 ion chamber	~ 100 per 1mm gap	$2\lambda \leq 200$	≤ 2 for few-GeV deposit	NB: shorter pulse width (2λ) possible the expense of signal/noise $\simeq \lambda^{\alpha}$, at $\alpha \sim 1$.

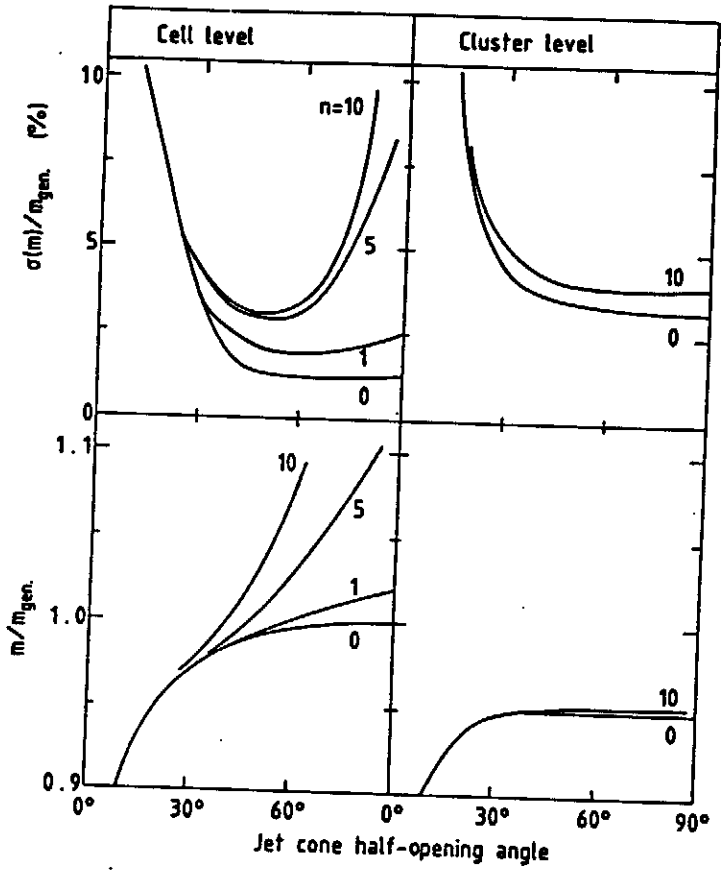

Fig. 23: Two-jet mass resolution (upper part) and reconstructed mass value (lower part) for a 1 TeV system at the cell and at the cluster level as a function of the opening angle between the jets, and the number n of additional accidental minimum-bias events [39] (see Fig. 14 for definition of cell and cluster level).

5.2.3. Bolometric Readout. Repeatedly, particles have been detected through the temperature rise in a calorimeter, caused by the absorption of the particles. Such experiments contributed decisively to our understanding of radioactivity and to the concept of the neutrino [139]. Already 50 years ago it was recognized that owing to the large reduction in heat capacity of many materials at cryogenic temperatures, very sensitive instruments were permitted [140]. More recently, interest has refocused on cryogenic calorimetry, operated in the temperature range of 1 mK to ~ 1 K. Such detectors [141–143] are considered as possible particle detectors offering an energy resolution of $\lesssim$ 10 eV and having a time response in the 100 μsec to 1 msec range. Possible experiments include the search for double-beta decay or the measurement of the end point of tritium beta decay. More ambitiously, multiton silicon detectors operated at mK temperatures are considered as a solar neutrino observatory to measure the spectrum of solar neutrinos and to probe for neutrino mass differences at the 10^{-6} eV level. Cryogenic calorimetry promises far more precise energy measurements than any of the other 'standard' techniques and allows us to contemplate some of the most challenging and fundamental experiments in particle physics.

6. SYSTEM ASPECTS OF CALORIMETERS

6.1 General Scaling Laws of the Calorimeter Dimensions

A number of parameters which may be external to the calorimeter design, e.g. the dimensions of a charged-particle spectrometer, may ultimately determine the size of a calorimeter.

If, however, global optimization of an experiment is attempted, one should aim for the most compact calorimeter layout that may lead to the achievement of the physics goals of the detector.

The distance D of a calorimeter from the interaction vertex, and hence its necessary size, is determined by the achievable useful segmentation and the characteristic angular dimension θ required to be resolved in the measurement. The useful segmentation d is determined by the shower dimensions, approximately $d \sim 2\varrho_M$ for electromagnetic detectors and $d \sim \lambda$ for hadronic ones. The characteristic angular dimension θ may be the minimum angular separation of the photons from π^0 decay, or the typical angle between the energetic particles in a hadron jet.

For correctly designed detector systems, the calorimeter dimensions are determined by the angular topology and size of the showers to be measured. The minimum detector distance is then $D \geq d/\mathrm{tg}\,\theta$, and the required calorimeter volume V is found to be

$$V \propto D^2 \times L \text{ (depth of calorimeter required for total absorption)}$$

whence

$$V \propto \varrho_M^2 \times X_0 \text{ for e.m. detectors,}$$

and

$$V \propto \lambda^2 \times \lambda \text{ for hadronic detectors.}$$

The third-power dependence of the calorimeter volume on shower dimensions implies that it may be economically advantageous to select very compact calorimeter designs, even if the price per unit volume is very high. Table 9 explains why sometimes only the most expensive materials (per cm^3) can be afforded.

6.2. Calorimeter Systems for Physics Applications

6.2.1 Neutrino physics and nucleon stability. Detectors for these studies share some common features: the event rate is low and is proportional to the total instrumented mass; the physics requires a fine-grained readout system, which permits detailed three-dimensional pattern reconstruction. Bubble chambers have therefore been used extensively but are limited by the long analysis time per event. The present generation of neutrino detectors makes extensive use of wire-chamber techniques to approach the intrinsic spatial and angular resolution of calorimeters. New 'visual' electronic techniques are being developed for proton decay experiments, for which very massive detectors with a high density of signal channels are required.

A neutrino detector, even when exposed to present-day intense neutrino beams, must have a very large mass (typically hundreds of tons), and its volume must be

Table 9: Characteristic Dimensions and Price Comparisons for e.m. Calorimeters

Material / Quantity	NaI	BGO	U/Si sampling calorimeter
X_0 (mm)	26	11	4
ϱ_M (mm)	44	23	11
Reference volume (cm^3) for 95% containment of ~ 5 GeV electrons	1600	180	15
Approx. price/Ref. vol. (arbitrary units)	1	1	0.1

uniformly sensitive to the signature that an interaction has occurred and to the characteristics of the reaction products. These requirements explain the modular construction typical of modern electronic neutrino detectors. The general form of the interaction is $\nu_{(\mu,e)}$ + nucleon = $\ell_{(\mu,e)}$ + X, where ℓ is a charged lepton (charged-current interaction) or a neutrino (neutral-current interaction), and X represents the hadronic system. The signature for a neutrino interaction is the sudden appearance, in the detector, of a large amount of energy in a few absorber layers. If the scattered lepton is a muon, it leaves in each layer the characteristic signal of a single minimum-ionizing particle. In some detectors the absorber layers are magnetized iron, which makes possible a determination of the muon momentum from the curvature of its trajectory. For a detailed study of neutral-current interactions, a very fine grained subdivision of the calorimeter system is required for measuring the energy and direction of the hadronic system X and for reconstructing the 'missing' transverse momentum of the final-state neutrino.

Clearly the scope and sensitivity of neutrino experiments would be much improved if even the most massive detectors could resolve final state particles with the reliability and precision typical of a bubble chamber. With this goal in mind, some schemes are currently being investigated that use drift chamber methods with large volumes of liquid argon [79], which provides a visual quality characteristic of homogeneously sensitive detectors. In another case [144] a cylindrical detector, 3.5 m in diameter and 35 m long, is foreseen, containing about 100 tons of argon gas at 150 atm pressure, with ionization electrons collected on planes of anode wires. The idea has also been advanced [145] of using compressed mixtures of more common gases (air or freon), large liquid-argon TPCs [78], or room-temperature liquid hydrocarbons [146] to detect the ions that migrate away from charged-particle tracks (positive and/or negative ions produced by electron attachment).

Detectors to search for the decay of nucleons are also characterized by a very large instrumented mass, varying from a hundred to several thousand tons. Current theoretical

estimates place the proton lifetime at around $\tau_p \simeq 3 \times 10^{29 \pm 1.5}$ y compared with present experimental limits [147] of $\tau_p \geq 10^{32}$, reached by detectors of at least 1000 tons mass, or approximately $> 10^{33}$ nucleons. These detectors have to be instrumented to search sensitively for some of the expected decay modes such as $p \rightarrow e^+ + h^0$, where h^0 is a neutral meson (π^0, η, ϱ^0, ω^0). The signature of such a decay is clear, provided a detector is sufficiently subdivided to recognize the back-to-back decay into a lepton and a hadron with the relatively low energy deposit of about 1 GeV. The sensitivity is limited by the flux of muons and neutrinos originating from atmospheric showers. Only muons can be shielded by placing the experiments deep underground in mine shafts or in road tunnels beneath high mountains. The ν_μ-induced rate simulating nucleon decay is estimated at $\sim 10^{-2}$ events per ton per year if energy deposition alone is measured. If complete event reconstruction is possible, an experimental limit of $\tau \geq 10^{33}$ y may be reached [147].

The most massive calorimetric detectors to date have been conceived to explore the very high energy cosmic-ray spectrum. The detector volumes needed are so large that only the sea water [148] and air [149] are available in sufficiently large quantities. The interaction provoked by cosmic-ray particles is detected through the Cherenkov radiation emitted in the ensuing particle cascade in the case of the deep underwater array. In the case of the atmospheric detector it is the light from the excited N_2 molecules which is detected and measured with great ingenuity. The 'air calorimeter' represents the largest ($V \simeq 10^3$ km^3) and most massive ($W \sim 10^9$ tons) calorimeter conceived to date; already it has produced evidence about the cosmic-ray flux at $E > 10^{20}$ eV.

6.2.2. Calorimeter facilities for storage rings. At hadron machines the studies focus on reactions that are characterized by a large transverse energy (E_T) flow, as a signal for an inelastic interaction between the nucleon constituents. The signature appears in many different characteristic event structures and may therefore be efficiently selected with hadron calorimeters : examples are single high-p_T particles, 'jets' of particles, or events exhibiting large E_T, irrespective of their detailed structure. Topical applications include invariant mass studies of multijet events, often in conjunction with electrons, muons, or neutrinos (missing E_T). The power of this approach has been demonstrated by the results obtained in recent years at the CERN $p\bar{p}$ Collider [52], which in turn have led the UA1 and UA2 collaborations to proceed with major upgradings or replacements of their calorimeter detectors [95, 150]. This central role of calorimetry in exploratory hadronic physics programmes [39, 151, 152] is also recognized in the planning for the second detector facility for the FNAL Tevatron. The group is planning a 400 ton uranium/liquid-argon hadron calorimeter, which is expected to be the most advanced calorimeter facility in use during the coming years [51].

At electron–positron colliders, electromagnetic detectors are frequently used to measure the dominant fraction of neutral particles, the π^0's. They are also the ideal tool for detecting electrons, which may signal decays of particles with one or more heavy (c, b, ...) quarks. Unique investigations of cc and bb quark spectroscopy were accomplished with high-resolution NaI shower detectors [153].

For the physics programmes at LEP [154–156] and at the SLAC Linear Collider [120, 157] extensive use of hadron calorimetry will be made. At e^+e^- machines the event topology—production of particles at relatively large angles, with a total energy equal to the centre-of-mass (c.m.) collision energy, favours the experimental technique of total energy measurement. For future e^+e^- physics this method will be important because

- the fraction of neutron and K_L^0 production, measurable only with hadronic calorimeters, increases with energy [158];

- a large and most interesting fraction of events will contain neutrinos in the final state; missing energy and momentum analysis provides the sole handle for such reactions;

- a considerable fraction of events will show good momentum balance but large missing energy—these may be two-photon events or, above the Z^0 pole, events on the radiative tail; total energy will provide the cleanest signature;

- hadronic calorimeters will be the most powerful tool for measuring the reaction $e^+e^- \rightarrow W^+W^-$, either in channels where each W decays hadronically (a total of four jets) or through leptonic decay channels;

- most importantly, a measurement of energy topology is a powerful way of unravelling very rare and unexpected physics phenomena [159].

The technically most difficult requirements for the calorimetry will be imposed by the physics programme at HERA (DESY, Hamburg) [160]. Owing to the very asymmetric energy of the beams (800 GeV protons on 30 GeV electrons), the jets of particles fragmenting from the scattered quarks will have to be measured with the greatest possible energy and *angular* precision in a geometry similar to that of a fixed-target experiment. This implies that the detectors will have a very asymmetrical arrangement, a very large dynamic range, and very high granularity. Innovative developments [93, 127] signal the HERA groups' anticipation of this challenge.

At e^+e^- machines the performance with respect to the energy and space resolution of a well-designed calorimeter is matched to the physics programme foreseen at LEP and at the SLC. Consider, as an example, a 100 GeV multijet event of which the total energy can be measured with an accuracy of $\sigma \simeq 3$–5 GeV and the total momentum balance checked at a level of $\sigma \simeq 3$ GeV/c. These are intrinsic performance figures, disregarding possible instrumental effects (see Section 3). At hadron colliders, however, a further serious difficulty arises from the convolution of the energy response function with the steeply falling p_T distribution of hadronically produced secondaries [161–164]. As a consequence, the measured energy deposit E′ in the detector will originate predominantly from incident particles with energy $E < E'$; count rates and trigger rates are higher than the true physics rates. The result can be devastating for detectors with poor energy resolution or a non-Gaussian response function ('tails' in energy resolution), introducing large errors in the deconvolution. The problem is compounded if the calorimeter response is different for charged and neutral pions (see Section 3): without adequate precautions, these detectors would preferentially select π^0's, making the use of calorimeters marginal for general trigger applications.

The trigger capability is a unique and perhaps the most important requirement of hadron calorimeters employed at hadron machines. For satisfactory operation, one needs uniform response irrespective of event topology and particle composition; good energy resolution at the trigger level to minimize effects of the response function; and adequate granularity for the selection of specific event topologies. For high selectivity, rather complex analogue computations are required, as may be seen from the examples in Table 10 [165]. A tabular summary on calorimeter facilities may be found in Ref. [3].

Table 10: Triggering with Hadron Calorimeters

Experiment	Trigger
Single-particle inclusive distribution; correlations	Localized energy deposit in spatial coincidence with matching track; several thresholds used concurrently.
Jet studies	Extended (~ 1 sr) energy deposit; several thresholds and multiplicities.
Inclusive leptons, multileptons	Electromagnetic deposit in spatial coincidence with matching track; several thresholds and multiplicities.
Heavy flavour jets; correlations	Various combinations of above triggers.

6.3 Monte Carlo Simulations

The development of calorimeters from crudely instrumented hadron absorbers to finely tuned precision instruments owes much to the development of a number of simulation codes. The relatively simple physics governing the electromagnetic showers has facilitated their Monte Carlo simulation. Today, one program has emerged as the world-wide standard for simulating e.m. calorimeters [166]. It has progressed through several improvement stages up to the currently used version, EGS IV, which allows one to follow the shower history, tracking electron pairs down to zero kinetic energy and photons down to ~ 100 keV. It has successfully passed many very detailed tests, including the perhaps ultimate one, that of simulating absolutely the response of electrons relative to muons [167].

The physics and consequently its simulation are considerably more complex for hadronic showers. Over the last decade several programs have been developed, the aim of which is to simulate fairly accurately the detailed particle production of a hadronic cascade [25, 168, 169]. As an example, the flow chart of one of the most detailed simulations is shown in Fig. 24. The attentive reader will no doubt realize that even the most faithful physics simulation of the hadronic process will not guarantee unconditional success. Already the uncertainties associated with the sampling medium (relative response to minimum and heavily ionizing particles) and the complexities of the nuclear interactions are too large to make an *ab initio* calculation possible at present. These programs therefore do require careful tuning against many different measurements, before they become a reliable guide for designing new facilities. The results of a sample calculation are shown in Fig. 25 and give an impression of the power of this code. The status of these shower calculations has recently been extensively discussed [170].

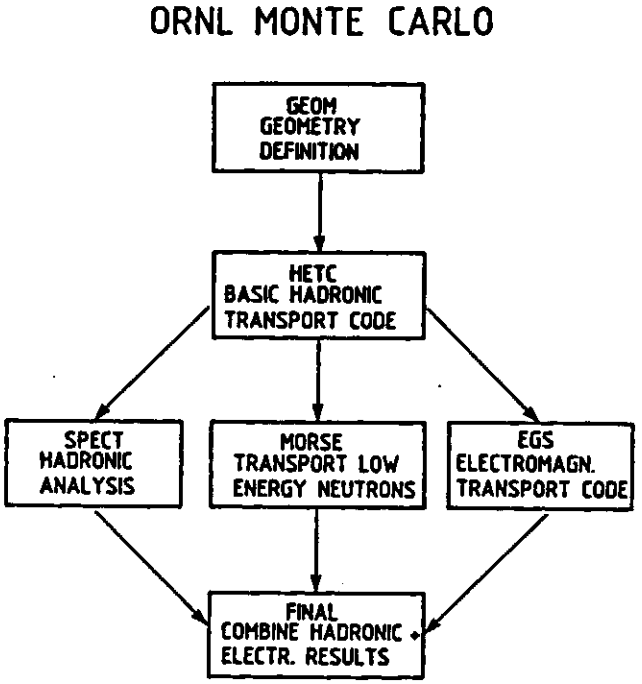

Fig. 24: Flow chart of the hadronic cascade Monte Carlo [T.A. Gabriel et al., Nucl. Instrum. Methods 195:461 (1982)].

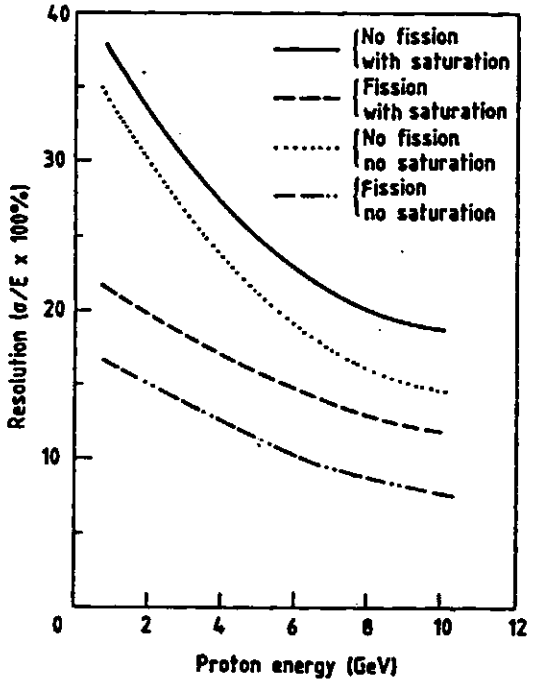

Fig. 25: Results of a 'Gedanken-experiment' using HETC to study the importance of the fission contribution and its manifestation is different readouts, with and without saturation [T. Gabriel et al., Nucl. Instrum. Methods. 164:609 (1979)].

7. OUTLOOK

The use of calorimetric methods in high-energy physics began with rather specialized applications, which capitalized on some unique features not attainable with other techniques: electromagnetic shower detectors for electron and photon measurements; neutrino detectors; and muon identifiers.

The evolution towards a more general detection technique—similar in scope to magnetic momentum analysis—had to wait for extensive instrumental developments driven by strong physics motivations. The application of this technique to the hadron storage rings (which were inaugurated in the early 1970's) was therefore delayed, but it has shaped the detectors for the CERN $p\bar{p}$ Collider and has proved to be of major importance for the detector facilities currently in preparation. At the same time, physics studies have evolved along lines where measurements based on 'classic' magnetic momentum analysis are supplemented or replaced by analyses which are based on precise global measurements of event structure, frequently requiring extraordinary trigger selectivity, and which are much more suitable for calorimetric detection. During the next decade, experiments will rely increasingly on these more global studies, with properties averaged over groups of particles and with the distinction between individual particles blurred, unless they carry some very specific information. This role of calorimetry in both present and planned physics programmes is summarized in Table 11; the impact of instrumental advances and technology is outlined in Table 12.

Table 11: Future Role of Absorptive Spectroscopy

Source of particles	Physics emphasis	Calorimeter properties	Technical implications
pp ($p\bar{p}$) collider	Rare processes: high-p_T lepton, photon production; manifestations of heavy quarks $W^{\pm}$, Z^0, ...	$\sim 4\pi$ coverage with e.m. and hadronic detection; high trigger selectivity	Approach intrinsic resolution in multicell device; control of inhomogeneities, stability
e^+e^- collider	Complex high-multiplicity final states (multi-jets, electrons in jet, neutrinos)	Precision measurements of total visible energy and momentum	Very high granularity; particle identification
ep colliders (secondary beams, $p \geq 1$ TeV/c)	High-multiplicity final states; strong emphasis on global features	Calorimeter becomes primary spectrometer element	High granularity, high rate operation
Penetrating cosmic radiation; proton decay	Detailed final-state analysis of events with extremely low rate	Potentially largest detector systems ($\geq$ 10,000 tons) with fine-grain readout	Ultra-low-cost instrumentation

Table 12: Interdependence of Detector Physics and Technologies for Calorimeters

Principles	Electronics	Mode of operation
Improved understanding of limitation to energy resolution in hadron calorimeters	Gain stability at ~ 1% gain monitoring at 0.1% of ~ 10^5 analogue channels	
Calorimeters replace magnetic spectrometers at high energies	Operational systems of ~ 10^5 light- or charge-measuring channels	Very high spatial resolution for electromagnetic and hadronic showers
Particle identification through energy deposit pattern (μ, e, γ, π^0, n, $\bar{p}$, K_L^0, ν)	Cheap, fast ADC for high-level fast trigger decisions	Helps or allows pattern recognition of very complex events (jets, ...)

Despite recent conceptual and technical progress, a number of questions deserve further attention:

1) What is the precise energy dependence of hadronic energy resolution?
2) What improvement in energy, position, and angular resolution could be obtained with complete information on the individual shower distributions? With such information, could we minimize the effect of increased longitudinal leakage on the energy resolution?
3) What contributes to the measured energy resolution $\sigma(E) = 0.2 \times E^{-1/2}$ of a fission-compensated hadron calorimeter?
4) Is there a cure for the low-energy non-linearities?
5) Can we understand hadronic sampling fluctuations to the same degree as we understand electromagnetic ones?
6) Can particle identification and separation be improved if more detailed shower information is available?
7) Are there any advantages in mixing different absorber materials, or in changing the sampling step inside a calorimeter?
8) Can we tailor the signal response of the readout to improve the calorimeter response?

The very diverse applications of calorimetric techniques will ensure continued study of these and the many technical questions connected with the signal processing of calorimeter information. There can never be a unique solution, but there should always be a search for the most suitable method. We hope that the information provided in this review will be useful for attaining this goal.

ACKNOWLEDGEMENTS

I wish to express my appreciation to Professor T. Ferbel who, as director of the 'Advanced Institute', has developed a School, which by its size, its students, its style, and its 'ambiance' appears optimally conducive to the pursuance of a variety of very topical themes.

R. Wigmans helped me considerably with a critical reading of these notes. C. Comby, L. Karen-Alun, M. Mazerand, M.-S. Vascotto, and K. Wakley efficiently and cheerfully converted my manuscript into printable form.

REFERENCES

[1] V.S. Murzin, Progress in elementary particle and cosmic-ray physics, J.G. Wilson and I.A. Wouthuysen, eds., North Holland Publ. Co., Amsterdam (1967), Vol. 9, p. 247.

[2] M. Atac, ed., Proc. Calorimeter Workshop, Batavia, 1975, FNAL, Batavia, Ill. (1975).

[3] C.W. Fabjan and T. Ludlam, Ann. Rev. Nucl. Part. Sci. 32:335 (1982).

[4] U. Amaldi, Phys. Scripta 23:409 (1981).

[5] S. Iwata, Nagoya University report DPNU-3-79 (1979).

[6] H. Messel and D.F. Crawford, Electron-photon shower distribution: Function tables for lead, copper and air absorbers, Pergamon Press, London (1970).

[7] Y.S. Tsai, Rev. Mod. Phys. 46:815 (1974).

[8] B. Rossi, High-energy particles, Prentice Hall, New York (1964).

[9] E. Longo and I. Sestili, Nucl. Instrum. Methods 128:283 (1975).

[10] H.H. Nagel, Z. Phys. 186:319 (1965).

[11] D. F. Crawford and H. Messel, Phys. Rev. 128:2352 (1962).

[12] Yu.D. Prokoshkin, Proc. Second ICFA Workshop on Possibilities and Limitations of Accelerators and Detectors, Les Diablerets, 1979, U. Amaldi, ed., CERN, Geneva (1980), p. 405.

[13] E.B. Hughes et al., IEEE Trans. Nucl. Sci. NS-19: 126 (1972).

[14] H.G. Fischer, Nucl. Instrum. Methods 156:81 (1978).

[15] R.W. Sternheimer et al., Phys. Rev. B3:3681 (1971).

[16] K. Pinkau, Phys. Rev. B139:1548 (1965).

[17] T. Yuda, Nucl. Instrum. Methods 73:301 (1969).

[18] C.J. Crannel, Phys. Rev. 182:1435 (1969).

[19] T. Kondo et al., A simulation of electromagnetic showers in iron-lead and uranium-liquid argon calorimeters using the EGS, and its implication for e/h ratios in hadron calorimetry, contributed paper to the Summer Study on the Design and Utilization of the Superconducting Super Collider, Snowmass, Colo. (1984).

[20] G.A. Akopdjanov et al., Nucl. Instrum. Methods 146:441 (1977).
S.R. Amendolia et al., Pisa 80-4.
R. Rameika et al., Measurement of electromagnetic shower position and size with a saturated avalanche tube hodoscope and a fine grained scintillator hodoscope, to be published in Nucl. Instrum. Methods.

[21] T. Kondo and K. Niwa, Electromagnetic shower size and containment at high energies, contributed paper to the Summer Study on the Design and Utilization of the Superconducting Super Collider, Snowmass, Colo. (1984).

[22] E. Gabathuler et al., Nucl. Instrum. Methods 157:47 (1978).

[23] A.N. Diddens et al., Nucl. Instrum. Methods 178:27 (1980).

[24] D. Bogert et al., IEEE Trans. Nucl. NS-29:336 (1982).

[25] J. Ranft, Particle Accelerators 3:129 (1972);
A. Baroncelli, Nucl. Instrum. Methods 118:445 (1974);
T.A. Gabriel et al., Nucl. Instrum. Methods 134:271 (1976).

[26] R. Bock et al., Nucl. Instrum. Methods 186:533 (1981).

[27] C.W. Fabjan and W.J. Willis, Proc. Calorimeter Workshop, Batavia, 1975, M. Atac ed., FNAL, Batavia, Ill. (1975), p. 1.
C.W. Fabjan et al., Phys. Lett. 60B:105 (1975).

[28] O. Botner, Phys. Scripta 23:555 (1981).

[29] A. Benvenuti et al., Nucl. Instrum. Methods 125:447 (1975).

[30] M.J. Corden et al., Phys. Scripta 25:5 (1982).
[31] A. Beer et al., Nucl. Instrum. Methods 224:360 (1984).
[32] T. Akesson et al., Properties of a fine sampling uranium–copper scintillator hadron calorimeter, submitted to Nucl. Instrum. Methods (1985).
[33] T. Gabriel and W. Selove, private communication.
[34] U. Amaldi and G. Matthiae, private communications.
[35] H. Abramowicz et al., Nucl. Instrum. Methods 180:429 (1981). See also, for earlier work, J.P. Rishan, SLAC 216 (1979).
[36] Results similar to those given in [35] were recently obtained by the WA78 Collaboration at the CERN SPS (P. Pistilli, private communication).
[37] C.W. Fabjan et al., Nucl. Instrum. Methods 141:61 (1977).
[38] W.J. Willis, Invited talk given at the Discussion Meeting on HERA Experiments, Genoa (1984).
[39] T. Akesson et al., Proc. ECFA-CERN Workshop on a Large Hadron Collider in the LEP Tunnel, Lausanne and Geneva, M. Jacob, ed., CERN 84-10 (1984).
[40] F. Binon et al., Nucl. Instrum. Methods 188:507 (1981).
[41] A.V. Barns et al., Phys. Rev. Lett. 37:76 (1970).
See also T. Ferbel, Understanding the fundamental constituents of matter, A. Zichichi, ed., Plenum Press, New York, NY (1978).
[42] J.A. Appel et al., Nucl. Instrum. Methods 127:495 (1975).
D. Hitlin et al., Nucl. Instrum. Methods 137:225 (1976).
R. Engelmann et al., Nucl. Instrum. Methods 216:45 (1983)
U. Micke et al., Nucl. Instrum. Methods 221: 495 (1984).
[43] M. Basile et al., A limited-streamer tube electron detector with high rejection power against pions, to be published in Nucl. Instrum. Methods (1985).
[44] J. Cobb et al., Nucl. Instrum. Methods 158:93 (1979).
[45] J. Ledermann et al., Nucl. Instrum. Methods 129:65 (1975).
[46] L. Baum et al., Proc. Calorimeter Workshop, Batavia, 1975, M. Atac, ed., FNAL, Batavia, Ill. (1975), p. 295.
A. Grant, Nucl. Instrum. Methods 131:167 (1975).
M. Holder et al., Nucl. Instrum. Methods 151:69 (1978).
[47] A. Bodek et al., Phys. Lett. 113B:77 (1982).
[48] K. Eggert et al., Nucl. Instrum. Methods 176 (1980) 217.
[49] Technical Proposal of the L3 Collaboration, CERN/LEPC/83-5 (1983).
[50] H. Gordon et al. (HELIOS Collaboration), Lepton production, CERN/SPSC 83-51 (1983).
[51] Design Report: An experiment at D0 to study antiproton–proton collisions at 2 TeV, December 1983.
[52] G. Arnison et al., Phys. Lett. 139B:115 (1984).
P. Bagnaia et al., Z. Phys. C. 24:1 (1984).
[53] W.J. Willis and K. Winter, *in* Physics with very high energy e^+e^- colliding beams, CERN 76-18 (1976).
[54] B.L. Beron et al., Proc. 5th Int. Conf. on Instrumentation for High-Energy Physics, Frascati, 1973. Laboratori Nazionali del CNEN, Frascati (1973), p. 362.
[55] Y. Chan et al., IEEE Trans. Nucl. Sci. NS-25:333 (1978).
[56] R. Batley et al., Performance of NaI array with photodiode readout at the CERN ISR, to be submitted to Nucl. Instrum. Methods
[57] M. Miyajima et al., Number of photo-electrons from photomultiplier cathode coupled with NaI (Tl) scintillator, KEK (Japan) 83-36 (1983).

[58] G.J. Bobbink et al., Nucl. Instrum. Methods 227:470 (1985).
[59] G. Blanar et al., Nucl. Instrum. Methods 203:213 (1982).
E. Lorenz, Nucl. Instrum. Methods 225:500 (1984).
[60] J. Ahme et al., Nucl. Instrum. Methods 221:543 (1984).
[61] J.A. Bakken et al., Nucl. Instrum. Methods 228:294 (1985).
[62] C. Laviron and P. Lecoq, Radiation damage of bismuth germanate crystals, CERN-EF/84-5 (1984).
[63] Ch. Bieler et al., Nucl. Instrum. Methods 234:435 (1985).
[64] M. Kobayashi et al., Proc. Int. Symp. on Nuclear Radiation Detectors, INS Tokyo, (1981). Inst. for Nuclear Study, Tokyo (1981), p. 465.
[65] D.E. Wagoner et al., A measurement of the energy resolution and related properties of an SCG1-C scintillation glass shower counter array for 1-25 GeV positrons, to be published in Nucl. Instrum. Methods (1985).
[66] B. Powell et al., Nucl. Instrum. Methods 198:217 (1982).
[67] W. Bartel et al., Phys. Lett. 88B:171 (1979).
[68] P.D. Grannis et al., Nucl. Instrum. Methods 188:239 (1981).
[69] K. Ogawa et al., A test of dense lead glass counters, to be published in Nucl. Instrum. Methods.
[70] R.M. Brown et al., An electromagnetic calorimeter for use in a strong magnetic field at LEP based on CEREN 25 lead glass and vacuum photo-triodes, presented at the IEEE Meeting on Nuclear Science, Orlando, Fla., 1984.
[71] C.A. Heusch, The use of Cherenkov techniques for total absorption measurements, preprint CERN-EP/84-98 (1984): invited talk given at the Seminar on Cherenkov Detectors and their Application in Science and Technology, Moscow, 1984.
[72] H. Grassmann, Untersuchung der Energieauflösung eines CsI(Tl) Testkalorimeters für Elektronen zwischen 1 GeV und 20 GeV, Universität Erlangen (1984).
H. Grassmann et al., Nucl. Instrum. Methods 228:323 (1985).
[73] M. Laval et al., Nucl. Instrum. Methods 208:169 (1983).
[74] D.F. Anderson et al., Nucl. Instrum. Methods 228:33 (1985)
[75] A. Kusumegi et al., Nucl. Instrum. Methods 185:83 (1981).
[76] H.H. Chen et al., Nucl. Instrum. Methods 150:579 (1984).
[77] E. Gatti et al., Considerations for the design of a time projection liquid argon ionization chamber, BNL 23988 (1978).
[78] K. L. Giboni, Nucl. Instrum. Methods 225:579 (1984).
[79] C. Cerri et al., Nucl. Instrum. Methods 227:227 (1984).
[80] J. Engler et al., Phys. Lett. 29B: 321 (1969).
[81] W.A. Shurcliff, J. Opt. Soc. Am. 41:209 (1951).
[82] R.C. Garwin, Rev. Sci. Instrum. 31:1010 (1960).
[83] G. Keil, Nucl. Instrum. Methods 89:111 (1970).
[84] W.B. Atwood et al., SLAC-TN-76-7 (1976).
[85] A. Barish et al., IEEE Trans. Nucl. Sci. NS-25:532 (1978).
[86] W. Selove et al., Nucl. Instrum. Methods 161:233 (1979).
[87] V. Eckardt et al., Nucl. Instrum. Methods 155:353 (1978).
[88] O. Botner et al., IEEE Trans. Nucl. Sci. NS-28:510 (1981).
[89] W. Hofmann et al., Nucl. Instrum. Methods 195:475 (1982).
[90] W. Kienzle, Scintillator development at CERN, CERN-NP Int. Report 75-12 (1975).
[91] W. Viehmann and R.L. Frost, Nucl. Instrum. Methods 167:405 (1979).
[92] J. Fent et al., Nucl. Instrum. Methods 225:509 (1984).

[93] H. Spitzer, Contribution to the Discussion Meeting on HERA Experiments, Genoa (1984);
J. Ahme et al., Novel readout schemes for scintillator sandwich shower counters, to be published.
[94] H.A. Gordon et al., Phys. Scripta 23:564 (1981).
[95] UA1 Collaboration, Technical report on the design of a new combined electromagnetic/hadronic calorimeter for UA1, CERN/SPSC/84-72 (1984).
[96] W. Kononnenko et al., Nucl. Instrum. Methods 214:237 (1983).
[97] L. Bachman et al., Nucl. Instrum. Methods 206:85 (1983).
[98] J. Borenstein et al., Phys. Scripta 23:549 (1981).
[99] H. Blumenfeld et al., Nucl. Instrum. Methods 225:518 (1984).
H. Burmeister et al., Nucl. Instrum. Methods 225:530 (1984).
[100] H. Schönbacher and W. Witzeling, Nucl. Instrum. Methods 165:517 (1979).
Y. Sirois and R. Wigmans, Radiation damage in plastic scintillators, submitted to Nucl. Instrum. Methods.
[101] G. Marini et al., Radiation damage of organic scintillation materials, CERN 'Yellow' Report, in preparation (1985).
[102] Usually, 'accelerated' tests are performed with levels of irradiation 10 to 10^6 times higher than those encountered in an experiment. Because radiation damage is frequently a function of both dose rate and integral dose, such tests are likely to indicate a higher dose tolerance than in the actual lower dose-rate experimental environment. R. Wigmans, private communication and Ref. [100].
[103] R.J. Madaras et al., Nucl. Instrum. Methods 160:263 (1979).
A.E. Baumbaugh et al., Nucl. Instrum. Methods 197:297 (1982).
A.M. Breakstone et al., Nucl. Instrum. Methods 211:73 (1982).
[104] Design report for the Fermilab Collider Detector Facility (CDF), FNAL (1981).
[105] V. Brisson et al., Phys. Scripta 23:688 (1981).
[106] W.J. Willis and V. Radeka, Nucl. Instrum. Methods 120:221 (1974).
[107] L.W. Alvarez, LRL Physics Note 672 (1968) unpublished.
[108] S.E. Derenzo et al., Nucl. Instrum. Methods 122:319 (1974).
[109] K. Masuda et al., Nucl. Instrum. Methods 188:629 (1981).
[110] T. Doke et al., Nucl. Instrum. Methods 134:353 (1976).
T. Doke, Portugal Phys. 12,1:9 (1981).
[111] G.R. Gruhn, private communication (1973).
[112] M. Conversi, Nature 241:160 (1973);
M. Conversi and L. Frederici, Nucl. Instrum. Methods 151:193 (1978).
[113] G.S. Abrams et al., IEEE Trans. Nucl. Sci. NS-27:59 (1980).
[114] V. Kadansky et al., Phys. Scripta 23:680 (1981).
[115] H.J. Behrend et al., Phys. Scripta 23:610 (1981).
[116] C. Nelson et al., Nucl. Instrum. Methods 216:381 (1983).
[117] J.A. Appel, Summary Session of the Gas Sampling Calorimeter Workshop, Fermilab FN-380 (1982);
J. Engler, Nucl. Instrum. Methods 217:9 (1983).
[118] M. Jonker et al., Nucl. Instrum. Methods 215:361 (1983).
[119] G. Battistoni et al., Nucl. Instrum. Methods 202:459 (1982).
[120] SLD Design Report SLAC-273 (1984).
[121] Presentations at the Discussion Meeting on HERA Experiments, Genoa, 1984.
[122] W.F. Schmidt and A.O. Allen, J. Chem. Phys. 52:4788 (1970).
[123] J. Engler and H. Keim, Nucl. Instrum. Methods 223:47 (1984).
[124] L. Onsager, Phys. Rev. 54:554 (1938).

[125] R.C. Munoz et al., Ionization of tetramethylsilane by alpha particles, Brookhaven Nat. Lab. C-2911 (1984), submitted to Chemical Physics Letters.
[126] G.G. Harigel, Nucl. Instrum. Methods 225: 641 (1984).
[127] P.G. Rancoita and A. Seidman, Nucl. Instrum. Methods 226:369 (1984).
G. Barbiellini et al., Nucl. Instrum. Methods 235:55 (1985).
[128] E. Gatti and V. Radeka, IEEE Trans. Nucl. Sci. NS-25:676 (1978).
[129] G. Charpak and F. Sauli, Ann. Rev. Nucl. Part. Sci. 34:285 (1984).
[130] H. Videau, Nucl. Instrum. Methods 225:481 (1984).
[131] G. Battistoni et al., Nucl. Instrum. Methods 176:297 (1980).
[132] H.G. Fischer and O. Ullaland, IEEE Trans. Nucl. Sci. NS-27:38 (1980);
M. Berggren et al., Nucl. Instrum. Methods 225:477 (1984).
[133] E. Iarocci, Nucl. Instrum. Methods 217:30 (1983).
[134] P. Campana, Nucl. Instrum. Methods 225:505 (1984).
[135] H. Aihara et al., Nucl. Instrum. Methods 217:259 (1983).
[136] B. Pope, Proc. DPF Workshop, Berkeley (1983), LBL-15973, p. 49.
[137] O. Botner and C.W. Fabjan, Measurements with the AFS calorimeter, unpublished note (1982).
[138] R. Diebold and R. Wagner, Physics at 10^{34} cm^{-2} s^{-1}, ANL-HEP-CP-84-87 and Proc. of the 1984 Summer Study of the Design and Utilization of the Superconducting Super Collider, Snowmass, Colo. (1984).
[139] P. Curie and A. Laborde, C.R. Acad. Sci. 136:673 (1903).
[140] S. Simon, Nature 135:763 (1935).
[141] T.O. Niinikoski and F. Udo, Cryogenic detection of neutrinos, CERN/NP Internal Report 74-6 (1974).
E. Fiorini and T. Niinikoski, Nucl. Instrum. Methods 224:83 (1984).
[142] B. Cabrera et al., Bolometric detection of neutrinos, Harvard preprint HUTP-84/A077 (1984).
[143] N. Coron et al., A composite bolometer as a charged-particle spectrometer, preprint CERN-EP/85-15 (1985).
[144] A.V. Vishnevskii et al., Moscow preprint ITEP-53 (1979).
[145] R. Bouclier et al., CERN-EP Internal Report 80-07 (1980).
[146] W.J. Willis, private communication.
[147] D.H. Perkins, Ann. Rev. Nucl. Part. Sci. 34:1 (1984).
[148] See, for example, Proc. 1980 International DUMAND Symposium, ed. V.J. Stenger. Honolulu, Hawaii (1981).
[149] R. Cady et al., Proc. 1982 DPF Summer Study on Elementary Particle Physics and Future Facilities, eds. R. Donaldson, R. Gustavson and F. Paige, p. 630.
R.M. Baltrusaitas et al., Phys. Rev. Letters 52:380 (1984).
[150] UA2 Collaboration, Proposal to improve the performance of the UA2 detector, CERN/SPSC 84-30 (1984).
[151] W.J. Willis, BNL 17522:207 (1972).
[152] See for example, Proc. DPF Workshop, Berkeley (1983), LBL-15973.
[153] E.D. Bloom and C.W. Peck, Ann. Rev. Nucl. Part. Sci. 33:143 (1983).
[154] Physics with very high energy e^+e^- colliding beams, CERN 76-18 (1976).
[155] E. Picasso, General Meeting on LEP, Villars-sur-Ollon, 1981, ed. M. Bourquin. ECFA 81/54, CERN, Geneva (1981), p. 32.

[156] The technical proposals for the four LEP experiments have the following LEP Committee numbers:
ALEPH, CERN/LEPC 83-2(1983);
DELPHI, CERN/LEPC/83-3 (1983);
OPAL CERN/LEPC/83-4 (1983);
L3, CERN/LEPC/83-5 (1983).
[157] W.K.H. Panofsky, Proc. Int. Symp. on Lepton and Photon Interactions at High Energies, Bonn, 1981, ed. W. Pfeil, Phys. Inst., Bonn (1981), p. 957.
[158] S.L.Wu, Phys. Reports 107:61 (1984).
[159] C. Rubbia, Physics results of the UA1 Collaboration at the CERN proton-antiproton Collider preprint CERN-EP/84-135 (1984): invited talk given at the Int. Conf. on Neutrino Physics and Astrophysics, Nordkirchen near Dortmund,1984.
[160] Experimentation at HERA, Proceedings of a Workshop jointly organized by DESY, ECFA, and NIKHEF, Amsterdam (1983).
[161] W. Selove, CERN/NP Internal Report 72-25 (1972).
[162] S. Almehed et al., CERN/ISRC/76-36 (1976).
[163] M.A. Dris, Nucl. Instrum. Methods 161:311 (1979).
[164] M. Block, UA1 Collaboration (CERN), unpublished note UA1-6, (1977).
[165] L. Rosselet, Proc. Topical Conf. on the Applications of Microprocessors to High-Energy Physics Experiments, Geneva, 1981, CERN 81-07 (1981), p. 316.
[166] R.L. Ford and W.P. Nelson, Stanford preprint SLAC-210 EGS, Version IV.
[167] T. Kondo et al., Talk given at the 1984 Summer Study on the Design and Utilization of the Superconducting Super-Collider, Snowmass, Colo., 1984.
DELPHI Progress Report, CERN/LEPC 84-16 (1984).
[168] A. Grant, Nucl. Instrum. Methods 131:167 (1975).
[169] H. Fesefeldt, Proc. Workshop on Shower Simulation for LEP Experiments, eds. A. Grant et al. CERN report in preparation.
[170] Proc. Workshop on Shower Simulation for LEP Experiments, eds. A. Grant et al. CERN report in preparation.

PERFORMANCE AND LIMITATIONS OF ELECTROMAGNETIC CALORIMETERS

Tejinder S. VIRDEE

Blackett Laboratory, Imperial College, London SW7 2BZ, UK.

ABSTRACT

The factors which determine and limit the performance of electromagnetic calorimeters are considered. Their performance can be characterized by the resolution attained in the measurement of the energy, the direction, the position and the timing of electrons or photons. Further factors such as two shower separation, electron-hadron separation and sensitivity to radiation damage are also considered.

1. Introduction

A high energy electron or photon incident on a thick absorber initiates a cascade of electrons, positrons and photons via pair production and bremsstrahlung. With increasing depth in the absorber material the energy of these particles is degraded and the number of shower particles increases. When the energy of the electrons and positrons falls below the critical energy, ϵ, the energy at which the radiative energy losses become equal to ionization energy losses, further dissipation of energy is dominated by ionization and atomic or molecular excitation rather than by the generation of more shower particles.

The longitudinal development of the showers is governed by the radiation length, X_0, defined to be the mean distance over which a high energy electron loses all but 1/e of its energy by bremsstrahlung. The lateral shower development is characterized by the Moliere radius which gives a measure of the lateral deflection of electrons of an energy of ϵ after traversal of $1X_0$. For rough estimation $X_0 \approx 180A / Z^2$ in g cm^{-2} and R_M(cm) $\approx 10/\rho$ (ρ in g cm^{-3})†. The shower development is approximately material independent when defined in terms of X_0 and R_M.

The longitudinal development of 10 GeV electron showers in Al, Fe and Pb[2c], generated using the EGS4 computer code, is shown in Fig.1. The shower maximum is deeper for higher Z materials due to the lower critical energy leading to particle multiplication down to lower energies. The slower decay beyond the maximum is due to the lower energies at which electrons can still radiate in higher Z materials.

Two effects are responsible for the lateral spread of an e.m. shower namely

- multiple scattering of electrons or positrons away from the axis,
- minimally attenuated photons depositing their energy a long way from their point of origin especially when emitted from electrons that travel at large angles w.r.t. shower axis.

---

† For more accurate estimation the following expressions[1] can be used

$X_0 = 716.4\ A / [Z(Z+1)\ \ln(287/\sqrt{Z})] \approx 180\ A/Z^2$ g cm^{-2}

$R_M = 21.2$ (MeV) X_0 / ϵ where $\epsilon = 800 / (Z+1.2)$ MeV.

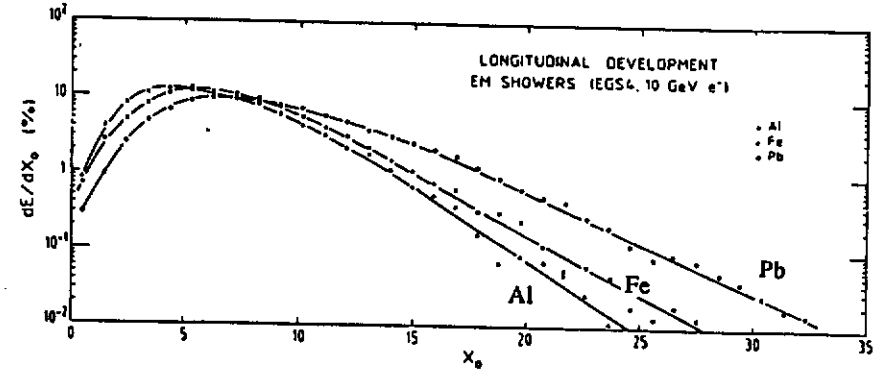

Fig.1 The longitudinal development of 10 GeV electron showers in different absorbers.

The former process dominates in the early part of the shower whilst the latter dominates deeper in. For example, the FWHM of the lateral profile of energy deposition is ~ 500 μm at a depth of 5 X_0 in CeF_3 for 30 GeV photon showers (Fig. 2a). The e.m. showers are narrow as can be seen from Fig. 2b. In liquid xenon 90% of the shower energy is contained in a cylinder of radius ≈ 7 cm (~ 1.75 R_M). The corresponding numbers for CeF_3 are ≈ 4.25 cm or ≈ 1.65 R_M.

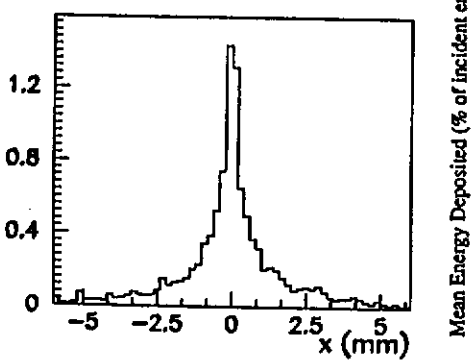

Fig. 2a. Lateral profile of the energy deposited in 300 μm thick Si at a depth of $5X_0$ in CeF_3 for a 30 GeV e^- shower.

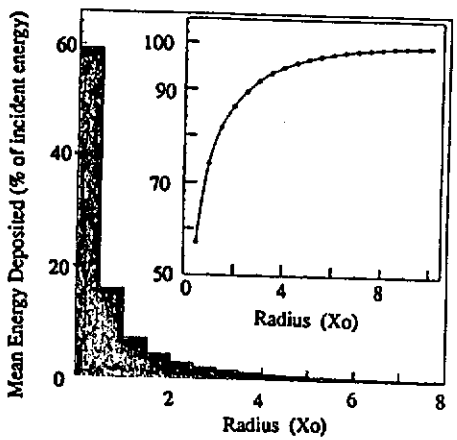

Fig. 2b. % of incident energy deposited in a long cylinder of radius r.

The performance of a stand–alone e.m. calorimeter can be quantified by considering :

- the energy resolution,
- impact position resolution,
- angular resolution,
- two shower separation,
- electron-hadron separation,
- the speed of response and,

- sensitivity to radiation damage

When integrated into an overall detector further parameters need to be considered, eg.

- jet energy resolution when combined with a hadronic calorimeter
- electron identification (with charged particle tracking and hadron calorimetery)
- effect of a magnetic field.

The relative emphasis placed on these parameters determines the calorimeter choice.

This report relies heavily on previous reviews[2] of electromagnetic calorimeters.

2. Energy Resolution

Conventionally the energy resolution of calorimeters is parameterized as

$$\frac{\sigma}{E} = \frac{a}{E} \oplus \frac{b}{\sqrt{E}} \oplus c$$

where the symbol ⊕ implies the square root of the quadratic sum of the three terms on r.h.s.

The "noise" term [coefficient a] includes

- the energy equivalent of the electronics noise and,
- the fluctuation in the energy carried by particles, other than the one of interest, entering the measurement area during the time over which the energy measurement is made.

The "sampling" term [coefficient b] accounts for

- the statistical fluctuation in the number of primary and independent signal generating processes, or any further process that limits this number eg. conversion of scintillation light into photo-electrons by a photosensor.

The "constant" term [coefficient c] takes into account

- the fluctuation in the amount of energy leakage from the front, the rear and the sides of the volume used for the energy measurement,
- the fluctuation in the amount of energy deposited in dead materials in front of or inside the calorimeter,
- the cell to cell inter-calibration error and,
- the non-uniformity in the generation or collection of the signal.

Such a parmetrization allows the identification of the various causes of resolution degradation. The assumption that the terms be added quadratically implies that the contributions are independent which may not always be the case. When comparing different calorimeters it is, of course, the actual value of the resolution, σ/E, at the relevant energies, that is important.

2.1 Intrinsic Energy Resolution

2.1.1 Homogeneous Calorimeters

When considering energy resolution it is instructive to start by looking at homogeneous calorimeters. All the energy of an incoming electron or photon is deposited in the active medium. If this is assumed to be laterally and longitudinally infinite then the resolution in the measured energy would only arise from the fluctuation in the produced number of ion pairs or photons. This is given by n = E/W where W is the mean energy required to produce an ion pair (or a photon). As the production process is random in nature the fluctuation on n will be given by

$\sigma/E = \sqrt{n} / n = \sqrt{(W/E)}$

However the fluctuation is reduced because the total energy deposited in the medium does not fluctuate. This reduction is characterized by the Fano factor, F, after Fano who first evaluated the size of such fluctuations [3]. The resolution will then be given by :

$$\sigma / E = \sqrt{(FW / E)} \qquad (1)$$

Photon energy resolution in Ge, operated at 77 °K, has been measured[4] to be $\sigma \approx 178$ eV at 100 keV, $\sigma \approx 390$ eV at 661 keV and $\sigma \approx 550$ eV at 1000 keV. It takes 2.98 eV to create an electron-hole pair. The energy difference between the band gap (Table 1) and the W value goes into phonons. For an energy deposit of 661 keV $n \approx 2.2.10^5$ and Poisson statistics lead to a resolution of ~1.4 keV. This is considerably worse than the measured resolution. Application of Fano's factor for Ge gives the observed value of ~ 0.4 keV. A comparison[4] of the pulse height spectra in Ge and NaI crystals is shown in Fig. 3.

Material	W_e (eV)	W_γ (eV)	F	Band Gap (eV)
Si	3.6	-	0.14	1.1
Ge	2.9	-	0.13	0.7
LAr	23.7	-	0.11	-
LKr	20.5	53	0.06	-
LXe	16.4	38	0.05	-

Table 1. Some properties of materials used for low energy total absorption calorimeters.

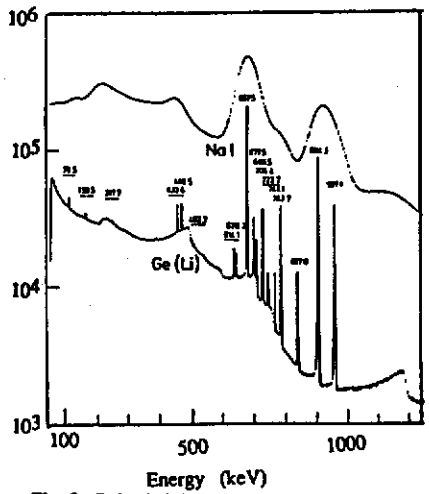

Fig. 3. Pulse height spectra in Ge and NaI.

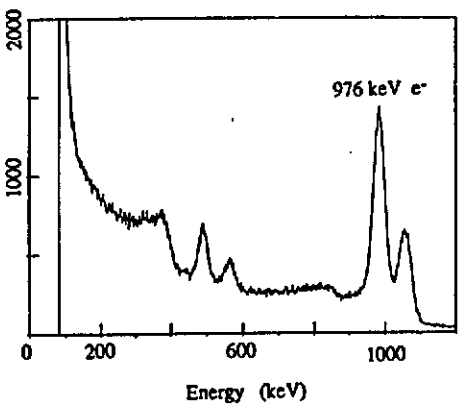

Fig. 4. Pulse height spectrum in liquid argon.

Noble liquid calorimeters should, in principle, allow measurement of ~ MeV photons to a similar precision. The energy resolution for 976 keV electron conversion line of ^{207}Bi is observed[5] to be only ≈ 11 keV (Fig. 4) whereas the use of Eq. 1 leads to 1.6 keV. It has been suggested[6] that the poorer energy resolution is due to the production of δ-rays. Approximately 30% of the energy deposited by a 976 keV electron is deposited by densely ionizing δ-rays[5b] carrying a kinetic energy of less than 10 keV. The electron-ion pair recombination is higher for densely ionizing tracks. This decreases the observed charge and the fluctuation in the amount of energy deposited by δ–rays then dominates the overall resolution.

Another source of fluctuation is in the amount of energy going into mechanisms other than the one being measured eg. scintillation when only ionzation charge is collected. The noble liquids listed in Table 1 also generate scintillation light. An anti-correlation between the amount of the charge collected and the luminescence intensity is seen[7] (Fig. 5). The scintillation light can arise from recombination and if it is detected together with the ionization then the energy resolution improves. Although this may not play a significant role for high energy measurements it could allow such liquids to be used for precise measurements at low energies.

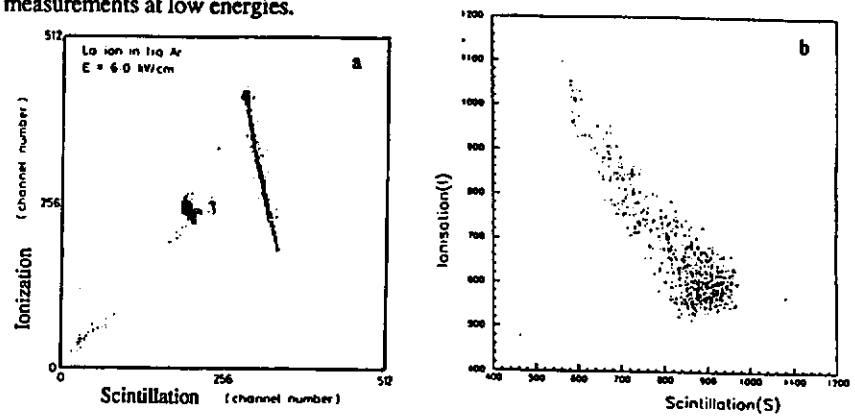

Fig. 5. The anti-coirrelation between the collected charge and the luminescence intensity in LAr.

Other phenomena may limit the number of signal generating events. Lead glass shower detectors are based on the detection of Cerenkov light, produced by the electrons and positrons with kinetic energies greater than ~ 0.7 MeV. This means that at most 1000 / 0.7 ~ 1400 independent particles, per GeV of deposited energy, produce Cerenkov light. The resolution is then dominated by the fluctuation in this number and thus cannot be better than $\sigma/E = \sigma_n \geq 3\% / \sqrt{E}$. A further contribution comes from the photoelectron (p.e.) statistics. Approximately 1000 p.e. are generated per GeV of deposited energy. The observed resolution then becomes $\sigma/E \sim \sqrt{(\sigma_n^2+\sigma_p^2)} \sim 4.4\%/\sqrt{E}$. An energy resolution of $\sigma/E \sim 5\% / \sqrt{E}$ for e.m. showers in the energy range 1-20 GeV has been attained in a large lead glass array [8].

Scintillation light from crystals has been used to attain good resolution at high energies. Their energy resolution is usually limited not by the statistics of primary light producing processes but by leakage of energy and by the non-uniformity in the generation and the collection of light. NaI(Tl) was the first type of crystal to be used in a large scale high energy physics experiment [9]. The energy resolution for 8 keV γ-rays is $\sigma/E \sim 15\%$, ~ 5% for 1 MeV and ~ 1% for 1 GeV electrons. Hence the resolution is worse by a factor ≥ 3 at 1 MeV and ~ 30 at 1 GeV if it is scaled by $\sigma/E \propto 1/\sqrt{E}$ from the lowest energy. This indicates

that the resolution is not dominated by statistical fluctuations but by the systematic effects mentioned above. Fig. 6 shows the observed energy resolution for high energy electrons[10]. A scaling law more like $\sigma/E \propto 1/E^{1/4}$ describes the data and is ascribed to energy leakage. Variation in light yield or collection efficiency can also yield a similar dependence as shown by a simulation[11] in which the light output was varied with σ=5% per cc.

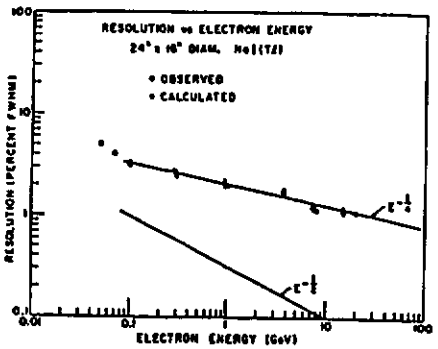

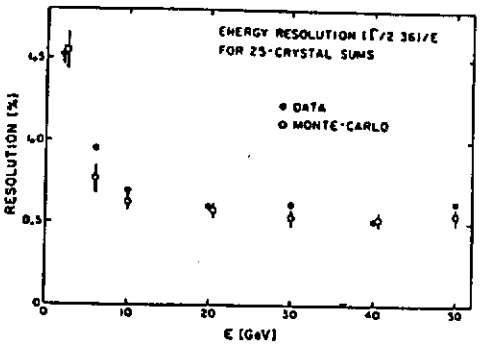

Fig. 6 The energy resolution for an array of NaI crystals. Fig. 7. As in Fig. 6 but for BGO crystals.

A very good energy resolution of $\sigma/E \sim 2\%/\sqrt{E} \oplus 0.5\%$ has been achieved[12] for a large number of BGO crystals in a test beam (Fig. 7). This has yet to be achieved in the L3 experiment where the resolution for electrons (~ 45 GeV) from Bhabba events is presently ~1.2%. The uncertainty in the energy of the electrons due to intial state radiation has not been unfolded. The poorer than expected resolution is believed to be due to cell to cell intercalibration error, poorer energy resolution for electrons entering near the crystal boundaries (section 2.5) and the variation of temperature inside the crystals. The light yield in BGO varies by –1.55% per °C of temperature change. This experience underlines the difficulty of attaining very high energy resolution in large systems.

2.1.2 *Sampling Calorimeters*

When the very best energy resolution is not required, sampling calorimeters are employed. The shower energy is measured in active layers, often of low Z, sandwiched by passive absorber layers of high Z materials. The energy resolution is determined by the fluctuation in the fraction of shower energy deposited in the active layers. If the energy loss in an active layer is much smaller than that in the absorber the number of independent charged particles crossing an active layer can be approximated by n=E/ΔE where ΔE is the energy lost by a minimum ionizing particle (m.i.p.) in the absorber layer. If t_{abs} is the thickness of the absorber layer and dE/dx is the energy lost per unit path length traversed by a m.i.p then $\Delta E = t_{abs}\, dE/dx$. The sampling fluctuation is then given by the familiar form

$$\sigma/E = \sqrt{n}/n \propto \sqrt{(\Delta E/E)} \propto k\sqrt{t_{abs}}/\sqrt{E} \quad (E \text{ in GeV}). \qquad (2)$$

The dependence of the resolution on ΔE can be seen in Fig.8 for various absorber and active materials[2d]. The constant k is ≈ 15% (with some material dependence) for $t_{abs} = 1\ X_o$.

A large fraction of the energy in an e.m. shower is deposited by low energy (few MeV)

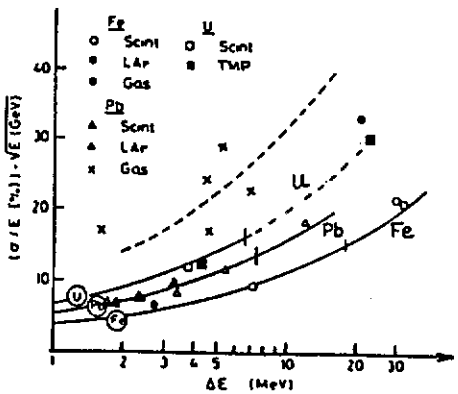

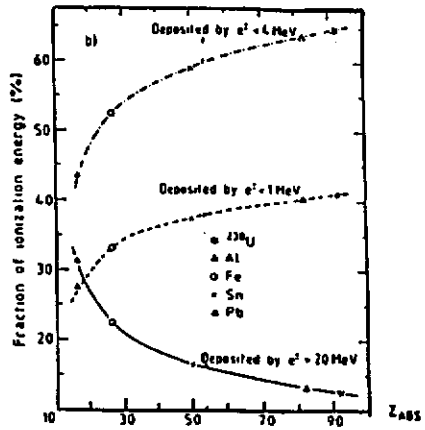

Fig. 8 Electron energy resolution as a function of the energy lost (ΔE) in one absorber layer.

Fig. 9 Fraction of the ionization energy deposited by particles of different momenta in a 10 GeV e⁻ shower.

electrons especially in absorbers with high Z (Fig.9). These electrons are generated by either the photoelectric effect or Compton scattering. These have a high power dependence on Z and hence usually take place in the absorber layers. When the electron, from the process γ (of low energy) –> e, is created near the surface of an absorber layer it can enter the active layers. Usually it cannot traverse more than one active layer because, for the absorber thicknesses usually employed, the energy loss in one absorber layer is too large. This leads to an energy resolution dependence $\propto \sqrt{t_{abs}}$.

Deviations from the scaling formula (2) can be understood by considering two cases. The first is where the absorber thickness is kept fixed but the thickness of the active layer is increased. The fraction of the incident energy deposited in the active medium increases. The improvement in the resolution[13] with increasing t_{act} can be seen in Fig. 10. Lead absorber plates of a thickness of 1/3 X_o sandwich a liquid argon active layer of varying thickness. The magnitude of this effect depends on the difference between the Z of the active and the passive layers

In the second case scaling according to Eq. 2 will not continue when t_{abs} becomes very small as the number of crossings in successive active layers now become correlated. This is clearly evident in a liquid argon calorimeter[14] with very fine sampling : 400 cells of 1mm stainless steel followed by a 1.05 mm gap of LAr (total 25.7 X_o). A resolution of $\sigma \sim 1.4\%$ is observed for 25 GeV electrons ($\sigma/E \approx 7\%/\sqrt{E}$). Scaling using Eq. 2 yields $\sigma \sim 0.8\%$ ($\sigma/E \approx 4\%/\sqrt{E}$).

These effects can be taken into account by parametrizing the energy resolution in terms of the sampling structure and the amount of energy deposited in the active medium. If ΔE_c is the energy, in MeV, that is deposited (eg. approximately by a m.i.p.) in one active and one passive layer and A is the fraction of the incident energy deposited in the active medium then the energy resolution can be written as

$$\frac{\sigma_s}{E} = \frac{5\%}{\sqrt{E}}(1-A)\ \Delta E_c^{0.5(1-A)} \qquad (3)$$

This is an extension of "Waseda's Formula"[15] which gives a worse resolution than M.C. simulation for the sampling effects for large ΔE_c and A. Some experimental data and results of M.C. simulations are compared in Fig. 11 with the resolution computed using Eqn.3. The contribution of the limited photoelectron statistics of the scintillator calorimeters has been unfolded. When A is small the familiar form for sampling calorimeters is recovered. We believe that this expression can predict the e. m. energy resolution to within 20%.

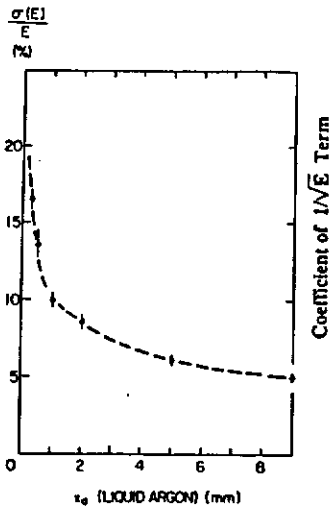

Fig. 10 Variation of the energy resolution versus the thickness of the active layer.

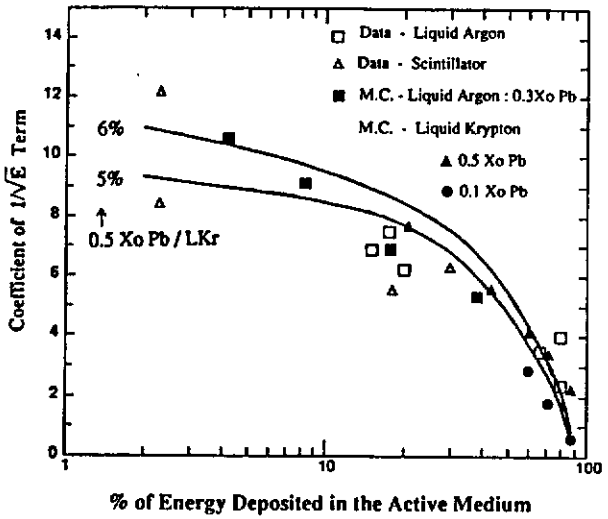

Fig. 11 Coefficient of the sampling term versus the % of energy deposited in the active medium.

2.2 *Degradation of Energy Resolution due to Energy Leakage*

Energy leakage, from the calorimeter volume used for the energy measurement, leads to a degradation of energy resolution. Fig.12 illustrates the degradation due to longitudinal and lateral energy leakage for a homogeneous LXe calorimeter [16]. Longitudinal leakage clearly has more serious consequences. At a fixed energy the profile of the longitudinal energy deposition differs from one shower to another. Showers developing late lead to a larger energy leakage from the rear of a finite depth calorimeter. The fraction of the incident energy leaking out, and the fluctuation on it, increases with energy since the depth at which the shower maximum occurs increases with energy, albeit logarithmically. Fig.13 shows the longitudinal development of photon showers, of different energies, in liquid xenon[16]. The resolution will no longer scale according to $1/\sqrt{E}$ as already seen in Fig.6 for NaI. The r.m.s. deviation, as a fraction of the mean deposited energy, versus the fractional longitudinal energy leakage (f) is plotted in Fig. 14. For a quick estimation[2b] $\sigma_{rms}/\langle E_{dep}\rangle \approx f/2$ for $f \lesssim 20\%$.

The loss of energy resolution due to the lateral energy leakage is smaller since the lateral profile of energy deposition differs much less from one shower to another. The energy dependence of the fluctuation is also weak as the lateral shower shape is almost independent

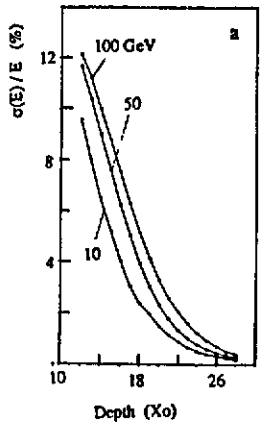

Fig. 12 The effect of a) longitudinal and b) lateral energy leakage on energy resolution of a LXe calorimeter.

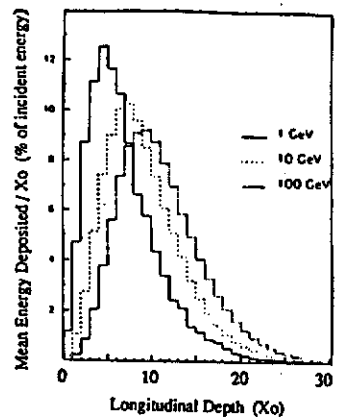

Fig. 13 The longitudinal profile of energy deposition in LXe for 1, 10 and 100 GeV γ's.

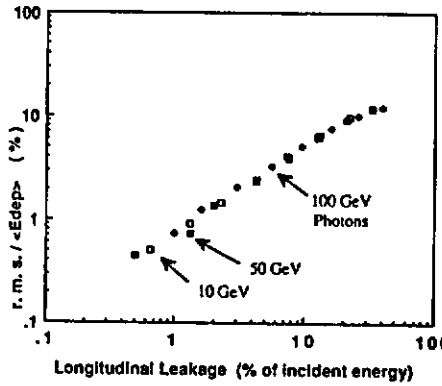

Fig. 14 Fractional r.m.s. of mean deposited energy versus longitudinal leakage in LXe.

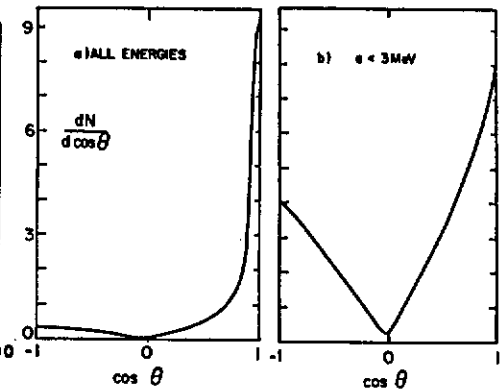

Fig. 15 The angular distribution of secondary electrons a) of all energies b) with < 3 MeV in a 1 GeV e^- shower.

of energy especially at high energies.

Energy leakage from the front of calorimeters can affect energy resolution, especially at low energies. The backscattered photons and electrons typically have energies lower than the critical energy. The fluctuation in the energy carried away by these particles results in a resolution loss[17] of ~ few percent for 100 MeV photons and ~ 0.1% for ones with energy greater than 10 GeV.

2.3 *Resolution Worsening due to Path Length and Landau Fluctuations*

In sampling calorimeters with relatively thin ($\lesssim 0.01$ g cm^{-2}) active layers the energy resolution is considerably worse than equivalent ones with thicker active layers. Gas

sampling calorimeters fall into this category. The poor resolution is due to two effects: path length and Landau fluctuations[13].

The angular distribution of shower electrons, plotted in Fig.15, shows that about 12% of all the electrons are back scattered into the sampling gaps. For low energy electrons (< 3 MeV) this percentage is considerably higher. The wide spread of angles leads to large fluctuations in the length of tracks in the active layers and hence in the deposited energy. In thick active layers the energy deposited by low energy electrons going forward at small angles is not much different from those at larger angles since their range, at low energies, is roughly similar to the thickness of the active layer. Fig. 10 shows that thick in this context would mean a few mm of LAr. In a gas sampling calorimeter the active layer usually has a thickness of ~ 10^{-3} g cm^{-2}. Low energy electrons that travel in the plane of the active layer deposit considerably more energy than the ones moving perpendicularly to the plane.

The energy deposited by a m.i.p. traversing an active layer is described by the Landau distribution which is an asymmetric distribution with a long tail towards high deposited energy. Therefore the resolution scaling is worse than $1/\sqrt{n}$, expected for n crossings. An order of magnitude estimate for this effect is given by [2a]

$$\sigma/E = (1/\sqrt{n})\,[2/\ln(10^4\ t\ (\mathrm{g.cm^{-2}})]\ .$$

In a calorimeter with active layers of t ~1 g.cm^{-2}, the Landau fluctuation worsens the resolution by ≤ 3% whereas in a gas sampling calorimeter (t ~ 10^{-3} g.cm^{-2}) the resolution worsens by ~ 40%.

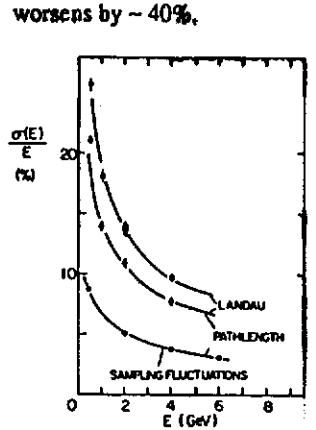

Fig. 16 Contribution of the Landau and path length fluctuations to the energy resolution

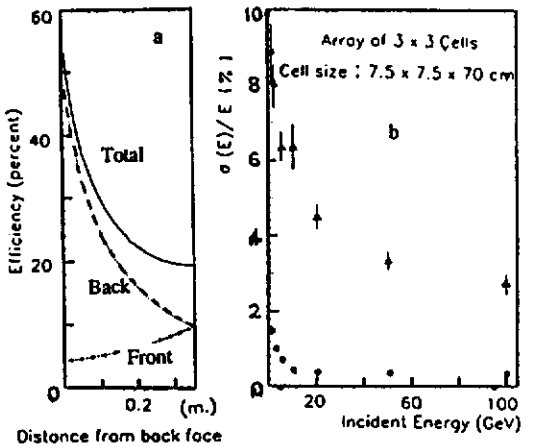

Fig. 17 a) Light collection efficiency b) energy resolution in a rectangular cell filled with liquid xenon.

For gas calorimeters the above two effects give similar contributions[13] (~12% at E=1 GeV). Combining with the sampling fluctuation (for a calorimeter with 1/3 X_0 absorber layers) leads to an overall resolution of ~ 18% /$\sqrt{E}$ (Fig.16). This can be compared with experimentally measured resolutions for gas calorimeters shown in Fig. 8.

2.4 Resolution Worsening due to Non-uniformity of Signal Generation and Collection

Longitudinal non-uniformity of signal generation and collection, when folded with the fluctuation in the longitudinal profile from one shower to another (at a fixed energy), leads to a loss of energy resolution. This will also lead to energy non-linearity due to the energy dependence of the average profile for longitudinal energy deposition.

The effect on the energy resolution of non-uniformity of light collection in a homogeneous liquid xenon calorimeter is shown in Fig.17[16]. Electron showers were generated in a setup of dimensions 22.5 x 22.5 x 70 cm^3 (8x 8x 25 X_0), split into 3 x 3 rectangular cells. The scintillation light is generated isotropically and the non-uniformity of light collection is due only to the imperfect reflectivity of the cell walls (with a reflectivity of 80% for 175nm light). The result is clearly unacceptable. Graded reflectivity of the side walls should enable more uniform light collection and consequently better energy resolution.

Light inside a crystal is usually internally reflected and hence the non-uniformity of light collection is not as severe as in the case mentioned above. The scintillation light in BGO crystals for the L3 experiment is detected by Si photodiodes mounted at the rear of the crystals. The efficiency of light collection from the front of the crystals is increased by the tapered geometry of the crystals. Fig. 18 shows the light collection uniformity as measured with a collimated ^{137}Cs source running along the main dimension of the crystal. The non-uniformity observed for crystals wrapped in aluminized mylar is greatly reduced by coating the polished crystals with a 40-50 μm thick layer of high reflectivity NE560 white paint. The effect of the non-uniformity can be parameterized by

$$S(x) = S(L)\ [1 - R(1 - x/L)\ ] \qquad (4)$$

where S(x) is the observed light signal, x is the distance from the diode plane and S(L) is amount of light detected when the source is at a distance L from the diode plane (L is the length of the crystal). Fitting the data in Fig.18 to Eq. 4 yields R=0.1 and 0.53 for the white paint coating and mylar wrapping respectively. Fig. 19 shows the Monte Carlo estimation of

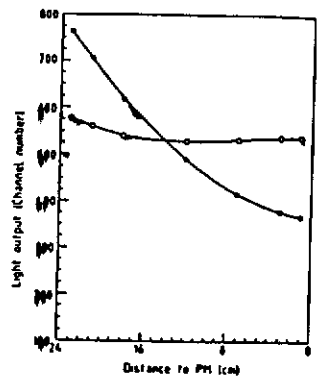

Fig. 18 Light collection versus distance from diode plane o - white paint coating, • aluminized mylar wrapping.

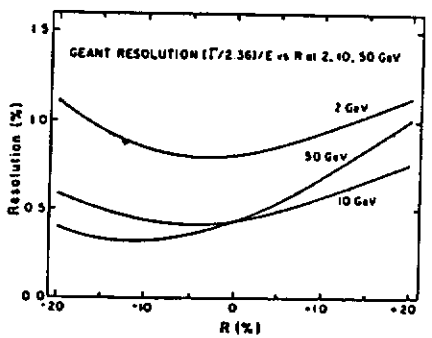

Fig. 19 Energy resolution as a function of the parameter R (see text).

the resolution degradation for different values of R. Without the coating the energy resolution of the BGO crystals would have been unacceptable. At the future colliders radiation damage will not be uniform and its effect on the uniformity of light collection for the crystal calorimeters must be estimated.

Calorimeters based on ionization chambers with a large drift gap also suffer from an effective non-uniformity of signal collection. An electron created near the cathode plane

contributes 1e to the induced charge whereas one created next to the anode contributes nothing. The signal induction efficiency thus ranges from ≈ 100% close to the cathode plane and ≈ zero near the anode palne. The calorimeter therefore appears to have a coarser sampling. If the shaping time is made smaller than the drift time a more uniform efficiency is obtained but the size of the signal is reduced. The magnitude of this effect has been estimated[18] for a LAr calorimeter with a structure of 500 μm G10 and 1 cm LAr gap using a peaking time > drift time. The estimated contribution, from this effect, to σ/E is ≈ 1% /√E whilst the sampling contribution is estimated to be ≈ 0.5% /√E.

Scintillating plastic fibre calorimeters, eg. SPACAL which has a lead to scintillator volume ratio of 4 and 1mm diameter fibres, show a large constant term in the electromagnetic energy resolution function[19]. This decreases when the angle of incidence w.r.t. the fibre axes gets larger. The sizeable constant term is due to at least two effects. Both the effects lead to lateral non-uniformity at a scale smaller than the overall lateral shower size and hence to a variation of response that is independent of incident energy. These are :

- dependence of the size of the observed signal on the impact point. The lateral size of the shower in the early part is smaller than the inter fibre separation. Consequently electrons entering the calorimeter in a fibre will, on average, produce larger signals than those entering lead.
- the number of fibres that contribute significantly to the shower measurement in this calorimeter is small because of the narrowness of e.m. showers. Hence fibre to fibre variations will affect the resolution. If the distribution of the fibre to fibre response has an r.m.s. of σ_f and the number of fibres contributing significantly to the signal is n_f then the size of the constant term will be $c = \sigma_f/\sqrt{n_f}$. For the test described in ref 19, $\sigma_f \approx 6\%$ and $n_f \approx 25$ leading to $c \approx 1.2\%$. A recent test[20] using fibres with a diameter of $\phi = 0.5$ mm, instead of $\phi = 1$mm, yielded a constant term of ≈ 0.7%. The Pb scintillator volume ratio was kept the same thus increasing n_f by a factor of 4. Since the inter-fibre separation also decreased the impact on the energy resolution of both the effects described above is reduced.

The sampling term in the resolution also improves by a factor of √2 from 12.9 % for the calorimeter with 1 mm diameter fibres to 9.3% for the one with ϕ=0.5mm.

2.5 *Effect of Dead Material in Front or Inside e.m .Calorimeters*

Dead material in front of e.m. calorimeters can be present because of eg. support structures or vacuum and cryostat walls for noble liquid calorimeters. Side wall supports may also be necessary to hold in place the calorimeter elements eg. crystals. The energy lost in the dead materials decreases the mean and increases the width of the observed energy distributions. This is shown in Fig 20 where a varying thickness of Al absorber was placed in front of an e.m. calorimeter[21] with a performance parametrized by σ/E = 18% /√E. Sizeable deterioration takes place for absorber thicknesses of ≥ $2X_0$. This degradation can be reduced by measuring the energy flow just after the dead material.

The presence of dead material, consisting of 200 μm Carbon fibre walls, the crystal wrapping and the distributed air gap, in between BGO crystals contributes to the degradation of the energy resolution. The energy resolution[12] with the beam centred on a

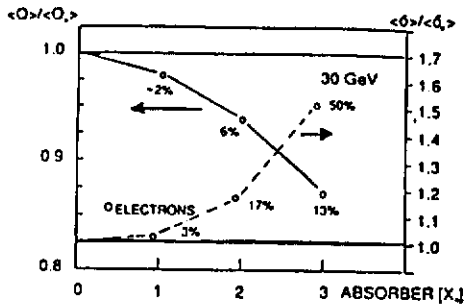

Fig. 20 Ratio of std. dev. with, <σ>, and without absorber, <σ_o>, versus the absorber thickness.

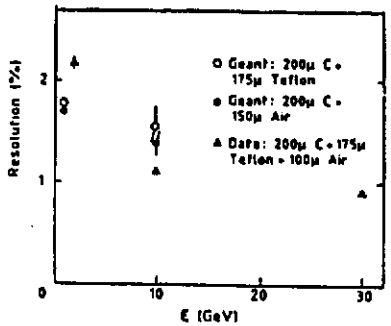

Fig. 21 Influence of walls on energy resolution. Beam is centred on the wall between two crystals.

wall is shown in Fig. 21. Comparison with Fig 7 shows that the degradation in the resolution, close to the crystal boundaries, is significant. Since the lateral shower shape does not vary much for high energy e.m. showers, such degradation of resolution is independent of incident energy and thus contributes to the constant term.

2.6 *Deterioration of Energy Resolution due to Inter-calibration Errors*

Electromagnetic showers are narrow (Fig.2b) and usually the central cell, or at most the central four cells, contains ≈ 80% of the shower energy. The reconstructed energy, Erec, can be expressed as

$$E_{rec} = \sum_{i=1}^{n} g_i E_i$$

where E_i is the energy in the i th cell, g_i is the calibration constant of the i th cell and n is the number of cells used to measure the energy. The lateral shape of e.m. showers does not change much from one shower to another (or with energy). Hence any deterioration of the energy resolution, due to inter-calibration errors, will be independent of energy. If the r.m.s. error on g_i is δ then the uncertainty on E_{rec} will be $c = \delta/\sqrt{n}$ leading to $c \approx \delta/2$ for n=4.

The cell to cell intercalibration error should therefore be considerably smaller than the desired constant term i.e. ≤ 0.3 % if the overall constant term is 0.5%. Although it is possible to achieve such accuracy in the calibration of electronics, it is more difficult in calorimeter system as a whole. The task is easier for calorimeters using unit gain and temporally stable primary signal generation and collection. An example of the excellent performance that is possible in such devices is the CERN-NA31 liquid argon calorimeter [22].

CDF collaboration has used their central magnetic field to measure the momenta of electrons originating from b, W and Z decays. These electrons are used to calibrate the electromagnetic calorimeter. An r.m.s. error of approximately 1.7% has been achieved[23] from a data sample yielding ~ 35 electrons per cell. At the future colliders electrons from Z decays can probably be used for calibrating the e.m. calorimeters. The rate of $Z \rightarrow e^+e^-$ pairs, in a rapidity interval of $|\eta| \leq 2$ and at a luminosity of $L = 10^{34}$ $cm^{-2}s^{-1}$ is ≥ 10 Hz. Appoximately 100 $e^{\pm}$ tracks per cell (size $\Delta\eta x \Delta\phi \approx 0.025 x 0.025$) per week could be recorded. This should be sufficient to achieve a few per mille calibration error, provided that

both the momentum and energy measurements are made with a precision of ≈ 1%. Electrons from b's and W's could be used at lower luminosities.

2.7 *Noise due to the Electronics and Energy Pileup*

Electronics noise, noise from radioactivity or from energy pileup make a constant contribution to the measured energy. This contribution can limit the precision of energy measurements up to ≤ 50 GeV at the future hadron colliders.

Electronics noise has to be considered whenever gain is obtained by the use of amplifiers. This can become a problem when very fast signals are desired. Consider the case of a liquid ionization chamber. If the electron lifetime in the liquid is very large, compared with the drift time (t_d), the current pulse is triangular in shape for uniform ionization across the gap. The observed charge for a peaking time of t_p is given by

$$Q_p = Q_T \{ 2t_p/t_d - (t_p/t_d)^2 \} \qquad 0 < t_p < t_d$$
$$Q_p \sim 2 Q_T t_p/t_d \qquad \text{and } t_p << t_d.$$

Since the equivalent noise charge varies as $1/\sqrt{t_p}$, the S/N ratio deteriorates as $(t_p)^{3/2}$. The CERN RD3 Collaboration[24] have measured an electronics noise equivalent (ENE) of 3.6 MeV/cell for $t_p \sim 100$ ns and $t_d \sim 400$ns. The energy of high energy showers is measured in 5 x 5 cells, with a two-fold depth segmentation. This leads to a total ENE of ~ 25 MeV. A peaking time of $t_p \sim 20$ ns was tried[25] and the resulting ENE became ~ 350 MeV for a three-fold depth segmentation. For a high energy resolution calorimeter such a noise level will dominate the energy resolution up to ≈100 GeV (if the constant term turns out to be ≤0.5%)

At a high luminosity hadron collider the spray of energy from the many overlapping minimum bias events can spoil the energy resolution. This can be a serious problem for high energy resolution e.m. calorimeters placed too close to the interaction vertex. For a calorimeter with a perfect energy resolution the smearing of the reconstructed γγ mass (=100 GeV) due to energy pileup from <10> interactions is shown[26] in Fig 22. The pileup is shown as a positive contribution though negative pileup, due to pulse shaping, can also occur. The magnitude of the effect of energy pileup can be obtained by considering a calorimeter with a resolution parameterized by $\sigma/E = 2\%/\sqrt{E} \oplus 0.5\%$. The size of the optimized mass window is 1.5 GeV for the search of a 100 GeV mass object decaying into 2 γ's. At a luminosity of $L = 10^{34}$ cm^{-2}s^{-1}, and for a measurement area of $\Delta\eta\Delta\phi$=0.1x0.1, about 10% of the signal events will fall outside the mass window due to energy pileup. In CeF_3 and for 95% lateral energy containment this situation corresponds to a distance from the interaction vertex of 1.3m.

2.8 *Effects of Radiation Damage*

High radiation levels are expected at the future colliders. The radiation dose in e.m. calorimeters will be predominantly due to photons from the decays of low momenta π^0's. For integrated luminosities of 10^{41} cm^{-2}, the expected[27] radiation dose and neutron levels are shown in Fig 22. Calorimeters based on the detection of light are particularly prone to radiation damage due to:

- a loss of light emission efficiency and

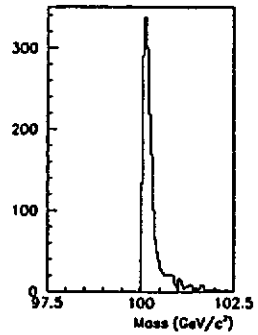

Fig.22 Reconstructed γγ mass for M_H=100 GeV with smearing due to energy pileup from <10> interactions.

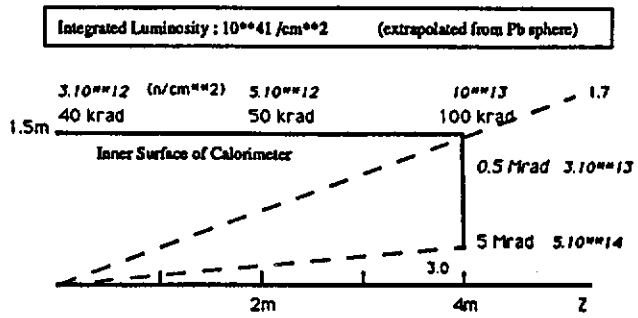

Fig. 23 Radiation doses and neutron fluences in e.m. calorimeters ($\int Ldt = 10^{41}$ cm^{-2})

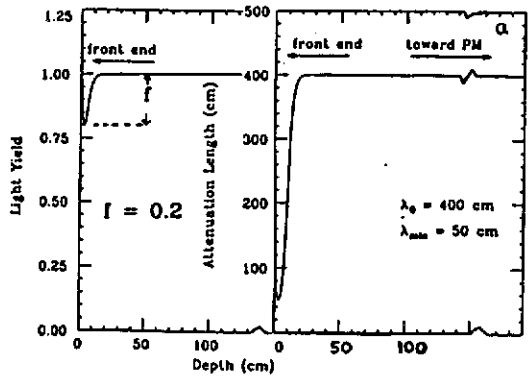

Fig. 24a Change in attenuation length and light yield as a function of depth due to radiation damage.

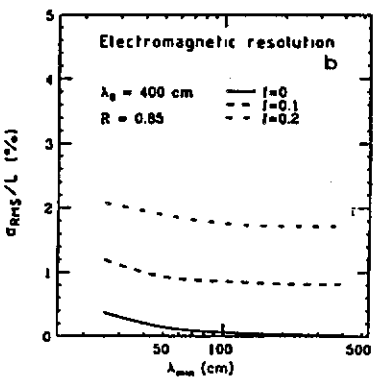

Fig. 24b Contribution to the energy resolution due to decreased light yield and attenuation length.

- an increase in the light attenuation in the damaged regions.

As an example we consider the studies carried out for a scintillating fibre calorimeter. Damage to plastic scintillating fibres results in the loss of both the emission and the transmission efficiency and leads to energy non-linearity and resolution degradation. Changes in attenuation length (λ) and light yield (f, which is the maximum fractional loss in light yield), as shown[28] in Fig. 24a, lead to a contribution to the energy resolution of ~ 1.69 % for 150 GeV electrons Fig.24b. The loss in efficiency of light emission is the more serious. If a contribution of 0.8% to the constant term is acceptable then the recieved dose should be ≤7 Mrad. Crystal scintillators will probably be less affected by radiation damage since the scintillation process is not affected up to doses of ~ 1 Grad.

3. Angular and Spatial Resolution

3.1 *Angular Resolution*

The two photon effective mass resolution is given by

$$\frac{\delta m}{m} = \frac{1}{2}\sqrt{\left(\frac{\delta E_1}{E_1}\right)^2 + \left(\frac{\delta E_2}{E_2}\right)^2 + \left(\cot\left(\frac{\theta}{2}\right)\delta\theta\right)^2}$$

where E_1, E_2 are the energies of the two photons and θ is opening angle between them. Good angular resolution can be obtained by measuring the impact position of the photons and linking them to the primary vertex. Running at high luminosities leads to many primary vertices per crossing. In order to reconstruct precisely the mass of a purely neutral final state, eg. H–> 2γ, measurement of the direction of the photons, with a good angular resolution, by the calorimeter itself is required. Fig. 25 illustrates[26] the degradation of mass resolution due to the lack of the knowledge of the vertex position, for a Higgs of a mass of 100 GeV/c^2, in a calorimeter with a perfect resolution starting at a radial distance of 2m from the interaction vertex. Reduction of this radius, without knowling the vertex position, would clearly worsen the resolution. The loss of resolution is equivalent to that due to energy resolution in a calorimeter with $\sigma/E = 7\%/\sqrt{E} \oplus 1.0\%$. An angular resolution of ~ 5 mrad is required to match an energy resolution of $\sigma/E = 2\%/\sqrt{E} \oplus 0.5\%$.

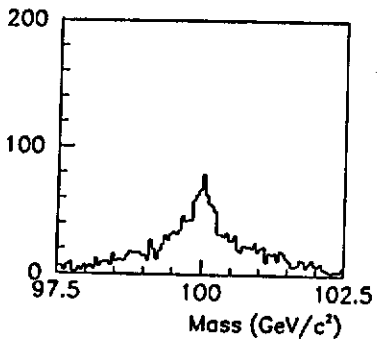

Fig. 25 Reconstructed mass smeared by loss of knowledge of vertex position (MH=100 GeV σvtx=5.5cm)

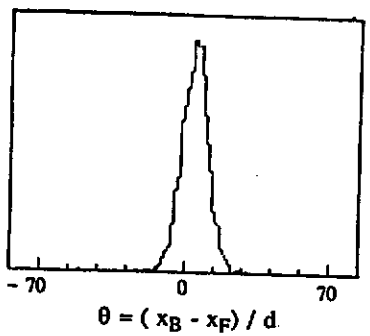

Fig. 26 Em shower angular resolution achieved by CERN-RD3 ("Accordion") LAr Calorimeter.

The angular resolution attained in a recent beam test[24] of the "Accordion" calorimeter is shown in Fig. 26. Two longitudinal segments, of 12.5 X_0 each, not optimized for angular measurement, were used. The barycentre in the front and back compartments, x_F and x_B respectively, is determined using the fine lateral segmentation. The effective lever arm, d, is extracted from the data and the angle is then given by $\theta = (x_B - x_F) / d$. An angular resolution of $\Delta\theta \approx 6.1$ mrad for 120 GeV electrons is obtained. It should scale $\approx 1/\sqrt{E}$ as the accuracy of the barycentre determinations improve similarly.

3.2 Spatial Resolution

The position of impact of a photon or an electron can be deduced from

i) the centre of gravity of the transverse energy deposition in the calorimeter cells,
ii) a preshower detector, placed after some amount of dead material ($\approx 1.5\ X_0$),
iii) a position detector, placed after a first sampling of $\approx 3\text{-}5\ X_0$.

The last approach relies on the narrowness of the shower in the early part of its longitudinal development. The simulated transverse shower profile in 300 μm thick Si counter placed at a depth of $5X_0$ is shown in Fig. 2a. A spatial resolution for photon showers of ≈ 2 mm /√E (E in GeV) should be possible using Si-strips with a pitch of 2mm. The precision improves as $1/\sqrt{n}$ where n is the effective number of m.i.p.'s passing through Si. As n is roughly proportional to the incident energy the resolution improves as $1/\sqrt{E}$. Similar precision, for a similar granularity, should be possible in the approach (ii) once the signal is clearly above the noise level.

In the first approach the size of the cells, and less importantly the noise contributions from either the electronics or the energy pileup, limits the precision of the spatial measurement. The spatial precision attained[29] versus cell size, 2Δ, using square lead glass blocks (X_0=2.4 cm) is shown in Fig. 27. A 25 GeV electron beam was used in this study. Recent results[24] from the "Accordion" LAr calorimeter (Fig. 28) show a position resolution of 4.4mm /√E (E in GeV) for single showers. The cells had a size of ≈ 2.7 cm (≈ 2.1 X_0).

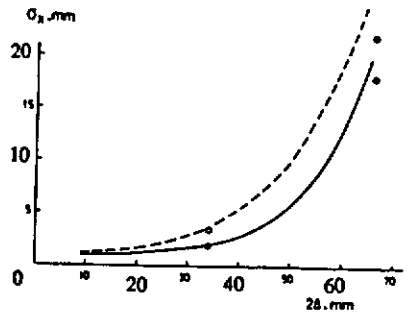

Fig. 27. Spatial resolution for 25 GeV electrons using square lead glass blocks of side 2Δ.

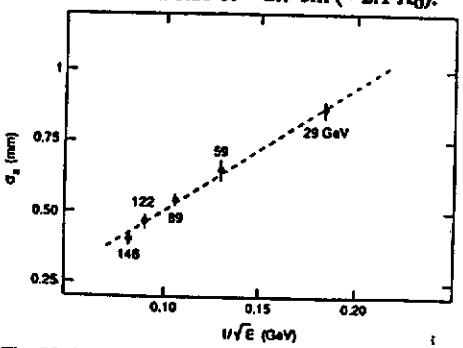

Fig. 28. Spatial resolution attained in the "Accordion" lead/liquid argon prototype.

4. Two Shower Separation

Recognition of two e.m. showers close to each other is important for the rejection of π^0–>2γ background when studying of prompt single photon production. The narrowness of

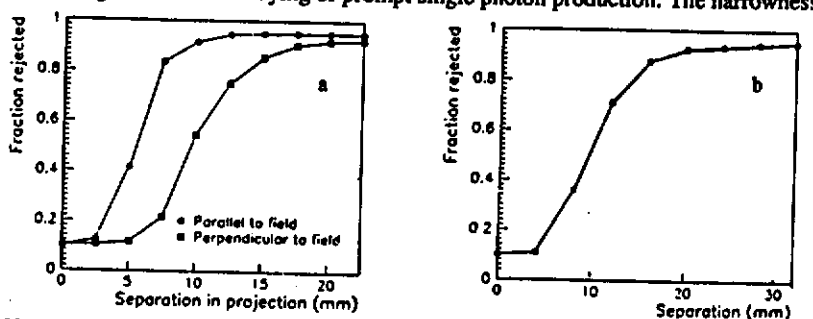

Fig. 29 Rejection of photon pairs versus their separation in a) one projection b) both projections.

the e.m. shower in the early part can be used to isolate events consisting of genuine single photons. The search for the intermediate mass Higgs via its two photon decay will require both a very high efficiency for the reconstruction of single photons and a high rejection power for two photon impacts (from jet -> π^0 -> 2γ). A simulation[30] using two orthogonal planes of Si strips (2mm pitch) leads to typical rejection power of ~ 6–10 for two shower separation of ~ 1.5 cm (Fig.29). An efficiency of 90% for a single shower is retained.

Two shower rejection is also possible using the mosaic structure of towers and pre-shower detectors. However a high two shower rejection power and a high single shower efficiency may be compromised by the presence pileup of low energy photons.

5. Electron – Hadron Separation

A high energy pion faking an electron leads to the contamination of signals using prompt electrons. At LHC in order to bring the rate of fake electrons from this source to a factor ~ 10 below that from the genuine sources (b –> e X, W –> ev etc.) an e-π separation of ≥ 1000 is required for p_T's ≥ 10 GeV/c.

The electron–hadron separation is usually based on the difference in the longitudinal and lateral development of showers intiated by electrons and hadrons. One or more of the following can be used to achieve the desired pion rejection power when detecting electrons :

i) a preshower detector at ≈ 1.5 X_0
ii) a position detector at ≈ 3-5 X_0
iii) lateral segmentation
iv) longitudinal segmentation including a hadron calorimeter
v) energy - momentum matching

The ultimate rejection power is limited by the charge exchange process (or first interaction), which results in one or several π^0s taking most of the energy of the incoming hadron. The shower from such hadrons then looks like an e.m. shower. Therefore sampling of showers early in their longitudinal development is imprtant.

The separation power for single particle[31], using (ii - iv) is shown in Fig.30. The structure of the calorimeter consisited of :

- towers of a lateral size of ~11 x 11cm (effective X_0 ≈ 8mm),
- 8-fold longitudinal segmentation, the first four samplings (2mm U / 2.5 mm TMP) with thicknesses of 3, 6, 10, 7 X_0 leading to a total of 1λ, the next two (5mm U/ 2.5mm TMP) with thicknesses of 0.7 λ and the last two (5cm Fe/ 1cm scint) with thicknesses of 2.5 λ.
- a position detector placed at a depth of 3 Xo.

The rejection power, as a function of energy, using (ii), (iii) and (iv) individually and then all combined is shown.

6. Timing Resolution

Machines running at high luminosities, and with short inter-crossing times, will require very fast processing of signals. Consider the example of LHC (or SSC) where the crossing

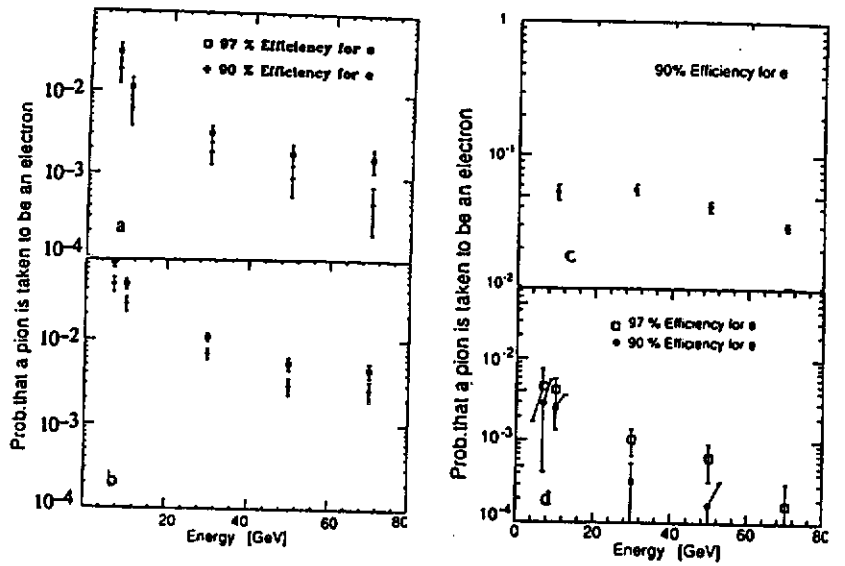

Fig. 30 The probability that a single pion is taken to be an electron using a) longitudinal profile only, b) lateral profile only, c) position detector only and d) all combined.

times are ~15ns. The consequences for a calorimeter that integrates over more than one crossing are due to the amount of extra pile-up energy that is introduced. Amongst these are

- a degradation of energy (and hence mass) resolution due to increased energy pileup from soft photons or hadrons from the many minimum bias events that occur within the resolution time of the calorimeter (section 2.7).
- a decreased effectiveness of isolation criteria due to extra energy entering the area used for isolation. Isolation is usually assured by making a cut on the sum of energy that falls in a cone around the track of interest in η–ϕ space. Integration over more than one crossing, even at a luminosity of $L = 10^{33}$ cm^{-2}s^{-1} may mean that cuts on energy sum, to ensure isolation, become inefficient. It may turn out that track isolation at high luminosities has to be carried out by requiring no extra tracks (photons or charged particles) with high p_T or E_T (> 2–5 GeV) inside the isolation cone.
- poorer shower track matching for electrons resulting in a decreased electron efficiency[2e] if only the transverse energy deposition, eg. in cells of a size $\Delta\eta x\Delta\phi$≈ 0.03 x 0.03, is used to localize high energy electrons.

7. Jet Energy Resolution

The design of the electromagnetic and hadronic calorimeters has to be different if the physics emphasizes the need for a very good e.m. energy resolution. This usually excludes the possibility of obtaining an overall compensating hadronic calorimeter, assuming that the

use of a weighting technique is not possible. The important issue is not only the jet or single particle energy resolution but also the shape of the measured energy distributions. Tails on these can fake large missing transverse energies which may compromise physics that requires cuts on such quantities. The performance of a calorimeter with different e.m. and hadronic sub-calorimeters has only been studied in simulations which usually cannot simulate accurately the systematic effects that lead to tails. Confirmation by beam tests of such systems should clearly be contemplated by groups designing such calorimeter systems.

8. Conclusion

The effect on the energy resolution of many of the sources described above can be seen[32] in Fig. 31. The results from beam tests of a liquid krypton filled calorimeter are shown. The calorimeter had a cylindrical shape with a depth of 76 cm (16.5Xo) and a diameter of 42 cm (9.5Xo) calorimeter. The ionization charge was collected on 500μm G10 boards separated by drift gap of 2 cm. Also shown are the calculated contributions to the energy resolution of different effects.

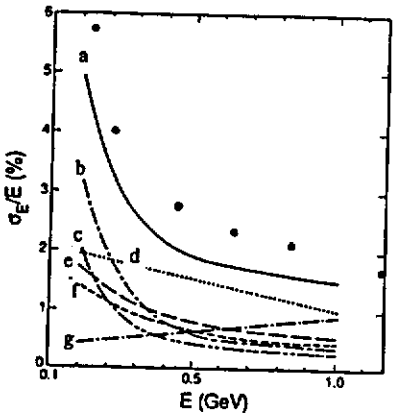

Fig. 31 Data from beam tests and calculated resolution of the KEDR liquid krypton e.m. calorimeter: a) total, b) elctronic noise, c) radioactivity, d) lateral leakage, e) charge induction efficiency, f) sampling fluctuations and g) longitudinal leakage

Acknowledgements

I would like to thank C. Fabjan and C. Seez for reading the manuscript and making several useful suggestions.

References

1. Particle Properties Data, M. Aguilar-Benitez et al., *Phys. Lett. B239.*
2a. U. Amaldi, *Phys. Scripta* 23 (1981) 409.
2b. C. W. Fabjan, *CERN-EP/85-54* (1985).
[2a] and [2b] also appear in *Experimental Techniques in High Energy Physics* ed. T.Ferbel (Addison-Wesley 1987) p 257 and p 325 respectively.
2c. C.W. Fabjan and R. Wigmans, CERN-EP/89-64, Reports on Progress in Physics
2d. R. Wigmans, *Proc. of ICFA School on Instrumentation in Elementary Particle Physics*, Trieste (1987) eds. C.W. Fabjan and J. E. Pilcher (World Scientific, Singapore 1988).
2e. J. Colas et al., p370, CERN 90-10 , ECFA LHC Workshop, Aachen (1990).

3. U. Fano, *Phys. Rev* . 72 (1947) 26.
4. G. F. Knoll, *Radiation Detection and Measurement*, John Wiley and Sons.
5a. E. Aprile et al., *Nucl. Instr. and Meths.* A261 (1987) 519.
b. K. Giboni, *Nucl. Instr. and Meths.* A269 (1988) 554.
6. A.E. Bolotnikov et al., *Prib. Tekh. Eksp.* 4 (1986) 42.
7a. H. Crawford et al., *Nucl. Instr. and Meths.* A256 (1987) 47.
b. J. Seguinot et al., CERN-LAA-PC/90-24 (1990)
8. R. M. Brown et al., *IEEE Trans. Nucl. Sci.* NS-32 (1985) 136.
9. E. Bloom and C. Peck, *Ann. Rev. Nucl. and Part. Sci.* 33, (1983) 143.
10. E. B. Hughes et al., *IEEE Trans. Nucl. Sci.* NS-19 (1972) 126.
11. E. Lorenz, p 621 CERN 89-10, ECFA Study Week, Barcelona (1989).
12. J. A. Bakken et al., *Nucl. Instr. and Meth.*, A254 (1987) 535.
B. Adeva et al., *Nucl. Instr. and Meth.*, A289 (1990) 35.
13. H. G. Fischer, *Nucl. Instr. and Meth.*, 156 (1978) 81.
14. C. Cerri and F. Sergiampietri, *Nucl. Instr. and Meth.*, 141 (1975) 207.
15. Y. Hoshi et al., *Japan. J. Appl. Phys.* 21 (1982) 1086.
16. E. Clayton et al., IC/HEP/90-9, Blackett Lab., Imperial College, London SW7 2BZ.
17. M. Kobayashi et al., *Nucl. Instr. and Meth.*, A308 (1980) 47.
18. T. Doke et al., *Nucl. Instr. and Meth.*, A237 (1985) 475.
19. D. Acosta et al., CERN-PPE/91-85 (1991).
20. J.-M. Gaillard, RD1 Status Report, CERN/DRDC 91-50 (1991).
21. J. Kruger, ZEUS Collaboration, CERN 90-10, ECFA LHC Workshop, Aachen (1990)
22. H. Burkhardt et al., *Nucl. Instr. and Meth.*, A268 (1988) 116.
23. F. Abe et al., *Phys. Rev.*, D43 (1991) 2070.
24. B. Aubert et al., CERN PPE/91-73 (1991), Submitted to Nucl. Instr. and Meths.
25. D. Fournier, RD3 Status Report to the CERN-DRDC Committee (1991)
G. Costa, these proceedings.
26. C. Seez et al., CERN 90-10 , ECFA LHC Workshop, Aachen (1990).
27. G. Stevenson, CERN 90-10 , ECFA LHC Workshop, Aachen (1990).
28. D. Acosta et al., CERN-PPE/91-45 (1991), Submitted to Nucl. Instr. and Meths.
29. G. A. Akopdjanov et al., *Nucl. Instr. and Meths.*, 140 (1977) 441.
30. C. Seez, these proceedings.
31. R. Apsimon et al., *Nucl. Instr. and Meth.*, A305 (1991) 331.
32. V. M. Aulchenko et al., *Nucl. Instr. and Meth.*, A289 (1990) 468.